

Measurement of J/ψ production cross-section in pp collisions at $\sqrt{s} = 13$ TeV

Liupan An¹, Lucio Anderlini², Vanya Belyaev³, Svende Braun⁴, Roberta Cardinale⁵, Sevda Esen⁴, Timothy Daniel Head⁶, Ilya Komarov⁶, Michael Kolpin⁴, Christian Linn⁷, Giulia Manca⁸, Matthew David Needham⁹, Marco Pappagallo¹⁰, Zhenwei Yang¹, Yanxi Zhang¹

¹Center for High Energy Physics, Tsinghua University (CN)

²Universita e INFN, Firenze (IT)

³ITEP Institute for Theoretical and Experimental Physics (RU)

⁴Physikalisches Institut, Ruprecht-Karls-Universitt Heidelberg (GE)

⁵Universita e INFN Genova (IT)

⁶Ecole Polytechnique Federale de Lausanne (CH)

⁷European Organization for Nuclear Research (CH)

⁸Laboratoire de l'Accelérateur Lineaire (FR)

⁹University of Edinburgh (GB)

¹⁰University of Glasgow (GB)

Abstract

Production cross-sections of J/ψ mesons in proton-proton collisions at a centre-of-mass energy $\sqrt{s} = 13$ TeV is measured, using a data sample with the integrated luminosity of $3.05 \pm 0.12 \text{ pb}^{-1}$ collected by the LHCb detector early in LHC operations in 2015. The double differential cross-sections, as functions of the transverse momentum p_T and the rapidity y of the J/ψ meson, are determined separately for prompt J/ψ mesons and J/ψ mesons from b -hadron decays in the range $0 < p_T < 14 \text{ GeV}/c$ and $2 < y < 4.5$. The production cross-sections integrated over the kinematic coverage are

$$\sigma(\text{prompt } J/\psi) = 15.30 \pm 0.03 (\text{stat}) \pm 0.86 (\text{syst}) \mu\text{b},$$

$$\sigma(J/\psi \text{ from } b) = 2.34 \pm 0.01 (\text{stat}) \pm 0.13 (\text{syst}) \mu\text{b}.$$

The comparison between the measurement and several theoretical calculations is performed, and good agreement is observed.

Contents

1	Introduction	1
2	Data and Monte Carlo samples	2
2.1	Data	2
2.2	Monte Carlo	3
3	Candidate reconstruction and selection	3
3.1	Trigger and Turbo stream selection	3
3.2	Offline selection refinement	4
3.2.1	MuonID strategy	5
4	Cross-section determination	6
5	Signal extraction	7
5.1	Determination of the prompt and detached signal yields	9
6	Efficiency determination	12
6.1	Geometrical acceptance	13
6.2	Reconstruction-selection efficiency	13
6.3	Muon identification efficiency	14
6.4	Trigger efficiency	15
6.5	Total efficiency	15
7	Systematic uncertainties	15
7.1	Signal extraction	16
7.1.1	Signal mass shape	16
7.1.2	Fit to t_z	17
7.2	MuonID efficiency	17
7.3	Tracking efficiency	18
7.4	Offline selection efficiency	21
7.5	Trigger efficiency	22
7.6	Unknown spectrum	24
7.7	Polarization scenarios	25
7.8	Other systematic uncertainties	26
7.9	Summary of systematic uncertainties	27
8	Results	27
8.1	Fraction of J/ψ from b	28
8.2	Extrapolation to 4π	29
8.3	Comparison with RUNI results	30
8.4	Comparison with theoretical models	35
9	Conclusion	41

A	Luminosity determination	42
B	Stripping selection	43
C	Parameterization of signal mass shape	43
D	Fit results in each kinematic bin tabulated	48
E	Efficiency tables	51
F	Cross section result tables	58
G	Modelling of t_z resolution	60
H	Introduction to trigger-based analysis	61
I	Comparison of Tesla and stripping candidates	61
J	J/ψ fits	66
K	Study of extrapolation factor	71
	References	72

1 Introduction

Study of heavy quarkonium productions in pp collisions provides important information to probe Quantum Chromodynamics (QCD), which describes the strong interaction between quarks and gluons. The process of heavy quarkonium production involves the production of a heavy quark pair, $Q\bar{Q}$, which happens at a short distance, followed by the heavy quark pair hadronizing into quarkonium. The first step can be calculated with perturbative QCD, while the latter one is non-perturbative and must be determined using experimental results. Thanks to almost forty years of theoretical and experimental efforts, our understanding of hadronic production of quarkonia has improved significantly; however the mechanism is still not fully understood. In the Colour Singlet Model (CSM) [1–7], the intermediate $Q\bar{Q}$ state is supposed to be colourless, and has the same J^{PC} quantum number as the final state quarkonium. While in the Non-Relativistic QCD (NRQCD) approach [8–10], intermediate $Q\bar{Q}$ states with all possible colour-spin-parity quantum numbers have probabilities to transform into the desired quarkonium. The transition probabilities, described by long distance matrix elements (LDME) in NRQCD, are non-perturbative and must be determined by fitting experimental data. These matrix elements are supposed to be universal, and their relative strength is ordered in powers of the velocity of heavy quarks, v , in the rest frame of the quarkonium. For perturbative expansions, only a few matrix elements need to be taken into account for J/ψ hadronic production, and the NRQCD coincides with CSM when only the leading v term is considered.

The CSM calculation at the leading order (LO) underestimates the J/ψ and $\psi(2S)$ production cross-sections in the range of high transverse momentum ($p_T > M(\psi)$) by more than one order of magnitude [11]. The correction at the next-to-leading order (NLO) for CSM changes the p_T behaviour at high p_T [12, 13], and the gap between predictions and experimental data reduces significantly but still not satisfactory; besides, the predicted J/ψ polarisation changes from transverse dominating at LO to significantly longitudinal [14]. NRQCD, with the matrix elements determined by fitting CDF data, can describe the p_T -dependent J/ψ cross-section at CDF [15, 16]. These matrix elements can also well describe the magnitude and the p_T dependence of quarkonium cross-sections measured at the LHC [17–19], confirming the universality of these matrix elements. Despite the success of NRQCD in describing quarkonium hadronic production cross-sections, the predicted large transverse polarisation at high p_T [20–23] is not supported by experimental results [24–30].

In pp collisions, J/ψ mesons can be produced 1) directly from hard collisions of partons, 2) through the feed-down of excited states, or 3) via decays of b -hadrons. The J/ψ mesons from the first two sources originate from the primary vertex of the pp collision, and are called prompt J/ψ , while those from the last source originate from vertices of b -hadrons, which are typically separated from the primary vertex, and are called J/ψ from b .

The J/ψ differential production cross-section has been measured with the LHC data in pp collisions at centre-of-mass energies of 2.76 TeV [31, 32], 7 TeV [33–37], and 8 TeV [38]. The J/ψ polarisation was also measured by ALICE [26], CMS [27] and LHCb [39] in pp collisions at 7 TeV. The measurements by ALICE were for inclusive J/ψ , while ATLAS,

CMS and LHCb disentangle prompt J/ψ and J/ψ from b -hadron decays. Theoretical calculations with CSM and NRQCD were compared with the measurements for prompt J/ψ production. In general the CSM alone at NLO still underestimate the production cross-section, and the NRQCD predicts the kinematic dependent J/ψ cross-section very well. However neither CSM nor NRQCD can model the polarisation satisfactorily. The production cross-sections of J/ψ from b -hadron decays were compared to the calculation at Fixed Order plus Next-to-Leading Logarithms (FONLL) [40], which is a tool to calculate the heavy quark production cross-section. FONLL is able to describe both the integrated cross-sections and the p_T -dependence very well for J/ψ from b -hadron decays.

This note describes details of the J/ψ cross-section measurement in pp collisions at $\sqrt{s} = 13$ TeV, using the data collected early in LHC operations in 2015 corresponding to an integrated luminosity of $3.05 \pm 0.12 \text{ pb}^{-1}$. The measurements include the double differential production cross-sections of prompt J/ψ and J/ψ from b as functions of p_T and y , the fraction, F_b , of J/ψ from b as a function of p_T and y , the integrated production cross-sections of prompt J/ψ and J/ψ from b with $p_T < 14 \text{ GeV}/c$ and $2.0 < y < 4.5$. The $b\bar{b}$ production cross-section in pp collisions at 13 TeV is also determined using the result of J/ψ from b .

2 Data and Monte Carlo samples

2.1 Data

The data sample used in this analysis are pp collisions with center-of-mass energy 13 TeV, collected by the LHCb detector in July 2015. The details of the fill are shown in Table 2.1. The data was taken with TCK 0x00F9014E, and the corresponding muon trigger lines dedicated to this analysis are shown in section 3.1.

Fill	Inte. Lumi. pb^{-1}	Runs
3981	1.03 ± 0.04	157558-157597
3988	0.93 ± 0.04	157697-157710
3988	1.05 ± 0.04	157803-157819

Table 2.1: Fills and corresponding luminosities and run range for this analysis.

The LHCb detector [41, 42] is a single-arm forward spectrometer covering the pseudorapidity range $2 < \eta < 5$, designed for the study of particles containing b or c quarks. The detector includes a high-precision tracking system consisting of a silicon-strip vertex detector surrounding the pp interaction region [43], a large-area silicon-strip detector located upstream of a dipole magnet with a bending power of about 4 Tm, and three stations of silicon-strip detectors and straw drift tubes [44] placed downstream of the magnet. The tracking system provides a measurement of momentum, p , of charged particles with a relative uncertainty that varies from 0.5% at low momentum to 1.0% at 200 GeV/ c . The minimum distance of a track to a primary vertex, the impact parameter,

is measured with a resolution of $(15 + 29/p_T) \mu\text{m}$, where p_T is the component of the momentum transverse to the beam, in GeV/c . Different types of charged hadrons are distinguished using information from two ring-imaging Cherenkov detectors [45]. Photons, electrons and hadrons are identified by a calorimeter system consisting of scintillating-pad and preshower detectors, an electromagnetic calorimeter and a hadronic calorimeter. Muons are identified by a system composed of alternating layers of iron and multiwire proportional chambers [46].

2.2 Monte Carlo

To study the efficiency, Monte Carlo samples with statistics of about 4 M are generated. In the simulation, pp collisions are generated using PYTHIA [47] with a specific LHCb configuration [48]. Decays of hadronic particles are described by EVTGEN [49], in which final state radiation is generated using PHOTOS [50]. The interaction of the generated particles with the detector and its response are implemented using the GEANT4 toolkit [51] as described in Ref. [52]. The prompt charmonium production is simulated in PYTHIA with contributions from both the leading order color-singlet and color-octet mechanisms [48, 53], and the charmonium is generated without polarization.

3 Candidate reconstruction and selection

The reconstruction-selection and of the J/ψ candidates for real data is based on Turbo Stream with a backup-option relying on a dedicated Stripping line from the full stream. Since the Turbo stream is found to work well as Stripping, and its availability comes much earlier than stripping, the candidates from Turbo stream are used for offline analysis.

3.1 Trigger and Turbo stream selection

Editor: Tim Head and Christian Linn

During online data taking, every event is reconstructed by the trigger in order to form a trigger decision. The Turbo stream stores these trigger candidates and writes them to disk. In 2015 the reconstruction in the trigger will be the same as used in the offline reconstruction. For final states with an exclusive selection in the trigger it is natural to use the trigger candidates directly instead of re-reconstructing them offline. The clear advantage of Turbo stream is its availability for offline analysis.

The trigger consists of three separate stages: L0, HLT1 and HLT2, for which the dedicated trigger lines are L0Muon, Hlt1DiMuonHighMass and Hlt2DiMuonJPsi(-Turbo) (since candidates firing this trigger will go to Turbo stream). The L0Muon trigger selects a muon candidate with high transverse momentum $p_T > 900 \text{ MeV}/c$. The Hlt1DiMuonHighMass trigger selects two good quality muon tracks with large momenta and transverse momenta and requires their invariant mass to be heavy, greater than 2700 MeV. The Hlt2DiMuonJPsiTurbo line exclusively reconstructs the J/ψ candidates. The selections

Variable	Value
Track χ^2/ndf	< 3
Track p	$> 3000 \text{ MeV}$
Track p_T	$> 500 \text{ MeV}$
Vertex DOCA	< 0.2
Vertex χ^2	< 25
Muon ID	isMuon
$M(\mu^-\mu^+)$	$> 2700 \text{ MeV}$

Table 3.1: HLT1DiMuonHighMass selection criteria

111 applied for HLT1DiMuonHighMass and HLT2DiMuonJPsiTurbo are given in Tables 3.1 and
112 3.2.

113 Candidates that fired the HLT2DiMuonJPsiTurbo trigger are written to the Turbo
114 stream, and these candidates are called Turbo stream candidates. Candidates in simulation
115 reconstructed with Turbo stream are also called Turbo stream candidates. The Turbo
116 stream candidates are also referred to as online candidates since they are related to a
117 specified trigger. Using the Turbo stream the HLT2 selection is equivalent to the stripping
118 selection in an analysis using the full stream. The HLT1 and L0 efficiencies can be
119 measured in a data driven way as the HLT2 line makes no L0 or HLT1 requirements.

120 The Turbo stream candidates are further refined by an offline selection which is detailed
121 in Sec. 3.2.

122 The total efficiency determined with simulation is split into several successive compo-
123 nents, allowing for calibration of each component independently. In order to determine the
124 efficiency for each component separately, the simulation is reconstructed (offline reconstruc-
125 tion) with loose pre-selections, in particular the muon identification (ID) and the trigger
126 requirements are not applied. The offline reconstruction can be an official one as stripping
127 or a private reconstruction with the same tools as official reconstruction. The private
128 reconstruction and stripping are resulting in the same collection of candidates, which are
129 collectively named offline candidates. To study the quality of online-offline matching, the
130 offline reconstructed candidates are compared to the Turbo stream candidates, and an
131 offline-online matching efficiency is obtained. However, since online and offline reconstruc-
132 tion is made as similar as possible, the matching between offline reconstructed candidates
133 and Turbo stream candidates are almost perfect with a difference of merely 0.1%, which
134 is good enough for our analysis (The correction is not applied for this small value). The
135 comparison is studied with simulation as shown in appendix I.

136 3.2 Offline selection refinement

137 *Editor: Svende Braun*

138 The offline selections are applied to J/ψ candidates to reduce the combinatorial background
139 to a reasonable level and ensure the good quality of the signal-extraction fit. First, each

Variable	Value
Track χ^2/ndf	< 4
Muon Identification	isMuon
vertex χ^2/ndf	< 25
Mass cut	$ m - M(J/\psi) < 150 \text{ MeV}$

Table 3.2: HLT2DiMuonJPsi selection criteria

event is required to have at least one primary vertex (PV) reconstructed, in order to utilize the decay time information. To remove possible clone tracks, the Kullback-Leibler (KL) distance [54] between two particles of less than 5000 is used to suppress duplicate particles created by the reconstruction, only the particle with the higher track fit quality is used and it reduces the clone rate to the level of 0.5×10^{-3} . The final state tracks are required to have a good fit quality, $\chi^2/\text{ndf} < 3$, and are identified as muons with the algorithm described in 3.2.1, and the track is required to prefer a muon hypothesis to a pion hypothesis $\text{DLL}_{\mu\pi} > 0$ as given by the combined PID. The muons are more signal-like by requiring ghost probability for each track ($\mu^+\mu^-$) to be less than 0.3. The momentum of each muon is required to be in the range $3 < p_\mu < 500 \text{ GeV}/c$, and transverse momentum p_T to be greater than $700 \text{ MeV}/c$. The two muons are required to form a good vertex by asking the vertex fit $\text{Prob}(\chi^2/\text{ndf}) > 0.5\%$, and have invariant mass within $150 \text{ MeV}/c^2$ of J/ψ PDG mass value. The pseudo-proper time, t_z , is required to be in the range $-10 < t_z < 10 \text{ ps}$, and its uncertainty to be less than 0.3 ps . The pseudo-proper time of the J/ψ is defined as

$$t_z = \frac{(z_{J/\psi} - z_{\text{PV}}) \times M_{J/\psi}}{p_z}, \quad (3.1)$$

where $z_{J/\psi}$ is the z position of the J/ψ decay vertex, z_{PV} that of the primary vertex. p_z the measured J/ψ momentum along the beam axis z , and $M_{J/\psi}$ the known J/ψ mass [55]. The PV is not refitted removing the two muon tracks from the J/ψ candidate, and studies with simulation shows that we can get correctly the J/ψ -from-b fraction from the fit using the sample without the PV refit, compared to the MC truth J/ψ -from-b fraction. The details of the fit are given in section 5. For event with multiple PV reconstructed (PileUp), the J/ψ candidate is associated to the PV with smallest χ_{IP}^2 .

Although some of these selections are already present in the triggers and muonID requirement, we think it's better to apply them explicitly in the simulation as reconstruction and selection efficiency, instead of hiding them inside other requirements. The selection criteria are summarized in Table 3.3.

3.2.1 MuonID strategy

A simple muon identification algorithm is used to identify muon candidates [56]. A track reconstructed by the LHCb tracking system is extrapolated to the muon stations and hits are searched around the extrapolation in some Field of Interest (FOI). The track is

Variable	Value
number of PV	> 0
Track χ^2/ndf	< 3
Muon Identification	$\text{isMuon}, \text{DLL}_{\mu\pi} > 0.$
Muon p_T	$> 700 \text{ MeV}/c$
Muon p	$3 < p < 500 \text{ GeV}/c$
Track ghost probability $P(\text{ghost})$	< 0.3
Vertex fit probability $P(\chi^2/\text{ndf})$	$> 0.5\%$
Mass cut	$ m(\mu^+\mu^-) - M(J/\psi) < 150 \text{ MeV}/c^2$
Pseudo proper time	$ t_z < 10 \text{ ps}$
Uncertainty of t_z	$< 0.3 \text{ ps}$
KL	> 5000
luminous region	$ z_{\text{PV}} < 227 \text{ mm}, y_{\text{PV}} < 1 \text{ mm}$

Table 3.3: Offline selection criteria

170 identified as a muon if at least a hit is found in each FOI of the required stations, which
171 depends on the momentum of the track, shown in Table 3.4. The muon ID is determined
172 with simulated samples by counting the fractions of signal J/ψ candidates with both tracks
173 identified as muons. This efficiency is calibrated using muon tracks from real data as
studied in section 7.2.

momentum range	required stations
$3 < p < 6 \text{ GeV}/c$	M2+M3
$6 < p < 10 \text{ GeV}/c$	M2+M3+(M4 or M5)
$p > 10 \text{ GeV}/c$	M2+M3+M4+M5

Table 3.4: Stations of the muon system required to identify muons for different momentum range.

174

175 4 Cross-section determination

176 The determination of the double-differential production cross-section requires knowledge
177 of the numbers of prompt J/ψ and J/ψ from b -hadron decays in bins of the kinematic
178 variables y and p_T . This is done by performing a simultaneous fit to the distributions
179 of the dimuon invariant mass and the pseudo-proper time t_z in each kinematic bin. The
180 t_z of promptly produced J/ψ signals has zero lifetime, while the t_z distribution for J/ψ
181 from b is approximately exponential as seen from simulation. The pseudo-proper time t_z
182 allows us to statistically separate the prompt J/ψ from the J/ψ mesons created in decays
183 of b -hadrons.

184 The double differential cross-section for prompt and J/ψ from- b production in a given

185 (p_T, y) bin is defined as

$$\frac{d^2\sigma}{dydp_T} = \frac{N(J/\psi \rightarrow \mu^+\mu^-)}{\mathcal{L} \times \varepsilon_{\text{tot}} \times \mathcal{B}(J/\psi \rightarrow \mu^+\mu^-) \times \Delta y \times \Delta p_T} \quad (4.1)$$

186 where

187 * $N(J/\psi \rightarrow \mu^+\mu^-)$ is either the number of prompt J/ψ or J/ψ from b -hadron signals
 188 reconstructed through the dimuon decay channel; it is obtained by the fit described
 189 in section 5;

190 * \mathcal{L} is the integrated luminosity.

191 * ε_{tot} is the total efficiency, described in detail in Section 6;

192 * $\mathcal{B}(J/\psi \rightarrow \mu^+\mu^-) = (5.961 \pm 0.033)\%$ is the branching fraction of the decay $J/\psi \rightarrow$
 193 $\mu^+\mu^-$, obtained from the PDG 2014 review [55];

194 * $\Delta p_T = 1 \text{ GeV}/c$ is the bin width of the J/ψ transverse momentum;

195 * $\Delta y = 0.5$ is the bin width of the J/ψ rapidity.

196 The following boundaries are used for the binning scheme of p_T and y of the J/ψ
 197 meson:

- 198 • p_T boundaries [GeV/ c]: 0, 1, 2, 3, 4, 5, 6, 7, 8, 9, 10, 11, 12, 13, 14;
- 199 • y boundaries: 2.0, 2.5, 3.0, 3.5, 4.0, 4.5.

200 In each bin, the efficiency ε_{tot} is assumed to be constant as a function of p_T and y in the
 201 small ranges, and thus a single number with corresponding uncertainty is provided. The
 202 efficiency for prompt J/ψ and J/ψ from b are calculated separately, except for the cases
 203 where there is no reasons that the two components have different efficiencies, the same
 204 efficiencies are used (after consistency being checked).

205 5 Signal extraction

206 *Editor: Svende Braun, Yanxi Zhang, Liupan*

207 The number of inclusive J/ψ signals in data is determined with an extended unbinned
 208 maximum likelihood fit to the invariant mass distribution. The distribution of the
 209 background is modelled with an exponential function. The signal is described by the sum
 210 of two Crystal Ball (CB) functions [57] with common mean value (μ) and different widths
 211 (σ_1 and σ_2), where one CB is defined as:

$$f(M_{\mu\mu}) = \begin{cases} \exp(-\frac{(M_{\mu\mu}-\mu)^2}{2\sigma^2}) & \text{for } \frac{M_{\mu\mu}-\mu}{\sigma} > -a \\ A \cdot (B - \frac{M_{\mu\mu}-\mu}{\sigma})^{-n} & \text{for } \frac{M_{\mu\mu}-\mu}{\sigma} \leq -a \end{cases} \quad (5.1)$$

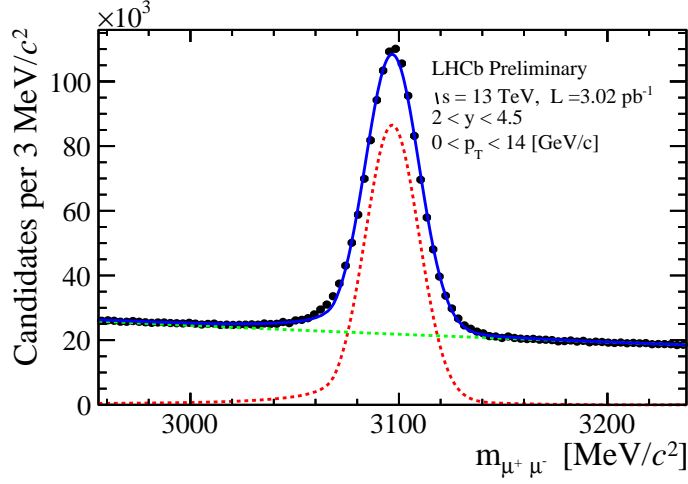


Figure 5.1: Invariant mass distribution of J/ψ candidates with $p_T \in [0, 14]$ GeV/ c and $y \in [2.0, 4.5]$.

in which

$$A = \left(\frac{n}{|a|} \right)^n \cdot \exp \left(-\frac{|a|^2}{2} \right) \quad (5.2)$$

$$B = \frac{n}{|a|} - |a|. \quad (5.3)$$

The tails in both CB functions are used to describe the tail in the dimuon invariant mass distribution due to the loss of energy as a photon is not reconstructed for the radiative decay. The fraction of the narrower CB function is fixed to 0.96 from simulation, the relation between the two widths is parametrized as a linear function, and the slope and the intersection of the linear function are fixed to values obtained from simulation, as discussed in more detail in section C. The a is parametrized as a function of the width, while n is fixed to unity from physics [58]. So there are merely two free parameters for signal mass shape, the μ of the two CB functions and σ_1 of the narrower CB function. These parametrizations can describe the simulated J/ψ sample very well, with a bias of signal yield of about 1%, as studied in section C, this bias is included in the systematic uncertainty calculation due to the mass signal shape in section 7.1.1. For real data this systematic can be obtained by comparing the results of the nominal double CB fits with fit using Hypatia function for the signal, which is found to give almost no bias for signal yield, as studied in section C. However since fitting with Hypatia function is slow, it is not used as the default fit model. In Fig. 5.1, the dimuon invariant mass distribution is shown together with the fit using two CB functions. Practically, the invariant mass fit is performed independent in each p_T and y bin of J/ψ candidates, detailed in section 5.1.

5.1 Determination of the prompt and detached signal yields

The fraction of J/ψ from b -hadron decay is determined by fitting the pseudo-proper time t_z distribution. So in total an unbinned simultaneous maximum likelihood fit to invariant mass $M(J/\psi)$ and t_z is used to disentangle the prompt J/ψ , J/ψ -from- b and combinatorial background. Fits to $M(J/\psi)$ and t_z are performed simultaneously to obtain F_b .

At generator level, pseudo-proper time distribution of the prompt J/ψ is a delta function, $\delta(t_z)$, while that of J/ψ -from- b follows an exponential function as seen from simulation. The effective lifetime of J/ψ -from- b , τ_b is found to be around 1.5 ps from MC simulations, depending slightly on J/ψ kinematics bin compared to the fit results given in appendix D. For fully simulated J/ψ signals, the detector resolution is taken into account by convolving these distribution with a resolution function, which is taken as the sum of two Gaussian functions,

$$f_{\text{resolution}}(t_z; \mu, S_1, S_2, \beta) = \frac{\beta}{\sqrt{2\pi}S_1\sigma} e^{-\frac{(t_z-\mu)^2}{2S_1^2\sigma^2}} + \frac{1-\beta}{\sqrt{2\pi}S_2\sigma} e^{-\frac{(t_z-\mu)^2}{2S_2^2\sigma^2}}, \quad (5.4)$$

where σ is the event-by-event error of t_z , calculated by combining the estimated errors of J/ψ decay vertex and associated PV, S_1 and S_2 are two scale factors to correct the non-perfect estimation of t_z error, μ is the bias of t_z measurement and β is the fraction of one of two Gaussians.

For reconstructed J/ψ candidates, it is possible that the PV that produces the J/ψ decay is not reconstructed and only the nearest reconstructed PV in the event is found; or the J/ψ candidate is associated to a wrong PV in the case that the reconstructed PVs are accidentally close to each other. These two cases are collectively named wrong PV event. In the latter case, the positions of the reconstructed and the true PV are correlated, which results in a Gaussian-like t_z distribution with width much larger than the detection resolution. To describe this effect, one may add a third Gaussian with much larger width than the resolution function. However, from simulation, it is found that by including the wide Gaussian in the resolution doesn't change the fitted parameters significantly because the fraction of this component is quite small, $\leq 1\%$ as seen from studies in section G. Therefore the third wide Gaussian is not used in the fit function.

On the other hand, for the case that the true PV is not reconstructed, the true PV and wrongly associated PV are not correlated, which results in a long tail in the t_z distribution that can be modelled using the next-event method. The next-event pseudo-proper time, t_z^{next} , for each candidate, is calculated combining the J/ψ candidate with the closest PV of another (next) event as

$$t_z^{\text{next}} = \frac{(z_{\mu\mu} - z_{\text{PV}}^{\text{next}}) \times M_{\mu\mu}}{p_z}, \quad (5.5)$$

where $z_{\text{PV}}^{\text{next}}$ is the z -coordinate of the nearest PV of the next event. In Fig. 5.2, the reconstructed t_z distribution is compared with the one with the next-event method t_z^{next} . The region $t_z < -2$ ps is dominated by tail events.¹ From the plot, it is clearly seen

¹The tail also present in region $t_z > 2$ ps, but over dominated by J/ψ from b decay, thus not visible.

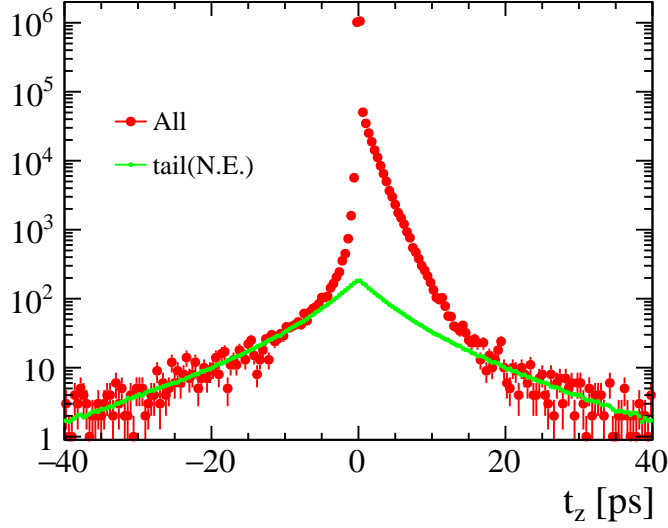


Figure 5.2: t_z distribution for reconstructed events and the one using next event method. The left part of the distribution is normalized to the same area for shape comparison.

that t_z^{next} is a reasonable quantity to model the tail distribution. The tail distribution is not convolved with resolution functions since the distribution is much wider than the resolution, and very smooth in the whole t_z region. It should be noted that since the requirement of PV reconstruction is looser, using at least 4 velo tracks, the probability to reconstruct the true PV is very high ($> 99\%$).

The J/ψ candidates in the mass sidebands, $60 < |M_{\mu\mu} - M(J/\psi)| < 150 \text{ MeV}/c^2$, are used to explicitly model the background t_z distribution. The background consists of random combinations of muons from semi-leptonic b and c decays, which tend to produce positive t_z values, as well as mis-reconstructed tracks from decays-in-flight of kaons and pions which contribute both to positive and negative t_z values. The background t_z is modelled with an empirical function, composed of a delta function and five exponentials (three for positive t_z and two for negative t_z , with one positive t_z and one negative sharing the same slope). This function is convolved with the sum of two Gaussian function as a resolution function, which has different parameters as for signals,² as,

$$f_{\text{background}} = \left[(1 - f_1 - f_2 - f_3 - f_4) \delta(t_z) + \theta(t_z) \left(\frac{f_1}{\tau_1} e^{-t_z/\tau_1} + \frac{f_2}{\tau_2} e^{-t_z/\tau_2} \right) + \theta(-t_z) \left(\frac{f_3}{\tau_3} e^{t_z/\tau_3} + \frac{f_4}{2\tau_4} e^{-|t_z|/\tau_4} \right) \right] * \left(\frac{\beta'}{\sqrt{2\pi} S'_1 \sigma} e^{-\frac{(t_z - \mu)^2}{2S'^2_1 \sigma^2}} + \frac{1 - \beta'}{\sqrt{2\pi} S'_2 \sigma} e^{-\frac{(t_z - \mu)^2}{2S'^2_2 \sigma^2}} \right). \quad (5.6)$$

The parameters in equation 5.6 are determined by fitting the mass sidebands, and are fixed for the final fit. In Fig. 5.3, the t_z background distribution for the kinematic range

²The uncertainty on the background vertex is usually worse than the one for signal.

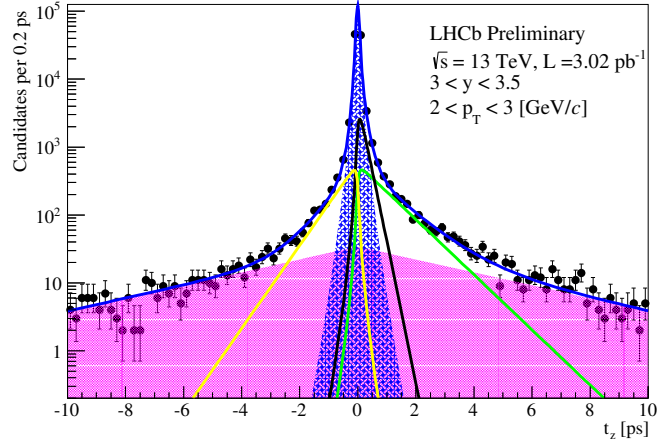


Figure 5.3: Background t_z distribution for J/ψ bin $p_T \in [2, 3]$ GeV/c, $y \in [3, 3.5]$

281 $p_T \in [2, 3]$ GeV/c, $y \in [3, 3.5]$ is shown together with a fit using equation 5.6. In total, the
 282 eventual function for t_z fit is:

$$F_{t_z}(t_z; N_p, N_t, N_b, N_{\text{BKG}}, \mu, S_1, S_2, \beta, \tau_b) = \left(N_p \delta(t_z) + \frac{N_b}{\tau_b} e^{-t_z/\tau_b} \right) * f_{\text{resolution}}(t_z : \mu, S_1, S_2, \beta) \\ + N_t f_{\text{tail}}(t_z) + N_{\text{BKG}} f_{\text{background}}(t_z), \quad (5.7)$$

283 where N_{BKG} , N_p , N_b and N_t are the number of background, prompt J/ψ , J/ψ -from- b and
 284 wrong PV events, respectively. The number of J/ψ signals in the tail component should
 285 be split into prompt J/ψ and J/ψ from b according to their relative fraction. Due to loose
 286 requirement on PV reconstruction, and the PV is not refitted removing the velo segments
 287 of the muon tracks, it is assumed that prompt J/ψ and J/ψ -from- b have equal probability
 288 that the true PV is not reconstructed, which means the fraction of J/ψ -from- b in the tail
 289 is the same as the one in non tail events, thus the J/ψ -from- b fraction is calculated as
 290 $\frac{N_b}{N_b + N_p}$. To calculate the J/ψ from b fraction at production level, the number obtained in
 291 the fit should be corrected by the efficiency, $\frac{N_b/\epsilon_b}{N_b/\epsilon_b + N_p/\epsilon_p}$, since the efficiency for prompt
 292 J/ψ and J/ψ from b is slightly different; more details are given in section 6. Usually, PV
 293 producing J/ψ -from- b have more tracks and are more efficient to be reconstructed, thus
 294 the fraction of J/ψ -from- b in tail is slightly smaller, however since the fraction of tail
 295 events are found to be small ($< 0.5\%$), the effect to the measured J/ψ -from- b fraction is
 296 negligible ($< 0.5\%$).

297 The fit is performed independently in each p_T and y bin of J/ψ mesons. The fitted
 298 parameters are give in appendix D. In Fig. 5.4, the invariant mass and t_z distributions
 299 together with the fits are shown for the range of $3 < p_T < 4$ GeV/c, $2.5 < y < 3$.

300 In Tables D.1, D.2, D.3, D.4 and D.5, the best fit parameters of the mass and t_z fits are
 301 given. In section D, the fitted parameters are also plotted as a function of p_T in bins of y .

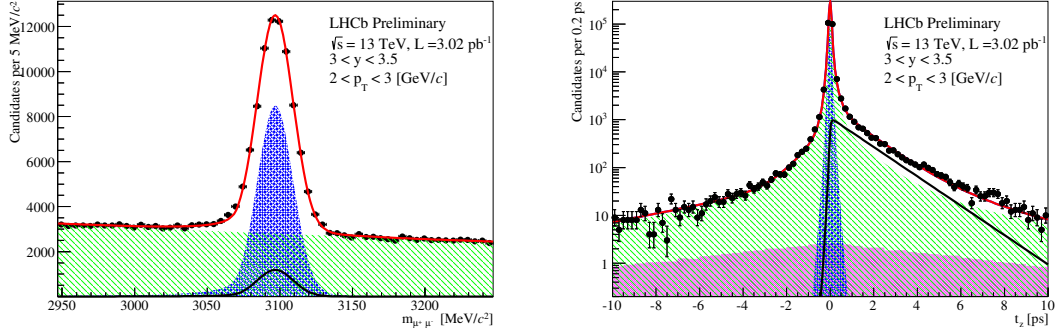


Figure 5.4: (Left) Invariant mass and (Right) pseudo-proper decay time fit result for the kinematic bin $2 < p_T < 3 \text{ GeV}/c$, $3 < y < 3.5$.

6 Efficiency determination

The total efficiency ϵ_{tot} is determined independently in each bin of J/ψ kinematics, split as follows

$$\epsilon_{\text{tot}} = \epsilon_{\text{acc}} \times \epsilon_{\text{Reco\&Sel}} \times \epsilon_{\text{MuonID}} \times \epsilon_{\text{Trigger}}, \quad (6.1)$$

which is the multiplication of the efficiency of geometrical acceptance, reconstruction-selection, muon identification and trigger, respectively.

The efficiency is calculated in each bin of J/ψ p_T and y separately, using Monte Carlo samples reconstructed as offline. These efficiencies are determined using truth matched candidates, and the truth matching efficiency is not present for real data, in which the signal candidates are determined with invariant mass fit. The number of not matched signal candidates is determined by fitting the invariant mass distribution of the not matched candidates. It is found that truth-matching inefficiency is around 0.3%, which is negligible compared to the statistical and systematic uncertainties.

It should be noted that for simulation, both Turbo stream (“online”) and offline reconstructions (offline) are used. The Turbo stream simulates the reconstruction of real data (online), while offline is used to determine the efficiency. The imperfect matching between online and offline in simulation introduces another efficiency correction, as studied in details in appendix I. Since the difference is small (0.1%), we neglect the effect, and don’t apply the correction due to imperfect matching.

In the simulation sample, the prompt J/ψ and J/ψ from b decays are separated using MC truth information. For each efficiency component, the one for prompt J/ψ and J/ψ from b decays is calculated independently, unless when there is no reason that the prompt J/ψ and J/ψ from b have different efficiency (details for each efficiency given below).

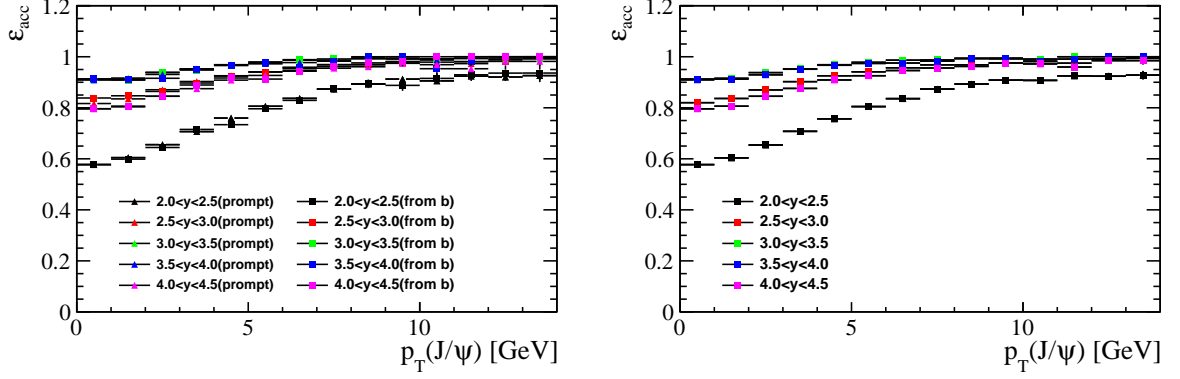


Figure 6.1: Geometrical acceptance ϵ_{acc} calculated using simulated events as a function of p_T in bins of y . The right figure shows the average between efficiency of prompt J/ψ and J/ψ from b .

6.1 Geometrical acceptance

The geometrical acceptance is defined as

$$\epsilon_{\text{acc}} \equiv \frac{J/\psi \text{ with both } \mu \text{ in LHCb acceptance}}{\text{Generated } J/\psi}. \quad (6.2)$$

The LHCb acceptance means the polar angle $[10, 400]$ mrad defined with respect to the direction of LHCb z -axis, before entering the magnet. The efficiency ϵ_{acc} is determined using a simulation sample which has not any geometrical acceptance requirement on the muons. In Fig. 6.1, the efficiency in each p_T and y bin of the J/ψ meson is shown for prompt J/ψ and J/ψ from b , and is summarized in tables E.1 and E.2 in appendix E. Since the prompt J/ψ and J/ψ from b has similar efficiency, the average of the efficiency between prompt J/ψ and J/ψ from b is used to increase the statistics, shown in the right plot of Fig. 6.1 and summarized in table E.3.

6.2 Reconstruction-selection efficiency

The reconstruction and selection efficiency is estimated as

$$\epsilon_{\text{Reco\&Sel}} \equiv \frac{J/\psi \text{ reconstructed and selected (w/o } \mu\text{ID)}}{J/\psi \text{ with both } \mu \text{ in LHCb acceptance}}. \quad (6.3)$$

It includes the efficiency of reconstructing the two muon tracks and the refinement of the J/ψ signals, with the selections that are listed in Table 3.3 (excluding muon identification). For each p_T and y bin, the efficiency of $\epsilon_{\text{Reco\&Sel}}$ is shown in Fig. 6.2, and summarized in tables E.4 and E.5 in appendix E for prompt J/ψ and J/ψ from b . The reconstruction-selection efficiency for prompt J/ψ and J/ψ from b are slightly different because (1) J/ψ from b events have large track multiplicities thus smaller tracking efficiency (2) J/ψ from b events have a lifetime around 1.5 ps, which results in a small fraction of events leaking out

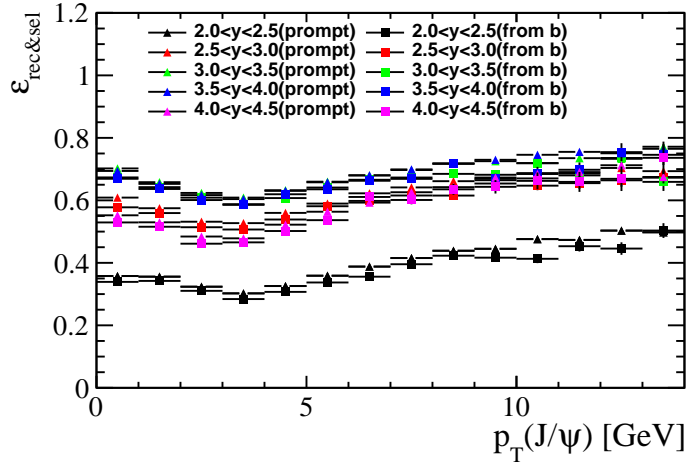


Figure 6.2: Reconstruction-Selection efficiency $\epsilon_{\text{Reco\&Sel}}$ calculated using simulated events as a function of p_T in bins of y .

outside the $|t_z| < 10$ ps cut window. Since the prompt J/ψ and J/ψ from b have slightly different efficiencies, the prompt J/ψ and J/ψ from b efficiencies are determined separately.

Studies show that the tracking efficiency is slightly different between simulation and data, as a result, the reconstruction efficiency in simulation is corrected as a function of the kinematics of the two muons. The correction factors in bins of muon kinematics, given in Fig. 7.4, are provided from the tracking group, by comparing the absolute tracking efficiency in data and simulation. The corrections depend on J/ψ kinematic bins, with values of a few percent. The details of the tracking correction is given in section 7.3.

6.3 Muon identification efficiency

The efficiency introduced by muon identification requirements is given by

$$\epsilon_{\text{MuonID}} \equiv \frac{J/\psi \text{ selected including } \mu\text{ID requirement}}{J/\psi \text{ reconstructed and selected (w/o } \mu\text{ID)}}. \quad (6.4)$$

For each p_T and y bin, the efficiency of ϵ_{MuonID} is shown in Fig. 6.3, and summarized in tables E.6 and E.7 in appendix E for prompt J/ψ and J/ψ from b . These efficiencies determined from simulation are cross checked with real data. To reduce the statistical fluctuation, the cross check is performed combining all J/ψ kinematic bins instead of bin by bin. The calibration efficiency is determined by convolving the kinematics dependent single track muonID efficiency determined from calibration data sample with the muon kinematics in simulation. The ratio between the calibrated efficiency and the efficiency in simulation, 1.02, is used to correct the muonID efficiency in simulation. The details are shown in section 7.2. Since the prompt J/ψ and J/ψ from b has similar efficiency, the average of the efficiency between prompt J/ψ and J/ψ from b is used to increase the statistics, shown in the right plot of Fig. 6.3 and summarized in table E.8.

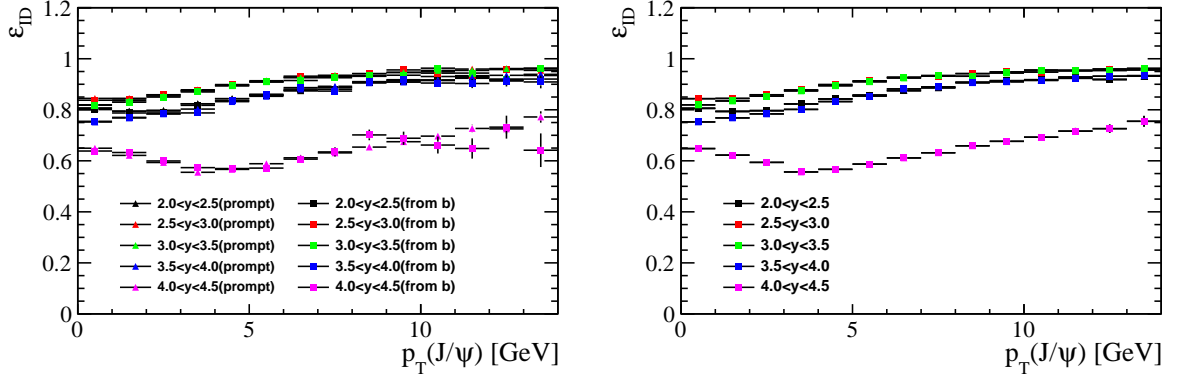


Figure 6.3: MuonID efficiency ϵ_{MuonID} calculated using simulated events as a function of p_T in bins of y . The right figure shows the average between efficiency of prompt J/ψ and J/ψ from b .

6.4 Trigger efficiency

The trigger efficiency is defined as

$$\epsilon_{\text{Trigger}} \equiv \frac{J/\psi \text{ triggered}}{J/\psi \text{ selected including } \mu\text{ID requirement}} \quad (6.5)$$

Here the triggers include both `L0Muon`, `Hlt1DiMuonHighMass` and `Hlt2DiMuonJPsiTurbo`. Only `L0Muon` and `Hlt1DiMuonHighMass` contribute actually to the efficiency, because the `Hlt2DiMuonJPsiTurbo` trigger is almost fully efficient ($> 99.7\%$ obtained with stripping data sample) due to the facts that the offline selections are much tighter than those in `Hlt2DiMuonJPsiTurbo` and the same reconstruction procedure and tools are implemented online and offline. For each p_T and y bin, the efficiency of $\epsilon_{\text{Trigger}}$ is shown in Fig. 6.4, and summarized in tables E.9 and E.10 in appendix E for prompt J/ψ and J/ψ from b . Since the prompt J/ψ and J/ψ from b has similar efficiency, the average of the efficiency between prompt J/ψ and J/ψ from b is used to increase the statistics, shown in the right plot of Fig. 6.4 and summarized in table E.11.

6.5 Total efficiency

The total efficiency ϵ_{tot} is shown in Fig. 6.5 for prompt J/ψ and J/ψ from b , and is summarized in tables E.12 and E.13 in appendix E. It should be noted that the total efficiency is corrected with a small amount for MuonID efficiency (5%) and tracking efficiency (a few percent depending on J/ψ kinematic bins), with calibrations from real data; and the correction factors are presented separately in the following sections.

7 Systematic uncertainties

The following sources of systematic uncertainty are considered.

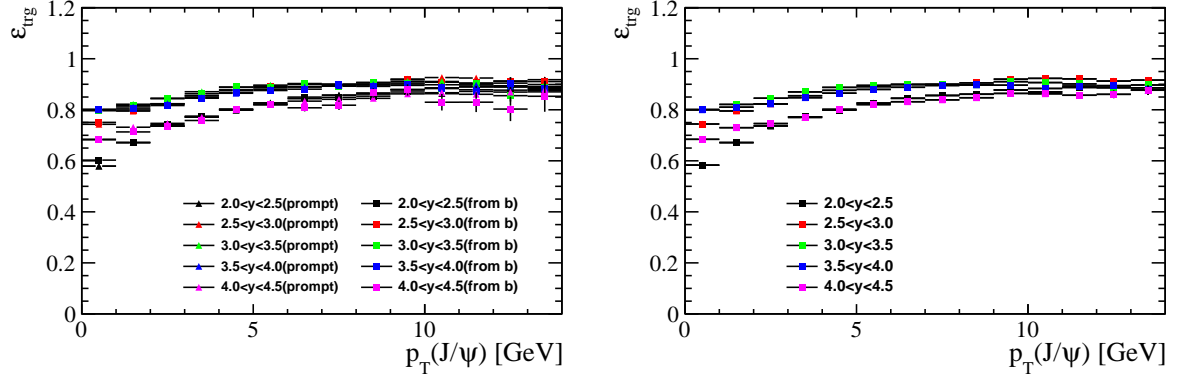


Figure 6.4: Trigger efficiency $\epsilon_{\text{Trigger}}$ calculated using simulated events as a function of p_T in bins of y . The right figure shows the average between efficiency of prompt J/ψ and J/ψ from b .

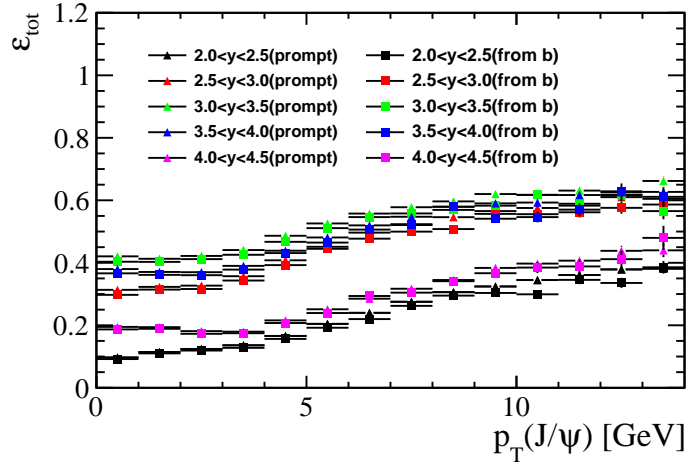


Figure 6.5: Total efficiency ϵ_{tot} calculated using simulated events as a function of p_T in bins of y . The numbers of acceptance efficiency, muon ID efficiency and trigger efficiency for prompt J/ψ and J/ψ from b are taken to be the same.

7.1 Signal extraction

7.1.1 Signal mass shape

Studies of the fits to full MC simulation show that using the sum of two Crystal Ball function parametrized as in this analysis bias the signal yield of about 1% as shown in appendix C. For an alternative, the signal invariant mass is also fitted with the Hypatia function [59], which effectively takes into account the event-by-event variation of mass resolution. Since this bias is almost constant over all bins as shown in C, to reduce the effect of statistical fluctuation, the study is performed in a high statistics kinematic bins; and the signal yield is compared. The relative difference between the nominal fit and

393 Hypathia fit is 0.0097 and therefore 1%, is quoted as the systematic uncertainty, and is
 394 considered as correlated across J/ψ kinematic bins.

395 7.1.2 Fit to t_z

396 There are several scenarios that could deviate the fitted b fraction from its true value:

- 397 • Imperfect modelling of the detector resolution of t_z . Since the shape of prompt J/ψ
 398 is dominated by the resolution, a defective description of resolution could make the
 399 prompt J/ψ distribution not fitted very well, and thus will affect the fitted J/ψ from
 400 b fraction. To study this effect, a third wide Gaussian is added to the resolution
 401 function. As a result, it is found that the variation of the fitted F_b is negligible as
 402 studied in G.
- 403 • Systematic uncertainties related to the background description. The cFit explicitly
 404 models the background distribution using mass sidebands. Since the amount of mass
 405 sidebands available is limited, the background parameters can also be obtained from
 406 the s-weighted invariant mass distribution and will be fixed for the t_z fit. The change
 407 of the J/ψ from b fraction with the alternative method is only 0.05%.
- 408 • Systematic errors due to the long tail t_z description. The nominal approach to
 409 describe the tail is the next-event method, defined in section 5.1. A second approach
 410 is used to describe tail with an analytical function of a bifurcated exponential with
 411 equal slopes on the positive and negative sides. Here the slope parameter can be
 412 left free in the t_z fit. The difference of F_b between the fits is taken as a systematic
 413 uncertainty, and is relatively 0.073%, which is small due to the fact that the tail is
 414 rather small.

415 In total the systematic uncertainty due to t_z fit models are only 0.1%.

416 7.2 MuonID efficiency

417 *Editor: Yanxi Zhang and Liupan An*

418 The muon ID efficiency is calibrated with muon tracks using data taken in the same period
 419 as this analysis. The single track muon identification efficiency is determined using a
 420 tag-probe method with J/ψ candidates from data. One of the J/ψ daughters is identified
 421 as a muon (the tag leg) to reduce the combinatorial background, while the other muon (the
 422 probe track) has no muon identification requirements. The calibration sample has been
 423 prepared carefully asking the probe muon to be independent of any muon triggers (TIS),
 424 to avoid biases on the result. The single track muon identification efficiency is evaluated
 425 as the number of J/ψ signals in this calibration sample with the probe track identified as
 426 a muon divided by total J/ψ signals. The number of J/ψ signals are determined using
 427 a fit to the invariant mass distribution. Since the statistics of this sample is not very
 428 large, the systematic uncertainty due to signal extraction, which is much smaller than
 429 statistical uncertainties, is not taken into account. The single track efficiency is calculated

as a function of the probe muon momentum p_μ and pseudo-rapidity η_μ . The single track efficiency depends also (but only weakly) on the track multiplicity in the event. However the track multiplicity is found to be similar in the calibration and the analysis sample. In Fig. 7.1, the single track muon ID efficiency in calibration sample is shown. For η_μ bins at the boundary, they are extended to include outliers.

The efficiency determined in the calibration sample is used to calibrate the simulation muonID efficiency by averaging the muonID efficiency of each event, which is the product of the two muon ID efficiencies assigned according to their kinematics in the calibration table as

$$\bar{\epsilon} = \frac{\sum \epsilon_{\mu^+}(p_{\mu^+}, \eta_{\mu^+}) \epsilon_{\mu^-}(p_{\mu^-}, \eta_{\mu^-})}{N_{\text{rec\&sel}}}. \quad (7.1)$$

The calibration of the muonID efficiency is performed by combining all the kinematic bins of J/ψ , namely $p_T < 14 \text{ GeV}/c$, $2 < y < 4.5$. The ratio of the calibrated efficiency divided by the efficiency in simulation, 1.05, is used to correct the simulated PID in each J/ψ kinematic bin of the analysis. This factor is used to multiply the efficiency calculated for each kinematic bin in section 6 for the Muon ID efficiency.

The systematic uncertainty of the calibration (correction factor) includes the following contributions:

- statistical uncertainty due to the finite size of the calibration sample, which is studied using the toy MC method to be 1.7%.
- uncertainty due to binning scheme of the calibration sample, studied by varying the number of bins in p_μ and η_μ respectively, and the quadratic sum of the differences is quoted, which is 0.7%.
- discrepancy of track multiplicity in calibration sample and analysis sample. Since in the Turbo data sample, the total track multiplicity is available but the number of long tracks plus number of downstream tracks, we use the number of SPD hits as a proxy for the event activities. We reweight the SPD hits multiplicity in calibration sample to that in data sample when extracting the single track efficiency. The variation of the calibration efficiency on average is 0.2%, which is very small.

The combination of the components above gives a value of 1.8%, which is quoted as the PID systematic uncertainty and is correlated in all J/ψ bins.

7.3 Tracking efficiency

Editor: Michael Kolpin

The track reconstruction efficiency is evaluated using the tag-and-probe technique. For that $J/\psi \rightarrow \mu^+ \mu^-$ decays are investigated with three different methods.

While the tag track is a fully reconstructed and tightly selected long track muon, the probe track reconstruction depends on the method used. For the Long method the probe is a **MuonTTTrack**, which uses hit information from the Muon stations and TT. It thus probes the efficiency of the VELO and T stations simultaneously.

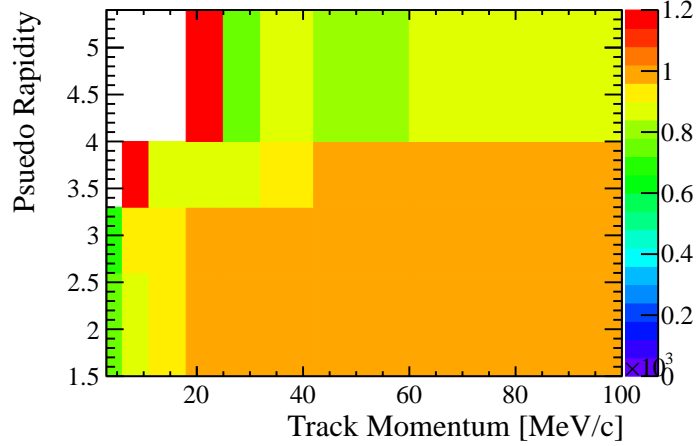


Figure 7.1: Single track muon ID efficiency in calibration sample in bins of p_μ and η_μ of muon.

The VELO method uses Downstream tracks (probing the VELO efficiency) as probes, while the T station method uses **VeloMuon** tracks (using VELO and TT hits), and thus probes the T station efficiency. The combination of VELO and T station methods (assuming factorisation of the long efficiency) should yield the same result as the Long method. The analysis of the data collected during Run I showed good agreement between these Long and combined methods [60].

For the Turbo stream implemented in Run II, dedicated trigger lines are used to reconstruct tag and probe tracks and combine them to a J/ψ as well as select candidates. Furthermore, dedicated lines are matching the probe tracks for these candidates to fully reconstructed long tracks (not using PID information). Kinematic information of the candidates triggering the respective decisions are saved and evaluated using the Tesla framework. This way, the track reconstruction efficiency within the HLT can be investigated.

To investigate the tracking efficiency of the full offline reconstruction, Stripping lines **StrippingTrackEff*** are used for tag and probe reconstruction.

For both the evaluation of offline and online reconstruction, the efficiencies observed on data and MC simulation are evaluated separately, where the efficiency is measured in bins of p and η of the tracks. Besides that the MC samples are reweighted to show the same track multiplicity distributions as data.

The ratio of tracking efficiencies for a single track in data and simulation determined with the Long method is shown in Fig. 7.3, which is used to correct the simulation sample. The combined method gives consistent results. It should be noted that when the single track tracking efficiency is determined, the event multiplicities in simulation have been reweighted to match data, thus when we apply the efficiency correction we have to first reweight the event multiplicity distribution. Here we use number of SPD hits as a multiplicity reweighting variable. Because the event multiplicity in simulation is quite different (smaller) than data as shown in Fig. 7.2, and the efficiency drops with increasing

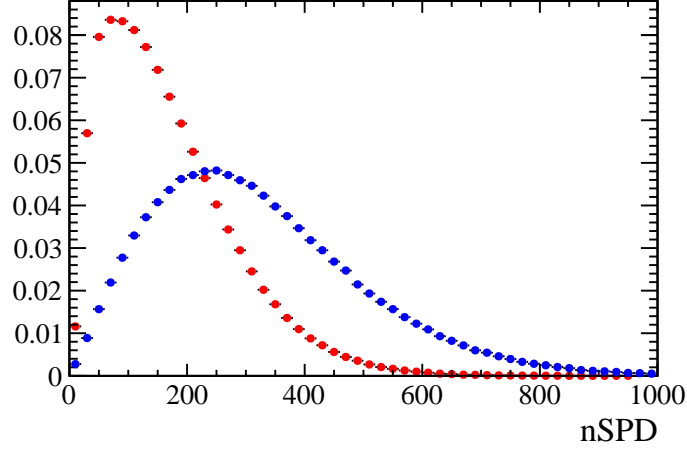


Figure 7.2: Distribution of number of SPD hits for (blue) data and (red) simulation.

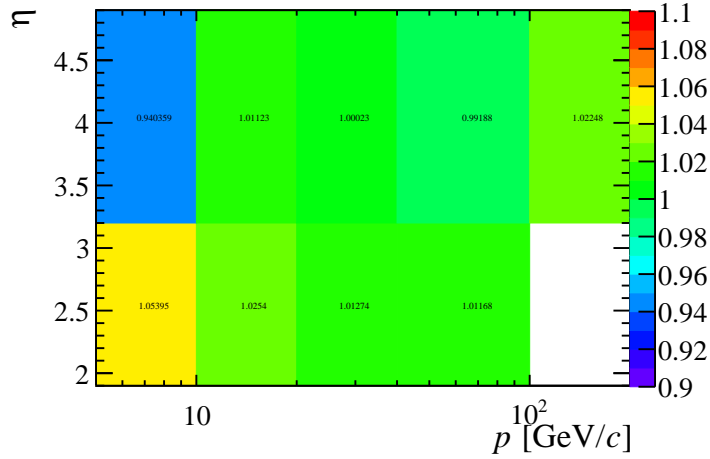


Figure 7.3: Tracking efficiency ratio between data and MC2015 simulation in bins of p_μ and η_μ of muon.

event multiplicity, after multiplicity reweighting the simulation efficiency decreases by 5%, and the drop of efficiency is almost not dependent on J/ψ kinematic bins. After reweight the event multiplicity, the J/ψ reconstruction efficiency is further corrected using the data-over-simulation single tracking efficiency ratio. In total, combining the efficiency loss due to event multiplicity and tracking efficiency correction, the multiplication factor to simulation efficiency is shown in Fig. 7.4 for different p_T and y bin of J/ψ mesons. Since the event multiplicity distribution of prompt J/ψ and J/ψ from b in simulation is quite similar compared to the event multiplicity difference between simulation and data, we assume prompt J/ψ and J/ψ from b have same efficiency corrections.

The systematic uncertainty due to statistical uncertainty of tracking efficiency correction

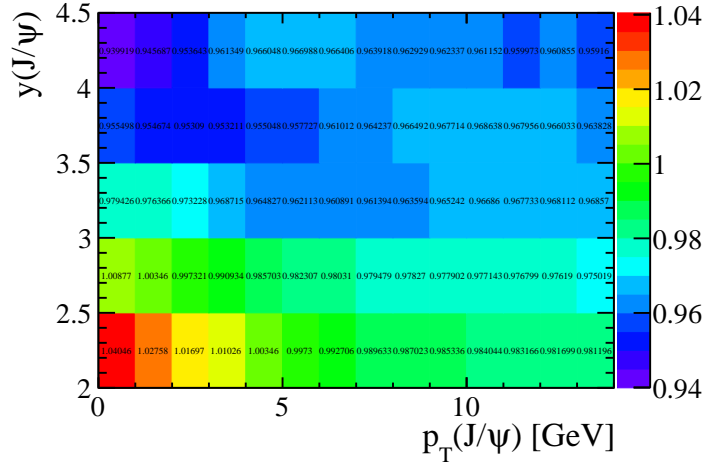


Figure 7.4: Tracking efficiency correction factor in bins of J/ψ p_T and y .

table is propagated using toy MC method, resulting values of around 1.%, depending
 J/ψ (p_T, y) bins. The choice of event multiplicity variable is another source of systematic
uncertainty and has been found to be 0.4% per track.

7.4 Offline selection efficiency

Editor: Svende Braun

The systematic uncertainty of the offline selection related to kinematic variables are treated
as due to unknown spectrum and is studied in section 7.6. The cuts on track quality and
track ghost probability are very loose, and their systematic effects are taken into account
by tracking efficiency systematic in section 7.3. Simulation shows that the probability to
reconstruct the primary vertex that produces J/ψ is larger 95%, however due to pile up,
when the true PV is lost, there is a large chance that an accompanying PV is reconstructed
and associated. For simulation with $\nu = 1.6$ the PV association efficiency, the probability
that a reconstructed J/ψ is associated to a reconstructed primary vertex, is $> 99.8\%$.
Because of the high PV finding efficiency, the systematic effect due to requirement of at
least one PV in each event is neglected. Similar discussion applies to luminous region cut,
which is almost fully efficient for signals ($\approx 99.9\%$).

In previous studies differences in the efficiency of the vertex quality criteria between
data and MC were seen. The nominal selection cut requires for the vertex fit probability
 $P(\chi^2/\text{ndf}) > 0.5\%$. The vertex fit quality cut is studied by comparing the cut efficiency in
data and simulation for variations of the cuts as can be seen on the left of Fig. 7.5. With
the selection cut a maximum value of 0.36% is observed for the difference of the efficiencies
between data and MC, therefore this is taken into account as a systematic error for the
vertex cut. The efficiency of this cut has also been studied as a function of p_T on the right
of Fig. 7.5 for data and MC. One can see that the efficiency loss only weakly depends on
the J/ψ kinematics.

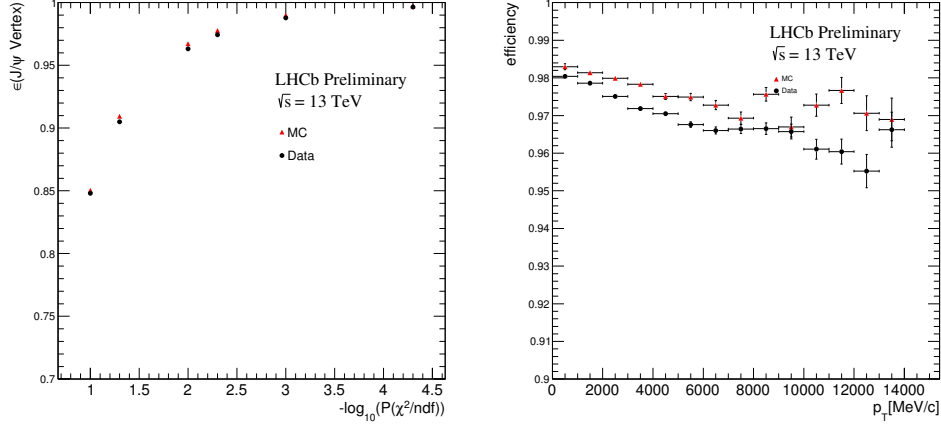


Figure 7.5: The efficiency on the vertex $P(\chi^2/\text{ndf})$ cut in data and simulation, the nominal cut value corresponds to $-\log_{10}(P(\chi^2/\text{ndf})) < 2.3$ (left). The efficiency of the nominal cut vertex probability $P(\chi^2/\text{ndf}) > 0.5\%$ as a function of the J/ψ p_T (right).

7.5 Trigger efficiency

Editor: Tim Head and Christian Linn

The trigger efficiency in simulation is cross checked with data, and the difference between simulation and data are quoted as systematic. For **L0Muon**, tag-and-probe method is used to extract the single track trigger efficiency in simulation and data. The tag-muon is required to fire the **L0Muon** trigger, and the single track trigger efficiency is determined to be the fraction of candidates with probe muon also firing the **L0Muon** trigger. When the efficiency is calculated, the J/ψ has been required to fire the **Hlt1DiMuonHighMass** trigger and matched to a Turbo stream candidate for simulation. The single track efficiency is determined in bins of muon momentum and pseudo-rapidity as $\epsilon(p_\mu, \eta_\mu)$, as shown in Fig. 7.6 for data and simulation respectively. μ^+ and μ^- tracks have different **L0Muon** efficiency especially for data in low p_T and high η bins. From the single track trigger efficiency, the J/ψ trigger efficiency is determined as $\sum (1 - \{(1 - \epsilon(p_{\mu^+}, \eta_{\mu^+}))(1 - \epsilon(p_{\mu^-}, \eta_{\mu^-})\}) / N_{\text{tot}}$, since at least one muon is required to fire the trigger. The relative efficiency difference (in absolute value) between data and simulation in each J/ψ kinematic bin is quoted as a systematic uncertainty. We also studied the variation of the calibrated efficiency with different binning scheme. In Fig. 7.7 the systematic uncertainty (before taking the absolute value) in each J/ψ bin is shown. In most of the bins, the systematic effect is quite small, except in high low p_T high rapidity bins. The **L0Muon** systematic uncertainty in neighboring bins are highly correlated since they uses the same single track muon trigger efficiency.

For **Hlt1DiMuonHighMass**, a TisTos method is used to evaluate the efficiency for simulation and data. In Fig. 7.8, the efficiency for data and simulation are given; the uncertainties are statistical only. The sample size is limited by the number of TIS events. For most of the kinematics bins, simulation and data agree with each other. In Fig. 7.9,

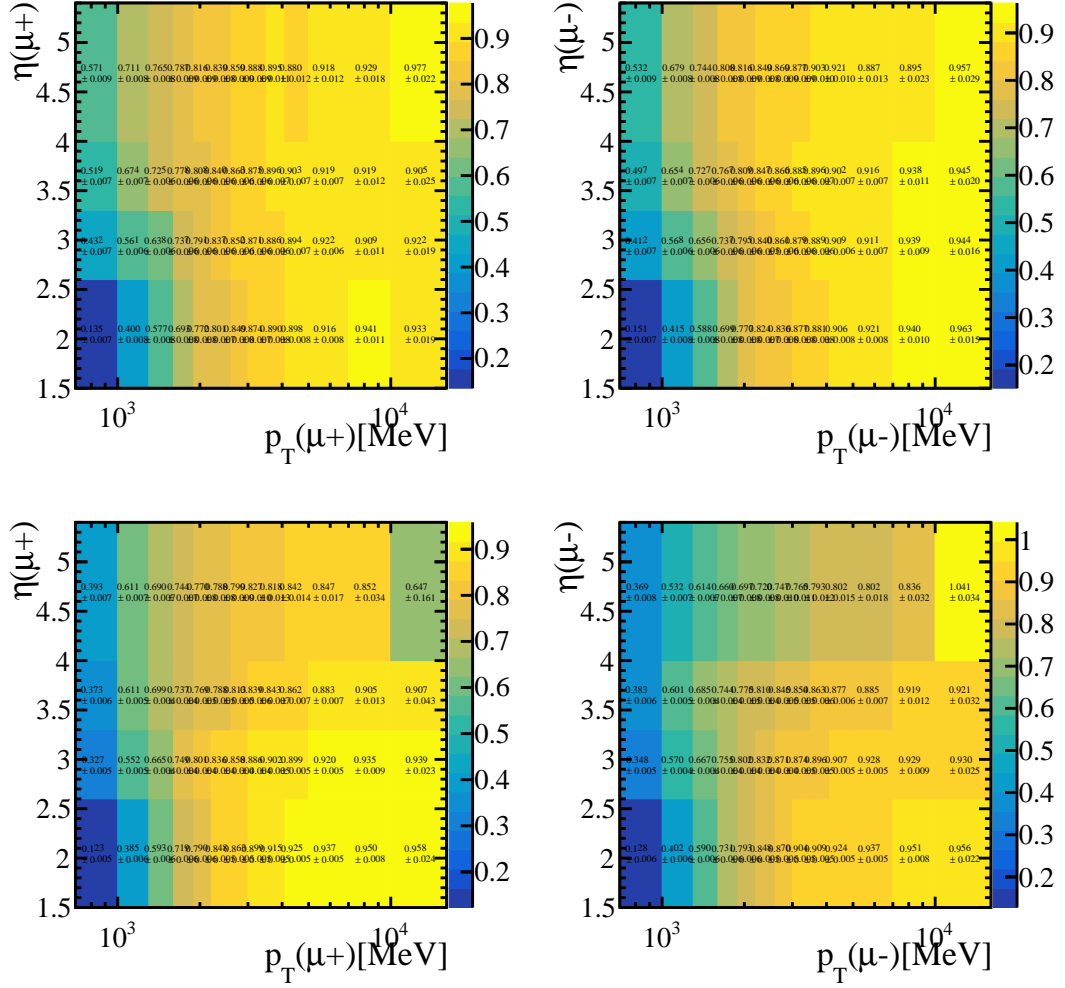


Figure 7.6: The single track L0Muon trigger efficiency determined using tag-probe method in (top) simulation and (bottom) data and (right), for (left) μ^+ and μ^- .

on the left the pull is shown, where pull is define as the relative difference of efficiency
in data over simulation, divided by its uncertainty; while on the right, the ratio of the
efficiency between data and simulation is shown. The fit with Gaussian on the left gives
mean -0.66 ± 0.18 and sigma consistent with one, and the fit with Gaussian on the
right gives mean 0.989 ± 0.003 . Both plots suggest a small inconsistency of Hlt1 trigger
efficiency in simulation and data. If the TisTos efficiency in data is multiplied by 1.015,
the pull distribution will be consistent with a normal distribution and the mean value of
the efficiency ratio distribution is also consistent with zero, so we quote a systematic value
of 1.5% consistent over bins. The systematic quoted this way is equivalent to combining
all kinematic bins to compared different in simulation and data, which gives efficiency of
 0.8776 ± 0.0005 for simulation and 0.864 ± 0.001 for data.

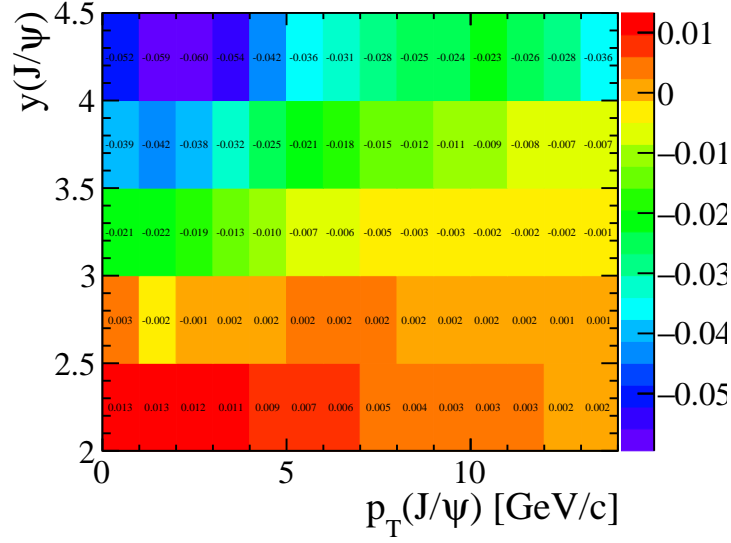


Figure 7.7: L0 muon trigger systematic in each bin of J/ψ kinematics.

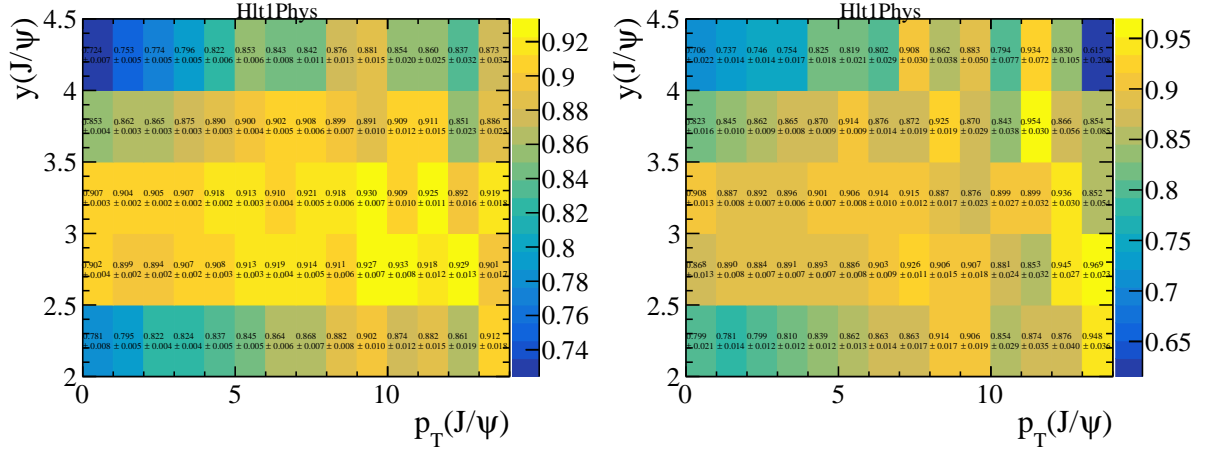


Figure 7.8: Efficiency of Hlt1DiMuonHighMass determined with TisTos method for (left) simulation and (right) data.

7.6 Unknown spectrum

Editor: Yanxi Zhang and Liupan An

For each kinematic bin, the difference of kinematics between simulation and data is a source of systematic uncertainty. The p_T and y distribution in simulation is weighted to the one in background subtracted data, and the efficiency is evaluated again with the weighted kinematic distribution in each bin; the variation of the efficiencies is quoted as systematic uncertainty. In Fig. 7.10, the binning systematic uncertainties for each bin are shown (before taking the absolute values). We assume that prompt J/ψ and J/ψ from b

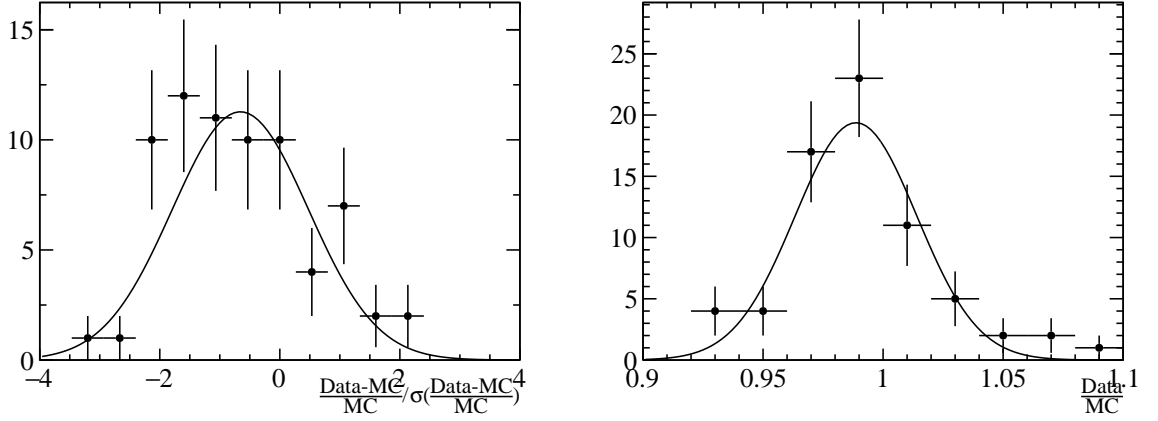


Figure 7.9: Efficiency of `Hlt1DiMuonHighMass` determined with TisTos method for (left) simulation and (right) data.

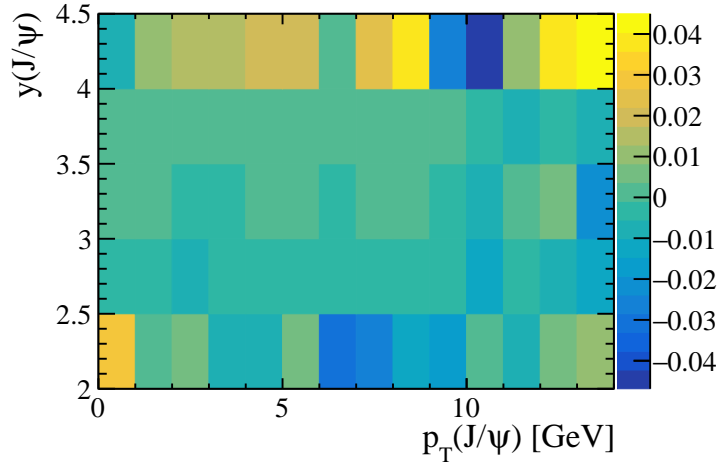


Figure 7.10: Binning systematic uncertainty in each bin of J/ψ kinematics.

decay have the same systematic uncertainties.

7.7 Polarization scenarios

Editor: Yanxi Zhang

The detection efficiency of J/ψ depends on the polarization, which could change the efficiency of about 20% for some kinematic bins, and a few percent for most of the kinematic bins, for extreme polarization scenarios. The LHCb experiment measured the prompt J/ψ polarization in rapidity bins $2 < y < 4.5$ with $2 < p_T < 15 \text{ GeV}/c$ in pp collisions at 7 TeV, and a small, non-zero longitudinal polarization of -0.145 ± 0.0027 is observed in the helicity frame summed over all bins, with no significant dependence on

Table 7.1: The relative increase of the total efficiency (in %), for a -20% polarisation rather than zero, in different bins of p_T and y .

p_T (GeV/c)	$2 < y < 2.5$	$2.5 < y < 3$	$3 < y < 3.5$	$3.5 < y < 4$	$4 < y < 4.5$
0 – 1	6.24 ± 0.35	4.89 ± 0.10	3.45 ± 0.11	3.31 ± 0.09	4.66 ± 0.17
1 – 2	5.58 ± 0.18	4.30 ± 0.07	2.94 ± 0.06	2.55 ± 0.03	2.82 ± 0.12
2 – 3	4.88 ± 0.14	3.47 ± 0.06	1.97 ± 0.04	1.52 ± 0.06	1.65 ± 0.13
3 – 4	4.77 ± 0.14	3.39 ± 0.06	1.94 ± 0.04	1.17 ± 0.07	1.13 ± 0.15
4 – 5	4.68 ± 0.14	3.34 ± 0.08	1.97 ± 0.04	1.20 ± 0.07	0.73 ± 0.14
5 – 6	4.43 ± 0.12	3.28 ± 0.10	2.03 ± 0.06	1.42 ± 0.06	0.75 ± 0.14
6 – 7	4.21 ± 0.09	3.03 ± 0.12	2.05 ± 0.08	1.57 ± 0.04	0.77 ± 0.14
7 – 8	3.88 ± 0.04	2.81 ± 0.15	1.98 ± 0.10	1.69 ± 0.05	0.74 ± 0.14
8 – 9	3.59 ± 0.15	2.65 ± 0.20	1.81 ± 0.11	1.65 ± 0.11	1.01 ± 0.13
9 – 10	3.53 ± 0.18	2.44 ± 0.24	1.81 ± 0.15	1.68 ± 0.16	1.17 ± 0.14
10 – 11	3.39 ± 0.27	2.30 ± 0.26	1.88 ± 0.22	1.73 ± 0.26	1.26 ± 0.14
11 – 12	3.09 ± 0.32	2.18 ± 0.38	1.47 ± 0.18	1.65 ± 0.27	1.35 ± 0.43
12 – 13	3.25 ± 0.45	1.65 ± 0.32	1.93 ± 0.36	1.49 ± 0.26	1.48 ± 0.21
13 – 14	2.72 ± 0.58	1.68 ± 0.32	1.71 ± 0.38	1.17 ± 0.27	1.36 ± 0.51

p_T or rapidity. The ALICE collaboration measured inclusive J/ψ polarization also in the forward kinematic range [26], with values consistent with LHCb. The CMS experiment determined the J/ψ polarization in the p_T range [14, 70] GeV/c and $|y| < 1.2$, the values of the polarization are about $+0.1$ with uncertainty 0.1 for almost all the fiducial regions [27]. So, according to the polarization measurements by LHC runI analysis and CDF, the J/ψ polarization in the LHCb range is expected to be small [39]. If the polarisation is assumed to be $\pm 10\%$, the measured J/ψ cross section would change by values between $\mp 0.3\%$ and $\mp 3.0\%$ depending on the J/ψ kinematic bins. In Fig. 7.11, the relative variation of the efficiency is given for the case of the polarization parameter $\alpha(\lambda_\theta) = 0.1$, which is typical value of J/ψ polarization as measured in RUNI data. The average value of efficiency change is 1.2% which is much smaller than the systematic uncertainty. As a result, in this analysis, we only make the cross section measurements assuming zero polarization and no corresponding systematic uncertainty is quoted on the cross-section related to this effect, before polarization at 13 TeV is measured.

In Table 7.1, the increase of the total efficiency is given for a polarisation of $\lambda_\theta = -20\%$ compared to zero polarisation in bins of (p_T, y) of the J/ψ meson. This information will facilitate the extrapolation of the cross-sections measured with zero polarisation to other polarisation values by scaling from 20% polarisation scenario, and the linearity of the scaling is found to be reasonably good.

7.8 Other systematic uncertainties

- The uncertainty of $\mathcal{B}(J/\psi \rightarrow \mu^+ \mu^-) = (5.961 \pm 0.033)\%$ from [55], is propagated to the cross-section measurement as 0.6% . The fraction of J/ψ from b is not affected.

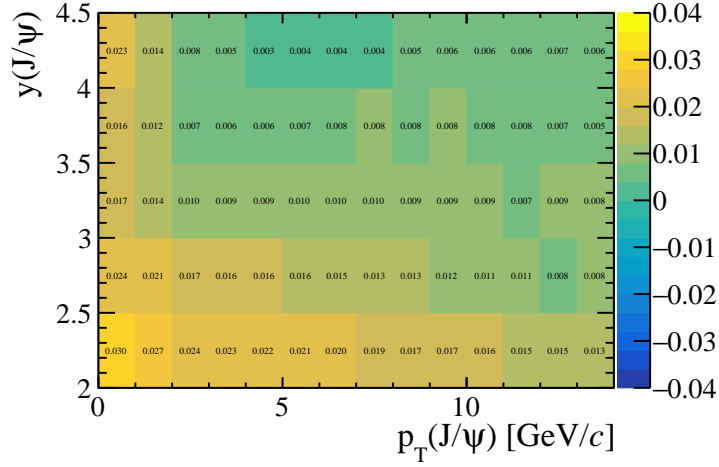


Figure 7.11: Relative variation of efficiency when the polarization is 10%.

- The relative uncertainty of luminosity is 3.9%, which propagates to the cross-sections in each bin equally.
- The limited statistics in simulation sample when the efficiencies are determined is a source of systematic uncertainties, which is between 0.3% and 5% dependent on the kinematic bin. The statistical uncertainty of data is twice as large.
- A fraction of events are lost because of the QED radiative tail. The efficiency of the mass window selections is estimated using simulation, thus the imperfect modelling of the radiative decay would be a source of systematic uncertainty. This has been studied in previous analysis and similar effect is expected, so as in RUN-I analysis a value of 1% is quoted.

7.9 Summary of systematic uncertainties

In table 7.2, the systematic uncertainties are summarized.

8 Results

Editor: Yanxi Zhang, Tim Head

The measured double differential cross-section of prompt J/ψ and J/ψ from b are shown in Figs. 8.1 and 8.2, and are also given in tables F.1 and F.2 in appendix F, for various J/ψ (p_T, y) bins.

The integrated cross-sections for prompt J/ψ and J/ψ from b in the defined acceptance, summing over all bins of the analysis, are:

$$\begin{aligned}\sigma(\text{prompt } J/\psi, p_T < 14 \text{ GeV}/c, 2 < y < 4.5) &= 15.30 \pm 0.03 \pm 0.86 \mu\text{b}, \\ \sigma(J/\psi \text{ from } b, p_T < 14 \text{ GeV}/c, 2 < y < 4.5) &= 2.34 \pm 0.01 \pm 0.13 \mu\text{b},\end{aligned}$$

Table 7.2: Summary of systematic uncertainties

Quantity	Systematic uncertainty	Comment
Luminosity	3.9%	Correlated between bins
L0 Trigger	0.1-5.9%	Correlated between bins
Hlt1 Trigger	1.5%	Correlated between bins
Muon ID	1.8%	Correlated between bins
Tracking	1.1-3.4%	Correlated between bins
Radiative tail	1%	Correlated between bins
Offline selections	0.36%	Correlated between bins
Signal shape	1%	Correlated between bins
$\mathcal{B}(J/\psi \rightarrow \mu^+ \mu^-)$	0.6%	Correlated between bins
p_T - y -spectrum	0.1 -5.0%	Bin dependent
MC statistics	0.3 -5.0%	Bin dependent
t_z fits	0.1%	Affects J/ψ from b

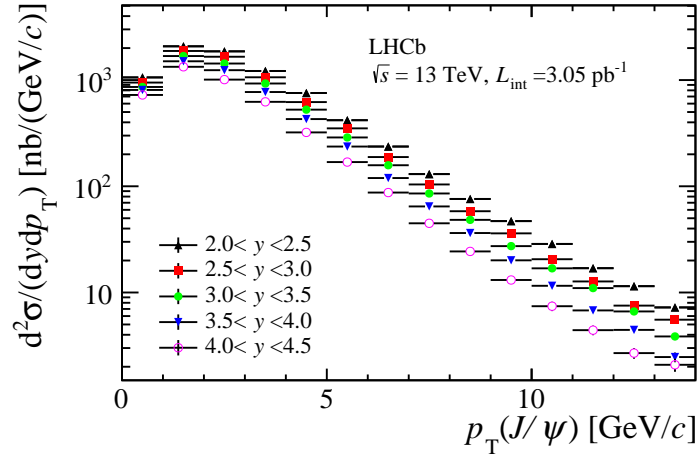


Figure 8.1: Differential cross-section for prompt J/ψ as a function of p_T in bins of y . Statistical and systematic uncertainties are added in quadrature.

where the first uncertainties are statistical and the second systematic.

8.1 Fraction of J/ψ from b

The fraction of J/ψ from b in each kinematic bin is calculated the fitted fraction $N_b/(N_b + N_p)$, corrected by the difference of detection efficiency for prompt J/ψ and J/ψ from b . In Fig. 8.3 and Table 8.1, the fraction of J/ψ from b in different kinematics bins are shown, with the statistical and systematic uncertainties (added in quadrature for the plot). The fraction increases as a function of p_T . For a constant p_T , the b fraction decreases with increasing rapidity, indicating the b -hadrons are produced less forward than prompt J/ψ .

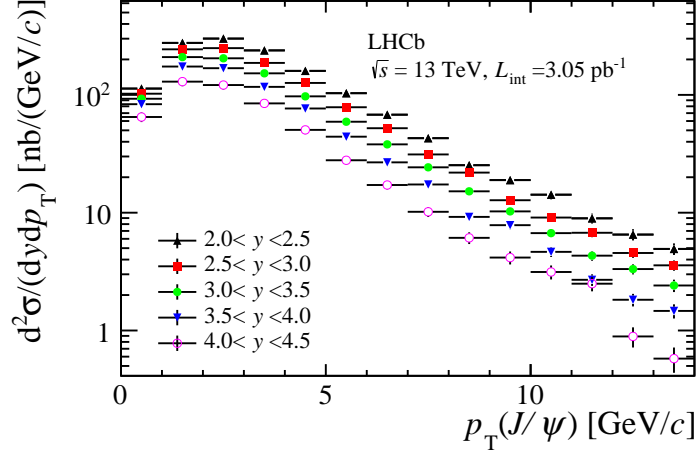


Figure 8.2: Differential cross-section for J/ψ from b as a function of p_T in bins of y . Statistical and systematic uncertainties are added in quadrature.

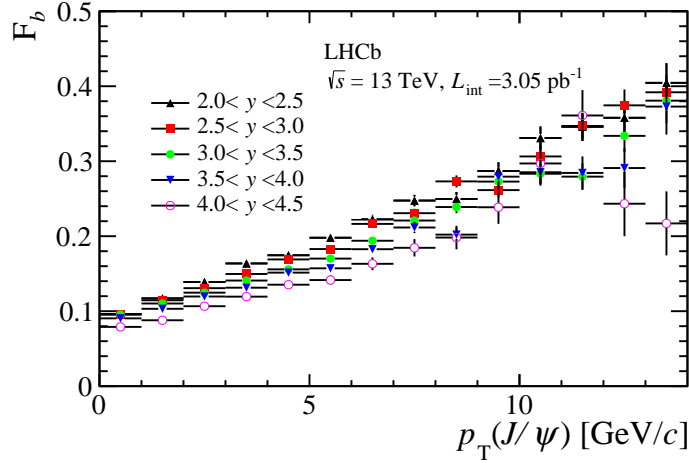


Figure 8.3: Fractions of J/ψ from b in bins of J/ψ p_T and y . Statistical and systematic uncertainties are added in quadrature.

8.2 Extrapolation to 4π

Editor: Matt Needham

The total $b\bar{b}$ production cross-section is calculated using:

$$\begin{aligned} \sigma(pp \rightarrow b\bar{b}X) &= \alpha_{4\pi} \frac{\sigma(J/\psi \text{ from } b, p_T < 14 \text{ GeV}/c, 2.0 < y < 4.5)}{2\mathcal{B}(b \rightarrow J/\psi X)} \\ &= 515 \pm 2 \pm 53 \mu\text{b}, \end{aligned} \quad (8.1)$$

where $\alpha_{4\pi}$ is the extrapolation factor from the measured to full kinematic region and $\mathcal{B}(b \rightarrow J/\psi X) = 1.16 \pm 0.10\%$ is the inclusive $b \rightarrow J/\psi X$ branching fraction. Using the

Table 8.1: The fraction of J/ψ -from- b mesons (in %) in bins of the J/ψ transverse momentum and rapidity. The uncertainty is statistical only. The systematic uncertainty is negligible.

p_T (GeV/ c)	$2 < y < 2.5$	$2.5 < y < 3$	$3 < y < 3.5$	$3.5 < y < 4$	$4 < y < 4.5$
0 – 1	9.6 ± 0.4	9.6 ± 0.3	9.6 ± 0.3	9.0 ± 0.3	7.9 ± 0.5
1 – 2	11.7 ± 0.3	11.5 ± 0.2	11.0 ± 0.2	10.3 ± 0.2	8.8 ± 0.3
2 – 3	13.9 ± 0.3	13.1 ± 0.2	12.5 ± 0.2	12.0 ± 0.2	10.7 ± 0.3
3 – 4	16.4 ± 0.3	15.0 ± 0.2	14.1 ± 0.2	13.1 ± 0.2	11.9 ± 0.4
4 – 5	17.5 ± 0.4	16.9 ± 0.3	15.6 ± 0.3	15.1 ± 0.3	13.5 ± 0.5
5 – 6	19.8 ± 0.5	18.3 ± 0.3	17.0 ± 0.3	15.7 ± 0.4	14.2 ± 0.6
6 – 7	22.2 ± 0.6	21.6 ± 0.5	19.4 ± 0.5	18.3 ± 0.5	16.3 ± 0.9
7 – 8	24.8 ± 0.8	23.1 ± 0.6	22.1 ± 0.6	21.2 ± 0.7	18.5 ± 1.2
8 – 9	25.0 ± 0.9	27.3 ± 0.8	23.9 ± 0.8	20.2 ± 0.9	19.8 ± 1.6
9 – 10	28.7 ± 1.2	26.1 ± 1.0	27.3 ± 1.1	27.9 ± 1.3	23.9 ± 2.2
10 – 11	33.1 ± 1.5	30.6 ± 1.3	28.3 ± 1.4	28.5 ± 1.8	29.7 ± 2.8
11 – 12	34.6 ± 1.9	34.7 ± 1.6	27.9 ± 1.8	28.4 ± 2.2	36.1 ± 3.4
12 – 13	35.8 ± 2.3	37.4 ± 2.1	33.4 ± 2.2	29.1 ± 2.6	24.3 ± 4.3
13 – 14	40.4 ± 2.6	39.2 ± 2.4	38.1 ± 3.0	37.3 ± 3.7	21.7 ± 4.3

LHCb tuning of Pythia 8 [61], $\alpha_{4\pi}$ is found to be 5.1^3 , giving $\sigma(pp \rightarrow b\bar{b}X) = 515 \pm 2 \pm 53 \mu\text{b}$ where the first uncertainty is statistical and the second systematic including the uncertainty on $\mathcal{B}(b \rightarrow J/\psi X)$. No uncertainty on $\alpha_{4\pi}$ is included in this estimate. The NLO based calculations in Ref. [62] give $\alpha_{4\pi} = 5.0$.

8.3 Comparison with RUNI results

To make a comparison with RUN-I analyses, J/ψ cross section measurements in pp collisions at center-of-energy of 2.76 TeV [32], 7 TeV [39] and 8 TeV [38], careful studies have been performed to evaluate the correlations of various sources of systematic uncertainties between this analysis and RUN-I analyses, and decouple the systematic uncertainties in RUN-I analyses into various components since only combined numbers are given in the published results. Fortunately, most of the systematic uncertainties are common among these analyses. A ratio cross section measurement is also made between the results at 13 TeV and 8 TeV to reduce the correlated systematic uncertainties. The correlations are evaluated this way (in the following all analyses means all J/ψ cross section measurements at LHCb including this one):

- Inter bin cross feed, which comes from different detector resolution in simulation and data. Since for analyses with different centre-of-mass energy, similar reconstructions are used in simulation and data, respectively, we expect a similar effect coming from this source. As a result, this kind of systematic uncertainty is totally correlated between all analyses.

³ for $\sqrt{s} = 13$ TeV Pythia 6 gives $\alpha_{4\pi} = 5.22$, FONLL gives $\alpha_{4\pi} = 5.0$
for $\sqrt{s} = 8$ TeV Pythia 6 gives $\alpha_{4\pi} = 5.4$, FONLL gives $\alpha_{4\pi} = 5.1$
for $\sqrt{s} = 7$ TeV Pythia 6 gives $\alpha_{4\pi} = 5.9$, FONLL gives $\alpha_{4\pi} = 5.2$

- 656 • Signal mass shape. In RUN-I analysis, one CB function is used to describe the signal
657 mass shape while in this analysis, two CB functions are used to reduce the systematic
658 uncertainty. This systematic uncertainty is correlated between 13 TeV analysis and
659 RUN-I analysis, however since different models are used to fit the invariant mass,
660 the correlation is not 100%. However since it is difficult to precisely estimate the
661 correlation, we assume the correlation is 50%, while the correlation between different
662 RUN-I analysis is 100%.
- 663 • Radiative tail. All analyses used similar models to describe radiative J/ψ decays, so
664 this effect totally cancels (100% correlated) between different analysis.
- 665 • MuonID The systematic uncertainty of MuonID comes from two sources, the first
666 class is the uncertainty of binning scheme, track multiplicity reweighting, the second
667 source is the limited knowledge of muonID efficiency in data, which is given by
668 the limited sample size of the MuonID calibration data. The first class is totally
669 correlated among different analyses, while the second is uncorrelated. Since the
670 second is dominating, for a simple calculation (and no separate numbers were
671 provided in all RUN-I analyses), we assume MuonID systematic uncertainty is totally
672 uncorrelated.
- 673 • Tracking. The same discussion for MuonID systematic uncertainty applies also to
674 the tracking systematic uncertainty, except that for the tracking, the systematic
675 uncertainty due to limited statistical uncertainty is much smaller (of similar size)
676 compared to the one due to event activities and detector material for 8 TeV analysis
677 (13 TeV analysis). So for simplicity, instead of decoupling the correlated and
678 uncorrelated tracking systematic uncertainty, we assume the total tracking systematic
679 uncertainty is 50% correlated.
- 680 • Vertexing, which is due to different distribution of J/ψ vertex fit quality in simulation
681 and data. We checked that the RUN-I simulation and this analysis have a similar
682 distribution, and for data it is also expected to be similar. So this effect totally
683 cancels.
- 684 • Trigger efficiency. This systematic uncertainty is complicated. In RUN-I 8 TeV
685 analysis, a value of 4% is quoted for all kinematic bins, which comes from comparison
686 of trigger efficiency in data and simulation using the TisTos method and comes
687 from the limited statistics. Later LHCb analysis using similar triggers show that the
688 trigger in simulation and data agrees within precision of 1-2%. For RUN-I 7 TeV
689 analysis, TisTos method is performed bin by bin, resulting in systematic value of
690 a few percent, in average 3%. The trigger systematic uncertainties are correlated
691 between different analyses, and the remaining uncorrelated systematic uncertainty is
692 estimated to be 1.5% between 8 and 13 TeV, which is about half of the total trigger
693 systematic uncertainty. Due to large variations of trigger systematic among different
694 analyses, to be conservative and simple, we assume the correlations are 50% between
695 measurements at all energies.

- 696 • Branching fraction. All RUN-I analysis used a value of $(5.93 \pm 0.06) \times 10^2$, while
697 in 13 TeV analysis an updated value of $(5.961 \pm 0.033) \times 10^2$ is used. To make all
698 numbers consistent for this external number, we update all RunI analysis with new
699 branching fraction value, and the new corresponding uncertainty. With this update,
700 the correlation between the two numbers 100.%, and the systematic uncertainty
701 totally cancels.
702 is $1/\sqrt{2}$.
- 703 • p_T - y -spectrum. The numbers are evaluated independent using different MC samples
704 for different analyses. There should be some correlations between different analyses,
705 since the same MC generator is used for different samples. But the consistency of
706 the kinematics between simulation and data might be different for the samples used
707 for different analyses, so for a conservative estimation, we assume the correlation is
708 zero. This systematic uncertainty is also bin dependent, making it reduced when
709 summing over kinematic bins.
- 710 • MC statistics, which is totally uncorrelated
- 711 • Global event cuts (GEC), which are present in the 8 TeV analysis, but are negligible
712 small.
- 713 • Luminosity, the correlation of luminosity uncertainty between 8 TeV and 7 TeV has
714 been estimated using a statistical [\[method\]](#), in which for each source of systematic
715 uncertainty contributing to the luminosity, a random value is assigned uniformly
716 distribution in the range $0-1$, $0-0.5$ or $0.5-1$, resulting the total correlation around
717 50% (0.55 ± 0.06). For different RUN-I analysis, we assume same correlations, while
718 a smaller value is expected between 13 TeV analysis and 8 TeV analysis because in
719 the 13 TeV analysis, only BGI method is used to determine the luminosity. Before a
720 detailed calculation is available, we take the number 50% as the correlation between
721 13 and 8 TeV luminosity.
- 722 • t_z fit, which only affects the J/ψ from b cross section. There are some correlations
723 between the different analyses, since they use similar methods to estimate the
724 uncertainties and the total reconstruction are not fully different. Again it is difficult
725 to estimate the exact correlation, and the estimated systematic uncertainties have
726 large contributions from statistical fluctuations since the numbers are determined
727 by comparing the nominal fit and alternative fit in each kinematic bin with limited
728 statistics. For a conservative assumption in the ratio measurement, its correlation is
729 assumed to be fully correlated.
- 730 • Branching fraction of $b\bar{b} \rightarrow J/\psi X$, which is correlated among all analyses and only
731 affects the extrapolated $pp \rightarrow b\bar{b}X$ cross section.

732 A more detailed discussion of the systematic uncertainty is given [here](#). Adding possible
733 J/ψ polarization is even more complex, since in the updated 7 TeV analysis the efficiency

is corrected with inputs of the polarization measurement at 7 TeV [39]. On the other hand, other analyses use zero polarization assumption and neglects the polarization effect. We don't intend to remake the RUN-I analyses, synchronize the polarization, instead, we use the same assumptions as the published paper [32, 38, 39], and assume it is totally uncorrelated.

In the cross-section ratios, many of these systematic uncertainties cancel because of their correlations between the two measurements. In Table 8.2, the remaining systematic uncertainties of the cross-section ratio are summarized.

Table 8.2: Summary of systematic uncertainties on the ratios of the cross-section in pp collisions at 13 TeV over that at 8 TeV.

Quantity	Systematic uncertainty
Luminosity	4.6%
Trigger	1.5%
Muon ID	2.2%
Tracking	1%
Signal shape	2%
p_T - y -spectrum, MC stat. (t_z fits)	1 -8 %

In Figs. 8.4, 8.6, and 8.5, 8.7 the ratio cross section between 13 TeV and 8 TeV measurements are given for prompt J/ψ and J/ψ -from- b , taking into account the correlations of various systematic uncertainties as discussed above. The numbers are also given in Tables 8.3 and 8.4, Tables 8.5 and 8.6 respectively. For comparison, in Fig. 8.8 the differential cross-section as a function of p_T integrated over y is shown with all uncertainties added together, compared to measurements with pp collisions at 8 TeV. Also in Fig. 8.9, the differential cross-section as a function of y integrated over p_T is shown for all uncertainties, compared to measurements with pp collisions at 8 TeV. The differential cross section integrated over p_T (y) is given in Table 8.8 (Table 8.7) for prompt J/ψ and J/ψ from b .

Another issue which should be noted is that, when comparing results at different center-of-energies, the correlations may be different. For example, the correlation between signal mass shape is 100% between 7 TeV and 8 TeV analysis, while it is only assumed to be 50% between 8 TeV and 13 TeV analysis. For this case, we split the uncertainty into two parts, correlated ($\sqrt{\rho}\sigma$) and uncorrelated part ($\sqrt{1-\rho}\sigma$), taking the largest correlation among all possible pair-wise cases: 7 TeV versus 8 TeV, 8 TeV versus 13 TeV etc. So for 8 TeV analysis, the correlation for the signal mass shape systematic is 100%, and it is 50% for 13 TeV analysis. This scenario also applies to the luminosity systematic uncertainty, for which the correlation between 7 TeV and 8 TeV is 0.55 ± 0.06 , and it is smaller between 8 TeV and 13 TeV. But this procedure (to choose the largest value among all pair-wise correlations) is only adopted when we compare different measurements for example the integrated prompt J/ψ cross section as a function pp collision energy as shown in Figs. 8.10 and 8.11, but not for the case of measuring ratio cross section between 8

Table 8.3: The ratio of cross-sections between measurements at 13 TeV and 8 TeV in different bins of p_T and y for prompt J/ψ mesons.

p_T (GeV/c)	$2 < y < 2.5$	$2.5 < y < 3$	$3 < y < 3.5$	$3.5 < y < 4$	$4 < y < 4.5$	$2 < y < 4.5$
0 – 1	1.46 ± 0.12	1.23 ± 0.08	1.19 ± 0.07	1.21 ± 0.07	1.25 ± 0.08	1.27 ± 0.08
1 – 2	1.43 ± 0.09	1.28 ± 0.08	1.24 ± 0.07	1.24 ± 0.08	1.33 ± 0.08	1.31 ± 0.08
2 – 3	1.51 ± 0.10	1.39 ± 0.09	1.33 ± 0.08	1.34 ± 0.08	1.35 ± 0.08	1.39 ± 0.08
3 – 4	1.61 ± 0.11	1.44 ± 0.09	1.43 ± 0.08	1.43 ± 0.08	1.50 ± 0.09	1.49 ± 0.09
4 – 5	1.75 ± 0.14	1.52 ± 0.09	1.47 ± 0.09	1.51 ± 0.09	1.58 ± 0.10	1.58 ± 0.09
5 – 6	1.81 ± 0.11	1.62 ± 0.10	1.58 ± 0.10	1.62 ± 0.10	1.76 ± 0.12	1.68 ± 0.10
6 – 7	1.88 ± 0.13	1.63 ± 0.11	1.63 ± 0.10	1.63 ± 0.10	1.81 ± 0.13	1.72 ± 0.10
7 – 8	1.92 ± 0.14	1.65 ± 0.11	1.68 ± 0.11	1.73 ± 0.12	1.88 ± 0.15	1.77 ± 0.11
8 – 9	1.94 ± 0.16	1.68 ± 0.11	1.77 ± 0.13	1.82 ± 0.13	2.07 ± 0.19	1.83 ± 0.11
9 – 10	2.14 ± 0.17	1.85 ± 0.13	1.82 ± 0.15	1.83 ± 0.15	1.98 ± 0.20	1.94 ± 0.12
10 – 11	2.11 ± 0.18	1.78 ± 0.14	1.91 ± 0.15	1.86 ± 0.17	2.19 ± 0.28	1.95 ± 0.13
11 – 12	2.11 ± 0.19	1.75 ± 0.16	2.20 ± 0.18	1.77 ± 0.18	2.16 ± 0.30	1.98 ± 0.13
12 – 13	2.19 ± 0.22	1.75 ± 0.16	2.02 ± 0.20	2.00 ± 0.22	2.59 ± 0.39	2.04 ± 0.14
13 – 14	2.20 ± 0.28	1.89 ± 0.20	1.85 ± 0.22	1.66 ± 0.22	4.65 ± 0.93	2.07 ± 0.16

Table 8.4: The ratio of cross-sections between measurements at 13 TeV and 8 TeV in different bins of y for prompt J/ψ mesons.

$2 < y < 2.5$	$2.5 < y < 3$	$3 < y < 3.5$	$3.5 < y < 4$	$4 < y < 4.5$
1.55 ± 0.09	1.38 ± 0.08	1.33 ± 0.08	1.34 ± 0.08	1.39 ± 0.08

Table 8.5: The ratio of cross-sections between measurements at 13 TeV and 8 TeV in different bins of p_T and y for J/ψ -from- b mesons.

p_T (GeV/c)	$2 < y < 2.5$	$2.5 < y < 3$	$3 < y < 3.5$	$3.5 < y < 4$	$4 < y < 4.5$	$2 < y < 4.5$
0 – 1	1.58 ± 0.25	1.43 ± 0.16	1.51 ± 0.19	1.80 ± 0.13	2.23 ± 0.23	1.63 ± 0.13
1 – 2	1.69 ± 0.12	1.55 ± 0.10	1.55 ± 0.10	1.74 ± 0.13	1.92 ± 0.16	1.66 ± 0.10
2 – 3	1.85 ± 0.13	1.65 ± 0.11	1.69 ± 0.11	1.86 ± 0.12	2.08 ± 0.15	1.79 ± 0.11
3 – 4	2.04 ± 0.15	1.75 ± 0.11	1.76 ± 0.11	1.87 ± 0.12	2.29 ± 0.17	1.90 ± 0.11
4 – 5	2.14 ± 0.18	1.86 ± 0.12	1.82 ± 0.12	2.03 ± 0.13	2.40 ± 0.20	2.00 ± 0.12
5 – 6	2.24 ± 0.16	1.88 ± 0.13	1.89 ± 0.13	2.15 ± 0.15	2.32 ± 0.21	2.06 ± 0.13
6 – 7	2.35 ± 0.18	2.05 ± 0.15	2.08 ± 0.14	2.22 ± 0.16	2.70 ± 0.26	2.22 ± 0.14
7 – 8	2.32 ± 0.19	2.04 ± 0.15	2.17 ± 0.16	2.40 ± 0.19	2.77 ± 0.31	2.25 ± 0.14
8 – 9	2.23 ± 0.21	2.15 ± 0.17	2.22 ± 0.19	2.21 ± 0.20	2.70 ± 0.36	2.23 ± 0.15
9 – 10	2.44 ± 0.22	2.05 ± 0.17	2.27 ± 0.21	3.07 ± 0.32	3.83 ± 0.71	2.44 ± 0.17
10 – 11	2.73 ± 0.27	2.19 ± 0.20	2.38 ± 0.23	3.29 ± 0.41	4.37 ± 0.79	2.64 ± 0.19
11 – 12	2.60 ± 0.28	2.40 ± 0.26	2.48 ± 0.28	2.48 ± 0.35	6.77 ± 1.47	2.67 ± 0.20
12 – 13	2.51 ± 0.31	2.10 ± 0.23	2.47 ± 0.31	2.51 ± 0.39	3.19 ± 0.78	2.40 ± 0.19
13 – 14	2.81 ± 0.39	2.58 ± 0.32	2.85 ± 0.43	3.50 ± 0.65	3.62 ± 1.11	2.84 ± 0.25

Table 8.6: The ratio of cross-sections between measurements at 13 TeV and 8 TeV in different bins of y for J/ψ -from- b mesons.

$2 < y < 2.5$	$2.5 < y < 3$	$3 < y < 3.5$	$3.5 < y < 4$	$4 < y < 4.5$
1.93 ± 0.12	1.70 ± 0.10	1.71 ± 0.10	1.90 ± 0.11	2.18 ± 0.14

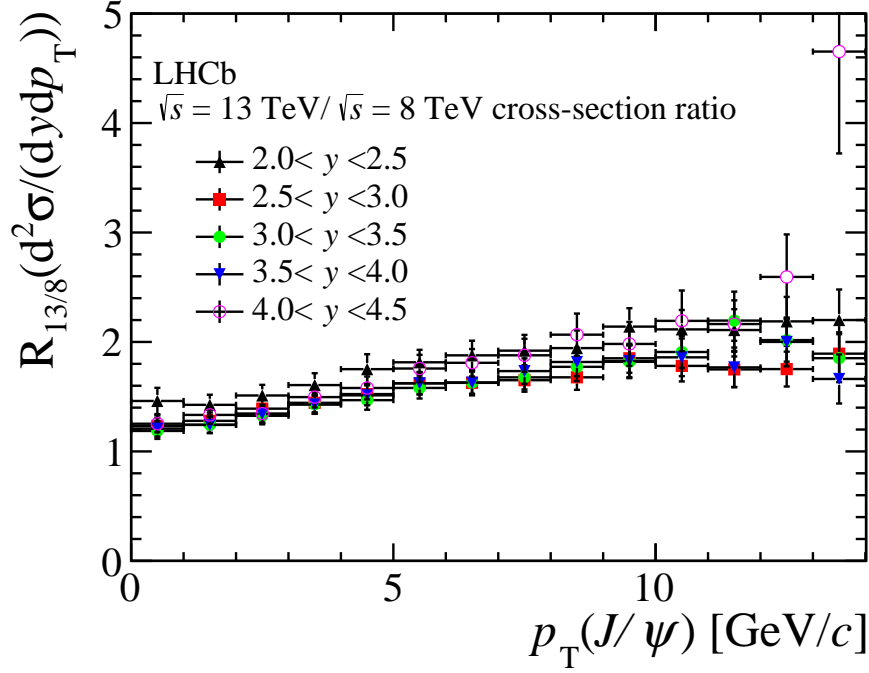


Figure 8.4: Ratio of differential cross sections between 13 TeV and 8 TeV measurement as a function of p_T in bins of y for prompt J/ψ .

and 13 TeV.

In Fig. 8.10, the J/ψ total cross-section in the LHCb acceptance as a function of pp center-of-mass energy is shown for prompt and J/ψ from b . In Fig. 8.11, the extrapolated $pp \rightarrow b\bar{b}$ cross sections in the full acceptance are compared in different pp collision energies. The uncertainties are split into correlated and uncorrelated parts, according to the discussions above. In Table 8.9, the cross sections as a function of the pp center-of-mass energy is given.

8.4 Comparison with theoretical models

Editor: Giulia Manca

The result is compared with the following theoretical models:

- NRQCD calculations [63] are compared for prompt J/ψ cross-section as a function of transverse momentum integrated over y in the range $2 < y < 4.5$ in the left

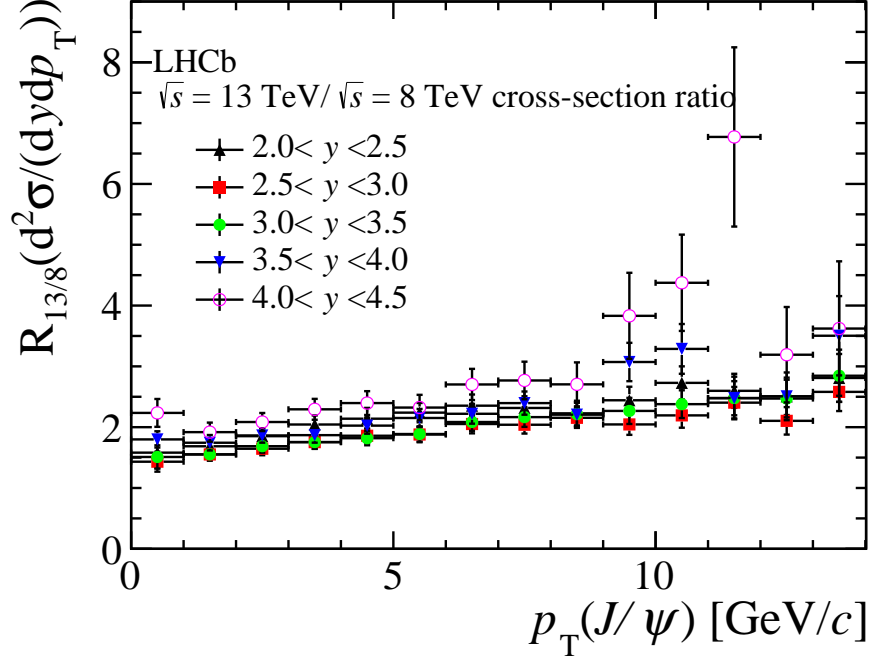


Figure 8.5: Ratio of differential cross sections between 13 TeV and 8 TeV measurement as a function of p_T in bins of y for J/ψ from b.

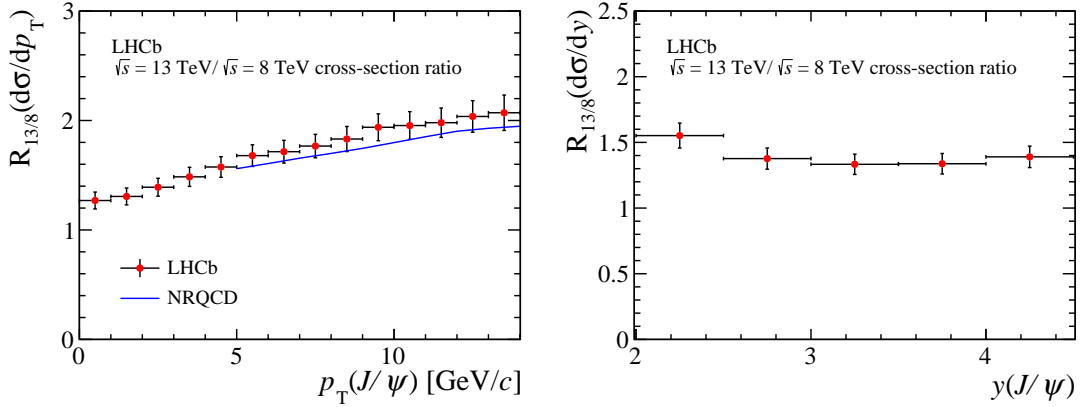


Figure 8.6: Ratio of differential cross sections between 13 TeV and 8 TeV measurement as a function of (left) p_T integrated over y , (right) y integrated over p_T for prompt J/ψ . Theoretical calculations of NRQCD [63] are compared to prompt J/ψ mesons on the left side.

777 plot of Fig. 8.12. In the NRQCD calculations, only uncertainties associated with
 778 LDMEs are considered since it is the dominating uncertainty for absolute production
 779 cross-section predictions. Good agreement is seen between NRQCD calculation and
 780 the measurement.

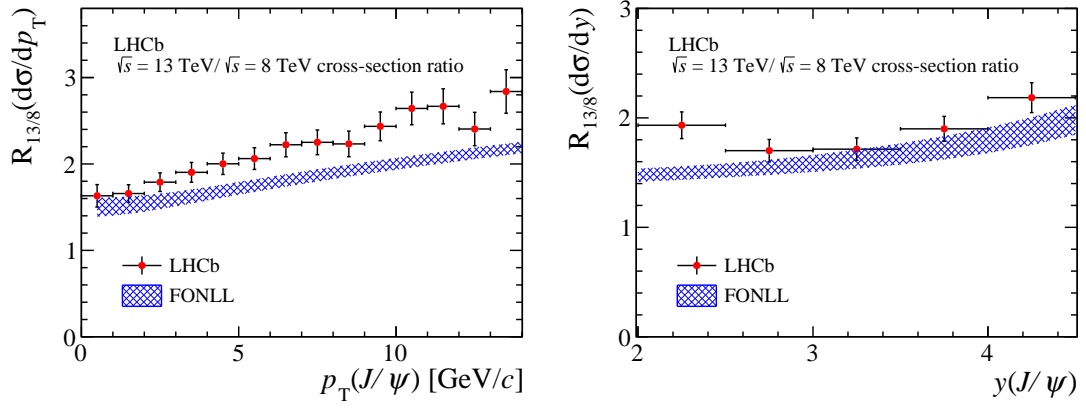


Figure 8.7: Ratio of differential cross sections between 13 TeV and 8 TeV measurement as a function of (left) p_T integrated over y , (right) y integrated over p_T for J/ψ from b . Theoretical FONLL calculations [64] are compared to the measured J/ψ -from- b ratio.

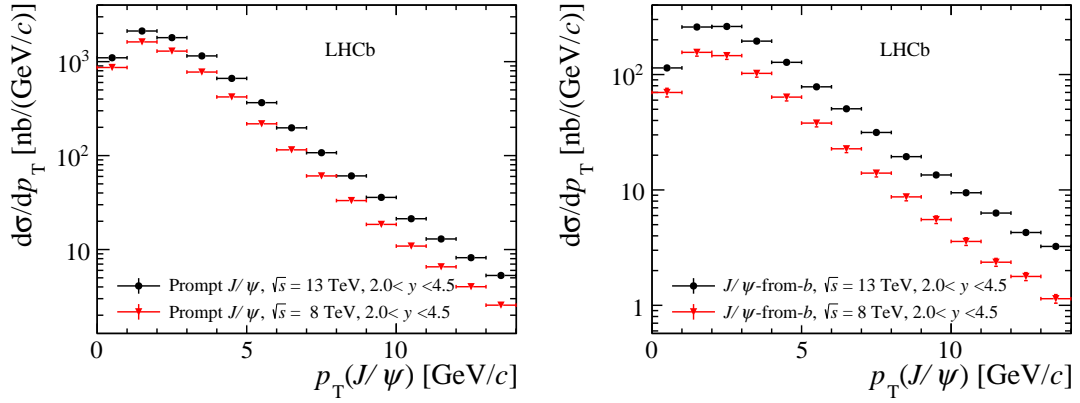


Figure 8.8: Differential cross-section as a function of p_T integrated over y for (left) prompt J/ψ and (right) J/ψ from b .

- FONLL calculations [40] are compared for J/ψ from b cross-section as a function of transverse momentum integrated over y in the range $2 < y < 4.5$ in the right plot of Fig. 8.12. The FONLL calculation includes the uncertainties due to b -quark mass and renormalisation-factorisation scales for the prediction of absolute production cross-section. The calculation is consistent with our measurement.
- The ratio of the cross-sections as a function of y integrated over p_T in the range $0 < p_T < 14 \text{ GeV}/c$ are compared with FONLL calculations [64] for J/ψ -from b , as shown in right of Fig. 8.7. The ratio of the cross-sections as a function of p_T integrated over y in the range $2 < y < 4.5$ is also compared with NRQCD calculations [63] for prompt J/ψ mesons, and predictions by FONLL [64] for J/ψ -from b , shown in left of Fig. 8.6 and Fig. 8.7 respectively. The uncertainty of the NRQCD prediction,

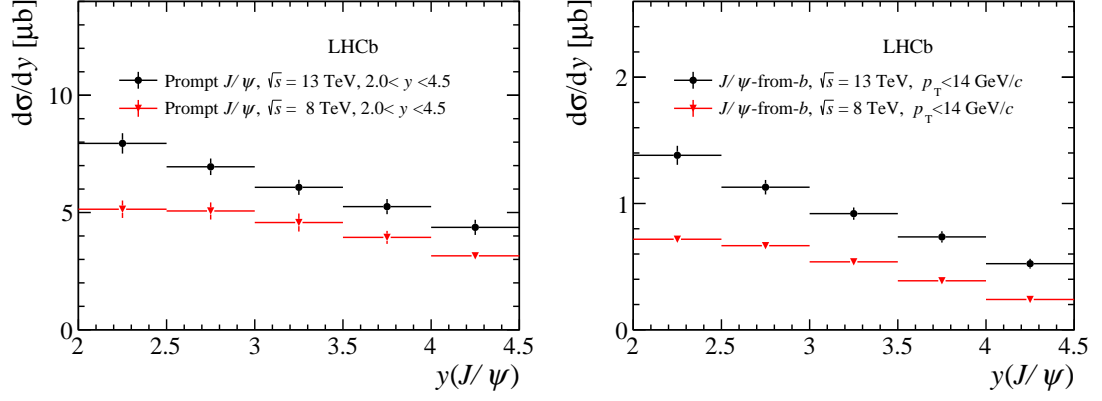


Figure 8.9: Differential cross-section as a function of y integrated over p_T for (left) prompt J/ψ and (right) J/ψ from b .

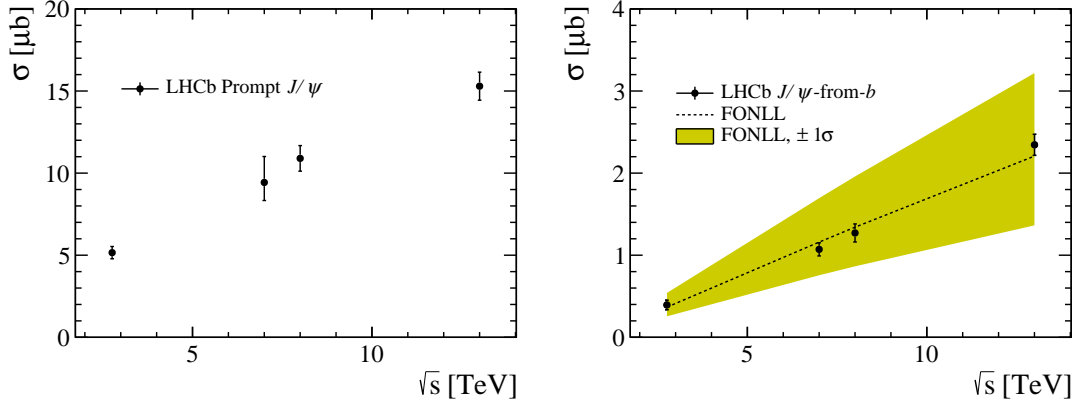


Figure 8.10: The J/ψ production cross-section for (left) prompt J/ψ and (right) J/ψ from b as a function of pp collision energy in LHCb acceptance.

792 considering only those from LDMEs, almost cancels in the cross-section ratio between
 793 13 TeV and 8 TeV measurements, so no uncertainties are given for the calculations
 794 in the left plot of Fig. 8.6. Besides those due to b -quark mass and scales, the
 795 FONLL calculation for the cross-section ratio also takes into account the gluon PDF
 796 uncertainty. The NRQCD calculation is in agreement with our data for prompt J/ψ
 797 production, while FONLL slightly undershoots our measurements.

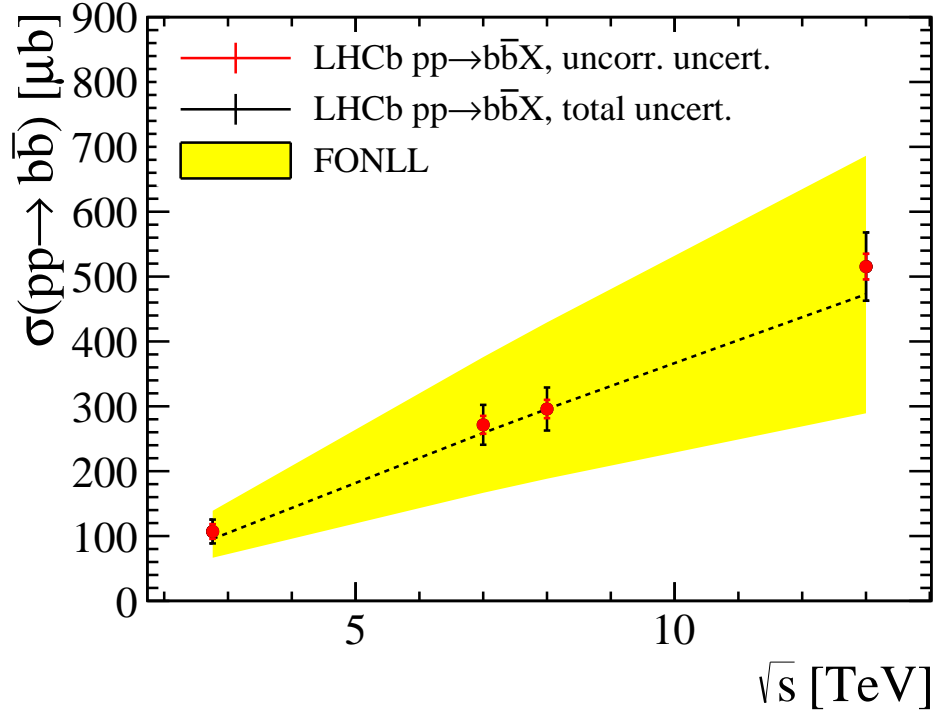


Figure 8.11: The production cross section of $pp \rightarrow b\bar{b}$ as a function of pp collision energy in full acceptance, extrapolated from the cross section of J/ψ from b .

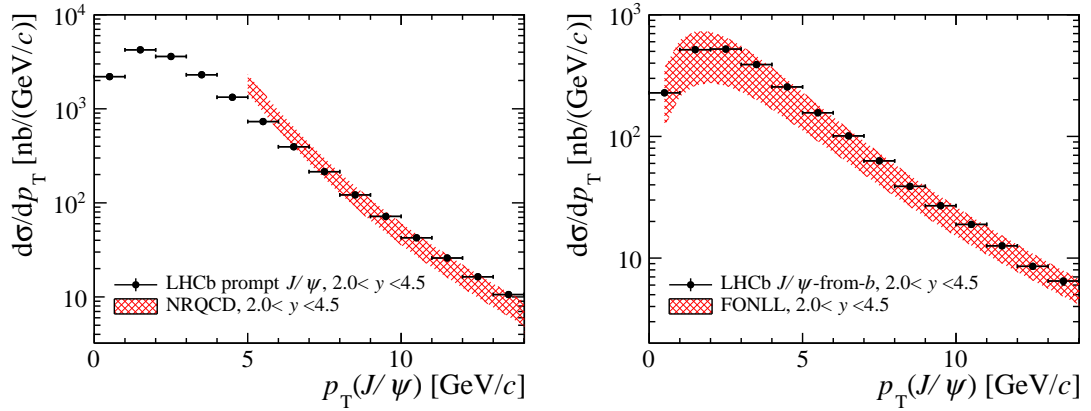


Figure 8.12: Differential cross-section as a function of p_T integrated over y in the range $2 < y < 4.5$, (left) compared with NRQCD for prompt J/ψ and (right) compared with FONLL for J/ψ from b .

Table 8.7: Differential cross-sections $d\sigma/dp_T$ (in nb) for prompt J/ψ and J/ψ -from- b mesons, integrated over y . The first uncertainty is statistical and the second (third) is systematic, correlated (uncorrelated) amongst bins.

p_T (GeV/c)	Prompt J/ψ	J/ψ -from- b
0 – 1	$2198 \pm 11 \pm 17 \pm 127$	$228.3 \pm 4.1 \pm 1.8 \pm 13.1$
1 – 2	$4237 \pm 15 \pm 13 \pm 245$	$516.4 \pm 5.1 \pm 1.7 \pm 29.5$
2 – 3	$3600 \pm 12 \pm 13 \pm 202$	$522.1 \pm 4.6 \pm 2.0 \pm 29.1$
3 – 4	$2301 \pm 9 \pm 9 \pm 125$	$389.7 \pm 3.7 \pm 1.7 \pm 21.0$
4 – 5	$1326 \pm 6 \pm 6 \pm 69$	$255.2 \pm 2.7 \pm 1.3 \pm 13.4$
5 – 6	$731.8 \pm 4.0 \pm 3.1 \pm 37.9$	$156.6 \pm 1.9 \pm 0.7 \pm 8.1$
6 – 7	$394.9 \pm 2.7 \pm 3.8 \pm 20.3$	$101.0 \pm 1.4 \pm 1.1 \pm 5.2$
7 – 8	$214.6 \pm 1.9 \pm 2.1 \pm 10.9$	$63.0 \pm 1.1 \pm 0.7 \pm 3.2$
8 – 9	$121.6 \pm 1.4 \pm 0.9 \pm 6.2$	$38.9 \pm 0.8 \pm 0.3 \pm 2.0$
9 – 10	$71.8 \pm 1.0 \pm 0.7 \pm 3.6$	$27.0 \pm 0.7 \pm 0.3 \pm 1.4$
10 – 11	$42.6 \pm 0.8 \pm 0.4 \pm 2.2$	$18.9 \pm 0.6 \pm 0.2 \pm 1.0$
11 – 12	$25.9 \pm 0.6 \pm 0.3 \pm 1.3$	$12.6 \pm 0.4 \pm 0.1 \pm 0.6$
12 – 13	$16.4 \pm 0.5 \pm 0.2 \pm 0.8$	$8.6 \pm 0.3 \pm 0.1 \pm 0.4$
13 – 14	$10.6 \pm 0.4 \pm 0.2 \pm 0.5$	$6.5 \pm 0.3 \pm 0.1 \pm 0.3$

Table 8.8: Differential cross-sections $d\sigma/dy$ (in nb) for prompt J/ψ and J/ψ -from- b mesons, integrated over p_T . The first uncertainty is statistical and the second (third) is systematic, correlated (uncorrelated) amongst bins.

y	Prompt J/ψ	J/ψ -from- b
2.0 – 2.5	$7947 \pm 36 \pm 44 \pm 430$	$1381 \pm 13 \pm 6 \pm 73$
2.5 – 3.0	$6949 \pm 20 \pm 20 \pm 351$	$1128 \pm 7 \pm 3 \pm 56$
3.0 – 3.5	$6074 \pm 17 \pm 10 \pm 320$	$919 \pm 6 \pm 1 \pm 48$
3.5 – 4.0	$5251 \pm 16 \pm 9 \pm 322$	$735 \pm 6 \pm 1 \pm 44$
4.0 – 4.5	$4367 \pm 19 \pm 27 \pm 321$	$523 \pm 7 \pm 3 \pm 37$

Table 8.9: Production cross-sections of prompt J/ψ and J/ψ -from- b mesons, integrated over LHCb fiducial region, in pp collisions at various centre-of-mass energies. The first is the total uncorrelated uncertainty, and the second the total correlated uncertainty.

σ_{tot} (μb)	$\sqrt{s} = 2.76 \text{ TeV}$	$\sqrt{s} = 7 \text{ TeV}$	$\sqrt{s} = 8 \text{ TeV}$	$\sqrt{s} = 13 \text{ TeV}$
Prompt J/ψ	$5.2 \pm 0.3 \pm 0.3$	$9.43 \pm 0.47^{+0.72}_{-0.99}$	$10.9 \pm 0.5 \pm 0.6$	$15.3 \pm 0.6 \pm 0.6$
J/ψ -from- b	$0.39 \pm 0.04 \pm 0.04$	$1.07 \pm 0.05 \pm 0.06$	$1.27 \pm 0.06 \pm 0.09$	$2.34 \pm 0.09 \pm 0.09$

9 Conclusion

The J/ψ production in proton-proton collisions at $\sqrt{s} = 13$ TeV is studied with an integrated luminosity of $3.01 \pm 0.12 \text{ pb}^{-1}$, collected by the LHCb detector in 2015. The double differential cross-section, as a function of p_T and y of the J/ψ meson in the range of $0 < p_T < 14 \text{ GeV}/c$ and $2 < y < 4.5$, is determined for prompt J/ψ and J/ψ from b -hadron decays. Integrating over the kinematic coverage, the cross-sections are obtained as:

$$\begin{aligned}\sigma(\text{prompt } J/\psi) &= 15.30 \pm 0.03 (\text{stat}) \pm 0.86 (\text{syst}) \mu\text{b} \\ \sigma(J/\psi \text{ from } b) &= 2.34 \pm 0.01 (\text{stat}) \pm 0.13 (\text{syst}) \mu\text{b}.\end{aligned}$$

The p_T distribution of J/ψ mesons in 13 TeV pp collisions are harder than the one in 8 TeV for both prompt J/ψ and J/ψ from b . The measured prompt J/ψ production cross-section as a function of transverse momentum is in good agreement with theoretical NRQCD calculations. The cross-section of J/ψ from b agrees with FONLL calculations it also describes the dependence on the centre-of-mass energy of pp collisions well.

A Luminosity determination

The absolute luminosity is measured using pp collisions taken in special physical runs, using direct methods of and beam gas interaction (BGI) described here [65, 66]. This absolute determination of the luminosity is propagated to any data-taking period using a relative normalization method, i.e. the counts of a physical observable is proportional to its cross section σ times the integrated luminosity, $N = \int \mathcal{L} \sigma$. The cross section is calibrated using the measurements of the absolute luminosity during special data taking period. Several observables have been used, and each one corresponds to an effective cross-section. The integrated luminosity for an arbitrary period of data taking is obtained by dividing the accumulated counts by its cross-section for each variable. The integrated luminosity for the data considered in this analysis is calculated to be $3.05 \pm 0.12 \text{ pb}^{-1}$.

B Stripping selection

Editor: Roberta Cardinale

Events containing a dimuon pair are preselected using a loose stripping line dedicated to quarkonia, `DiMuonForXSection`. Candidates are formed from pairs of opposite sign tracks identified as muons originating from a common vertex requiring $\chi^2/\text{ndf} < 25$. Each track is required to have a good quality of the track fit, $\chi^2/\text{ndf} < 3$, a transverse momentum higher than 650 MeV/c and the χ^2 value of the distance of the closest approach below 30. Moreover, the mass of the dimuon pair is required either to be within $\pm 150 \text{ MeV}/c^2$ of the nominal J/ψ or $\psi(2S)$ mass or above $8500 \text{ MeV}/c^2$, since this stripping line will be also used for $\psi(2S)$ and Υ studies. The complete list of stripping requirements is given in Table B.1.

Variable	Value
Track χ^2/ndf	< 3
Doca χ^2	< 30
Muon Identification	isMuon
Muon p_T	$> 650 \text{ MeV}/c$
vertex χ^2/ndf	< 25
Mass cut	$ m(\mu^+\mu^-) - M(\psi) < 150 \text{ MeV}/c^2 \parallel m > 8500 \text{ MeV}/c^2$

Table B.1: Stripping selection criteria

C Parameterization of signal mass shape

The invariant mass distribution of the signal is described by CB function(s), with a tail to account for radiative decay.

Not all parameters of the CB function(s) are free when fitting data, on the other hand, the correlations among them are investigated and parametrized accordingly with toy MC samples. The n parameter is set to be unity motivated by physics. The determination of a as a function of σ is done using the generator level MC sample, in which the invariant mass of dimuons differs from true J/ψ mass due to missing photons. Then the dimuon mass is smeared using a Gaussian distribution with zero mean and a constant sigma, Σ , which emulate the Gaussian detector resolution with a value of Σ . The result invariant mass distribution is fitted with a CB function with $n = 1$, and all other parameters are free. One of the fitted plot is shown in the left plot of Fig. C.1. In general the fitted mean and sigma value will be biased by a small amount ($\approx 2\%$) because the Gaussian core of the CB also takes into account the radiative effect in the corresponding region. So the CB function is only an effective function. By repeating this procedure with different Σ , the relation between the a parameter and fitted σ (resolution) can be determined, as shown in the right plot of Fig. C.1. The parametrization is tested using generated J/ψ events with very different momentum, and no significant difference is observed, which means for

different kinematic bins of J/ψ , the same relation between a and σ can be used, which is $a = 2.066 \pm 0.0085\sigma - 0.00011\sigma^2$, for σ in unit of MeV/c^2 . Note that this equation is only valid for $n = 1$. This parametrization is tested with background events included in this way: A CB function plus exponential is used to fit the invariant mass distribution of the smeared MC truth events mixed with artificially generated background events with mass following exponential distribution. The fitted signal yield is always consistent with the number of MC truth events for background to signal ratio from 0.01 to 10, as shown by Fig. C.2.

For toy MC, a single pure gaussian resolution is used to smear the mass distribution,

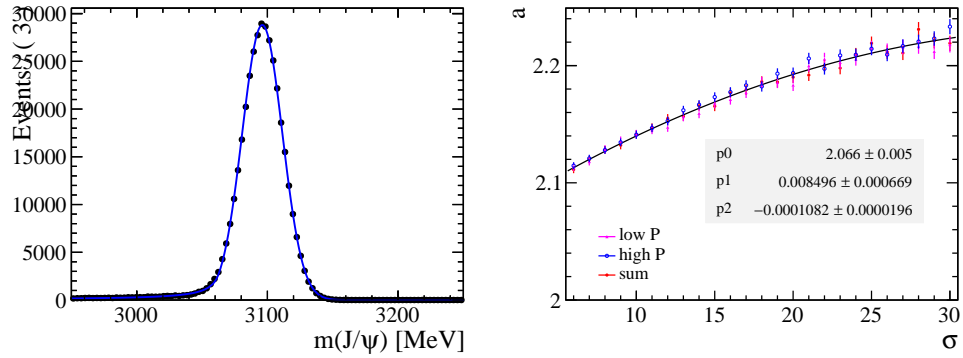


Figure C.1: (Left) The smeared invariant mass distribution of dimuons superimposed with fit with a CB function. (Right) The a parameter as a function of fitted resolution for J/ψ in different momentum range.

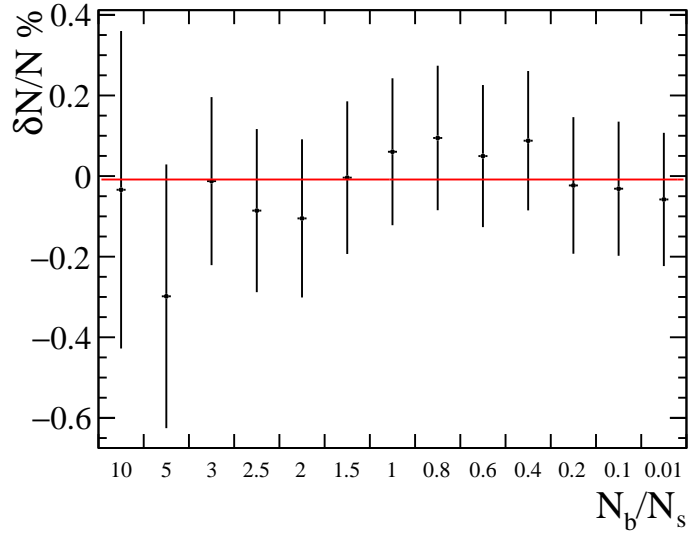


Figure C.2: The relative difference between fitted signal yield and the number of MC truth events for different signal to background level.

858 however for full simulation it is found that one single CB is not enough to fit the signal very
 859 well because the resolution is not merely a single Gaussian. The fit to the combination of
 860 full simulation J/ψ candidates and artificial background using single CB plus an exponential
 861 function shows that that yield is biased by 2.5%. A second CB is included, with the same
 862 parametrization of a as a function of σ and $n = 1$. The result suggest that the fraction of
 863 the CB with narrower width is approximately 0.96, and relation between the two widths
 864 can be parametrized as a linear function, as $\sigma_2 = 25.7 + 1.0\sigma_1$, as can be seen in Fig. C.3.
 865 With two CB functions, and parametrized this way, the fitted yield is only biased by
 866 around 1% as shown in Fig. C.4 for different J/ψ kinematic bins.

867 The Ipatia function is known to fit the invariant mass distribution better since it

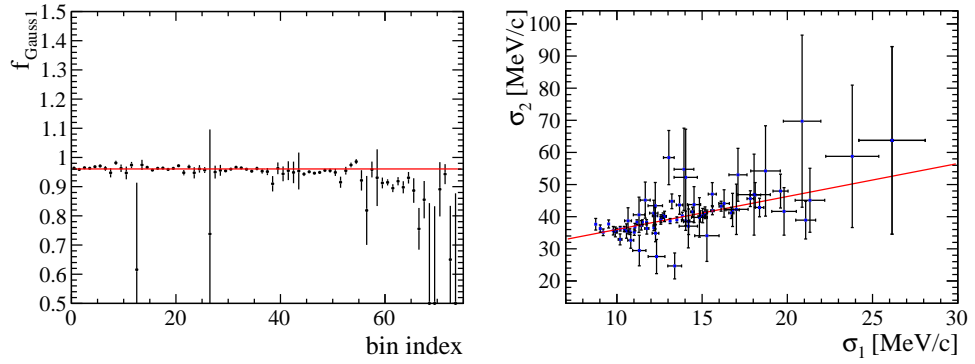


Figure C.3: (Left) The fitted fraction of the CB with narrower width, (Right) the relation between the width of the wider CB function and the one of the narrower CB function.

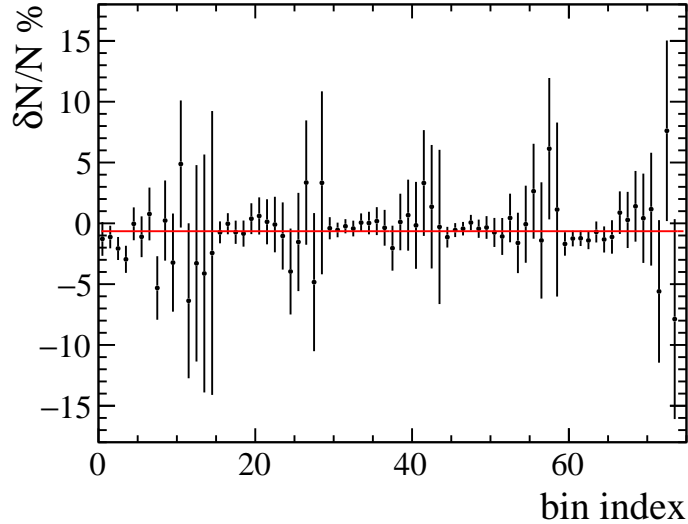


Figure C.4: The relative difference between fitted signal yield and the number of MC truth events in different kinematic bin of J/ψ (and different signal to background level).

868 takes into account event by event uncertainty of invariant mass. For a high statistics bin
 869 $2 < p_T < 3 \text{ GeV}/c$, $3 < y < 3.5$, the invariant mass distribution of full simulation events
 870 matched to MC truth is shown in left plot of Fig. C.5, with the fitted Ipatia function
 871 superimposed. For the signal plus background sample, the fit is given in right plot of
 872 Fig. C.5, and the Ipatia function is found to give unbiased yields, as shown in Fig. C.6
 873 (straight line fit gives $0.1\% \pm 0.1\%$). However due to much more time consuming with
 874 Ipatia fit, we don't use it as the default mass fit model, but it provides an alternative model
 875 for the study of the invariant mass fit systematic uncertainty, as the difference between
 876 nominal two-CB model and Ipatia model. In Fig. C.7, the difference of fitted yields given
 877 by Hypatia and double-CB function, divided by MC truth matched yield, is shown; the
 878 uncertainty is statistical uncertainty corresponding to the invariant mass fit of double-CB
 879 function (similar for Ipatia fit). The difference is consistent with being constant, taking
 880 into account the partially correlated statistical uncertainty. One can take the difference
 881 between Ipatia and double-CB as systematic uncertainty for a high statistics bin as the
 882 systematic uncertainty; alternatively to reduce the statistical uncertainty, one can merge
 883 several (or all) kinematic bins, and study the difference of yields given by fitting with
 884 Ipatia function and the summed yield in each kinematic bin given by double-CB fit.

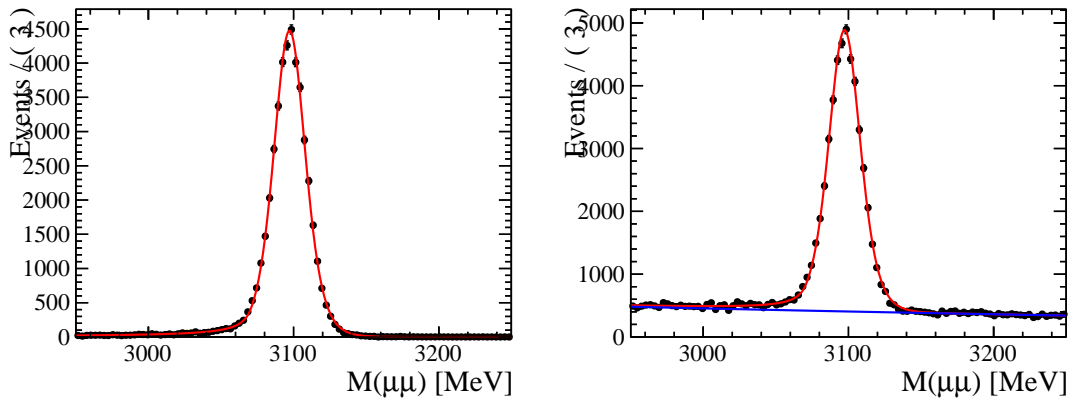


Figure C.5: Ipatia function fitted to (left) truth matched full simulation events, (right) full simulation including backgrounds (background described by exponential function).

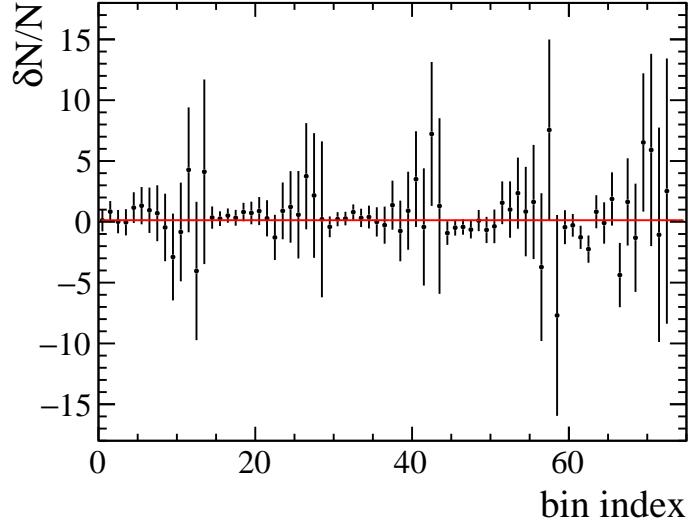


Figure C.6: The relative difference between fitted signal yield and the number of MC truth events in different kinematic bin of J/ψ for the Ipatia fit function.

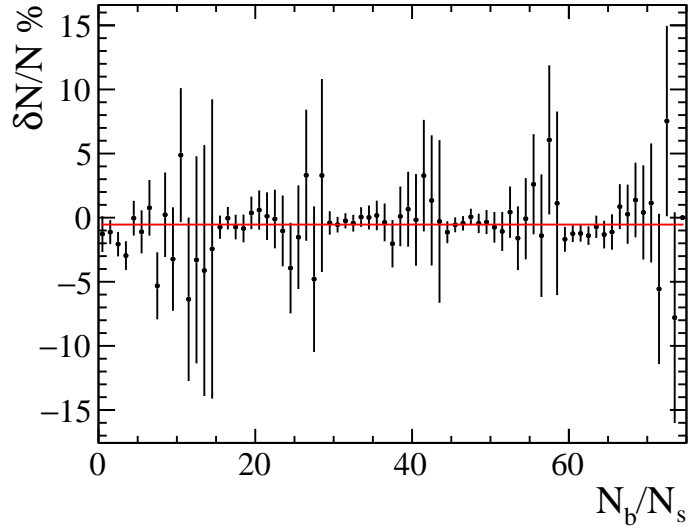


Figure C.7: The difference between fitted signal yields of Ipatia function and double-CB function, divided by truth matched yield.

D Fit results in each kinematic bin tabulated

For each kinematic bin of J/ψ candidates, the fitted value of $\mu_{J/\psi}$ (mean of invariant mass), σ_1 (width of narrower Gaussian), β (fraction of first Gaussian of signal resolution function), F_b (from fit), F'_b (from fit excluding tail component, $F'_b = \frac{F_b}{1-F_t}$), $\mu * 1000$ (bias of t_z distribution), $S_{1,2}$ ($\sigma_{1,2}$ of first/second Gaussian resolution function convolved with the t_z function), τ_b (effective b -hadron lifetime), n_{bkg} , n_p (number of prompt J/ψ), n_b (number of J/ψ -from- b) and n_{tail} (number of events in tail) will be given in tables.

Table D.1: The parameters of the invariant mass and t_z fit, including the fitted yields and shape parameters for different p_T bins in the rapidity bin $2.00 < y < 2.50$.

parameter	p_T (GeV/c)						
	0-1	1-2	2-3	3-4	4-5	5-6	6-7
$\mu_{J/\psi}$	3098.6 ± 0.2	3098.1 ± 0.1	3098.0 ± 0.1	3097.7 ± 0.1	3097.7 ± 0.1	3097.6 ± 0.2	3097.7 ± 0.2
σ_1	11.0 ± 0.2	10.9 ± 0.1	10.7 ± 0.1	11.0 ± 0.1	11.5 ± 0.1	12.1 ± 0.1	12.6 ± 0.2
β	0.047 ± 0.006	0.43 ± 0.07	0.53 ± 0.07	0.12 ± 0.08	0.19 ± 0.06	0.030 ± 0.008	0.21 ± 0.07
F_b	0.091 ± 0.004	0.113 ± 0.003	0.134 ± 0.003	0.155 ± 0.003	0.166 ± 0.004	0.188 ± 0.005	0.208 ± 0.006
F'_b	0.092 ± 0.004	0.113 ± 0.003	0.1340 ± 0.0027	0.1554 ± 0.0033	0.1664 ± 0.0037	0.1882 ± 0.0047	0.2083 ± 0.0057
$\mu * 1000$	-9.9 ± 0.9	-10.9 ± 0.6	-7.7 ± 0.5	-6.3 ± 0.5	-4.3 ± 0.6	-2.7 ± 0.6	-2.1 ± 0.7
S_1	8.1 ± 0.8	1.61 ± 0.07	1.46 ± 0.05	1.9 ± 0.4	1.8 ± 0.2	4.5 ± 0.6	1.8 ± 0.2
S_2	1.19 ± 0.02	0.91 ± 0.04	0.85 ± 0.04	1.06 ± 0.04	1.02 ± 0.03	1.14 ± 0.01	1.01 ± 0.04
τ_b	1.7 ± 0.1	1.56 ± 0.05	1.50 ± 0.03	1.41 ± 0.03	1.47 ± 0.04	1.39 ± 0.04	1.33 ± 0.04
n_{bkg}	47497 ± 250	125880 ± 405	84798 ± 332	36016 ± 220	15743 ± 149	6411 ± 98	2910 ± 68
n_{sig}	11233 ± 161	26321 ± 253	25954 ± 227	18907 ± 177	14397 ± 144	10044 ± 115	6794 ± 92
n_p	10199 ± 158	23338 ± 243	22476 ± 217	15968 ± 169	12001 ± 135	8153 ± 107	5379 ± 83
n_b	1033 ± 50	2984 ± 75	3477 ± 74	2939 ± 66	2396 ± 57	1890 ± 51	1415 ± 43
n_{tail}	69 ± 24	51 ± 27	7 ± 13	10.8 ± 8.1	11.1 ± 7.9	0.0 ± 1.9	15.8 ± 6.2
parameter	7-8	8-9	9-10	10-11	11-12	12-13	13-14
$\mu_{J/\psi}$	3097.2 ± 0.2	3097.5 ± 0.3	3097.1 ± 0.3	3097.5 ± 0.4	3096.9 ± 0.5	3096.9 ± 0.6	3099.0 ± 0.8
σ_1	12.8 ± 0.2	12.7 ± 0.2	13.4 ± 0.3	13.0 ± 0.4	13.1 ± 0.5	13.6 ± 0.6	15.0 ± 0.8
β	0.05 ± 0.02	0.19 ± 0.09	0.2 ± 0.2	0.05 ± 0.02	0.03 ± 0.03	0.7 ± 0.3	0.1 ± 0.1
F_b	0.239 ± 0.007	0.243 ± 0.009	0.27 ± 0.01	0.30 ± 0.01	0.34 ± 0.02	0.33 ± 0.02	0.41 ± 0.03
F'_b	0.2388 ± 0.0074	0.2430 ± 0.0091	0.2736 ± 0.0113	0.301 ± 0.015	0.336 ± 0.018	0.335 ± 0.022	0.407 ± 0.026
$\mu * 1000$	-1.4 ± 0.8	0.0 ± 1.0	-1.7 ± 1.1	-0.6 ± 1.3	0.2 ± 1.5	-1.8 ± 1.9	-3.3 ± 2.4
S_1	3.1 ± 0.5	2.0 ± 0.3	2.1 ± 0.7	4.9 ± 1.0	3.9 ± 1.5	1.5 ± 0.2	2.7 ± 1.8
S_2	1.14 ± 0.03	1.11 ± 0.06	1.1 ± 0.1	1.25 ± 0.04	1.19 ± 0.05	0.9 ± 0.3	1.4 ± 0.1
τ_b	1.37 ± 0.05	1.33 ± 0.06	1.29 ± 0.06	1.24 ± 0.07	1.13 ± 0.07	1.3 ± 0.1	1.4 ± 0.1
n_{bkg}	1387 ± 48	672 ± 34	338 ± 25	223 ± 20	167 ± 17	114 ± 14	61 ± 11
n_{sig}	4449 ± 73	2894 ± 58	1973 ± 47	1328 ± 39	864 ± 31	612 ± 26	436 ± 22
n_p	3387 ± 65	2191 ± 52	1433 ± 41	928 ± 34	573 ± 26	407 ± 22	258 ± 18
n_b	1062 ± 37	703 ± 30	540 ± 26	400 ± 23	290 ± 19	205 ± 16	178 ± 14
n_{tail}	4.9 ± 3.4	2.1 ± 2.1	0.0 ± 1.5	2.9 ± 2.8	0.0 ± 1.0	7.9 ± 4.0	0.0 ± 1.0

Table D.2: The parameters of the invariant mass and t_z fit, including the fitted yields and shape parameters for different p_T bins in the rapidity bin $2.50 < y < 3.00$.

parameter	p_T (GeV/c)						
	0-1	1-2	2-3	3-4	4-5	5-6	6-7
$\mu_{J/\psi}$	3097.5 ± 0.1	3097.20 ± 0.07	3097.30 ± 0.07	3097.10 ± 0.08	3097.10 ± 0.09	3096.9 ± 0.1	3097.0 ± 0.1
σ_1	10.6 ± 0.1	10.83 ± 0.07	11.12 ± 0.07	11.47 ± 0.07	11.75 ± 0.08	12.20 ± 0.10	12.5 ± 0.1
β	0.31 ± 0.04	0.47 ± 0.04	0.37 ± 0.05	0.32 ± 0.05	0.42 ± 0.09	0.22 ± 0.05	0.3 ± 0.1
F_b	0.092 ± 0.003	0.112 ± 0.002	0.127 ± 0.002	0.145 ± 0.002	0.164 ± 0.003	0.181 ± 0.003	0.210 ± 0.004
F_b'	0.093 ± 0.003	0.1121 ± 0.0017	0.1270 ± 0.0018	0.1447 ± 0.0021	0.1638 ± 0.0026	0.2 ± 0.0	0.2100 ± 0.0044
$\mu * 1000$	-8.8 ± 0.5	-8.4 ± 0.4	-7.1 ± 0.3	-4.5 ± 0.3	-3.9 ± 0.3	-3.5 ± 0.4	-2.2 ± 0.4
S_1	1.88 ± 0.08	1.57 ± 0.04	1.59 ± 0.06	1.62 ± 0.07	1.48 ± 0.07	1.8 ± 0.1	1.6 ± 0.2
S_2	0.96 ± 0.03	0.88 ± 0.03	0.93 ± 0.03	0.95 ± 0.02	0.93 ± 0.04	1.01 ± 0.03	1.00 ± 0.06
τ_b	1.35 ± 0.06	1.58 ± 0.03	1.54 ± 0.02	1.50 ± 0.02	1.37 ± 0.02	1.37 ± 0.03	1.34 ± 0.03
n_{bkg}	163118 ± 458	306734 ± 630	186690 ± 496	76476 ± 322	24637 ± 187	7952 ± 111	3087 ± 71
n_{sig}	31512 ± 280	65422 ± 395	59107 ± 344	41930 ± 262	28482 ± 197	18125 ± 150	11084 ± 114
n_p	28581 ± 270	58089 ± 378	51603 ± 328	35868 ± 248	23817 ± 184	14850 ± 138	8756 ± 104
n_b	2930 ± 84	7332 ± 117	7504 ± 109	6065 ± 93	4665 ± 79	3275 ± 64	2328 ± 54
n_{tail}	444 ± 53	137 ± 45	16 ± 22	8 ± 15	13 ± 10	0.0 ± 1.7	14.1 ± 6.8
parameter	7-8	8-9	9-10	10-11	11-12	12-13	13-14
$\mu_{J/\psi}$	3097.0 ± 0.2	3096.6 ± 0.2	3097.0 ± 0.3	3096.3 ± 0.4	3097.2 ± 0.5	3094.8 ± 0.7	3097.0 ± 0.7
σ_1	12.6 ± 0.2	12.9 ± 0.2	13.2 ± 0.3	13.8 ± 0.3	13.2 ± 0.4	15.0 ± 0.6	14.3 ± 0.6
β	0.21 ± 0.08	0.27 ± 0.08	0.3 ± 0.1	0.6 ± 0.2	0.15 ± 0.10	0.4 ± 0.1	0.2 ± 0.2
F_b	0.223 ± 0.006	0.259 ± 0.008	0.258 ± 0.010	0.30 ± 0.01	0.34 ± 0.02	0.36 ± 0.02	0.38 ± 0.02
F_b'	0.2236 ± 0.0058	0.2592 ± 0.0078	0.2584 ± 0.0096	0.299 ± 0.013	0.3387 ± 0.0161	0.363 ± 0.021	0.385 ± 0.024
$\mu * 1000$	-2.1 ± 0.6	-1.4 ± 0.7	-0.5 ± 0.8	-1.4 ± 1.1	-0.5 ± 1.2	-0.7 ± 1.4	-0.6 ± 1.8
S_1	2.0 ± 0.2	2.0 ± 0.2	2.0 ± 0.2	1.6 ± 0.1	2.4 ± 0.5	1.9 ± 0.3	2.1 ± 0.5
S_2	1.05 ± 0.05	1.03 ± 0.05	0.99 ± 0.07	0.8 ± 0.1	1.10 ± 0.09	0.9 ± 0.1	1.1 ± 0.1
τ_b	1.28 ± 0.04	1.36 ± 0.05	1.36 ± 0.06	1.25 ± 0.06	1.32 ± 0.08	1.25 ± 0.09	1.4 ± 0.1
n_{bkg}	1330 ± 48	694 ± 35	350 ± 27	205 ± 20	137 ± 16	98 ± 14	60 ± 11
n_{sig}	6524 ± 87	4008 ± 68	2566 ± 54	1575 ± 42	1044 ± 34	672 ± 28	507 ± 24
n_p	5065 ± 78	2969 ± 59	1902 ± 47	1104 ± 36	691 ± 28	428 ± 23	312 ± 19
n_b	1459 ± 43	1039 ± 36	663 ± 28	471 ± 24	354 ± 20	244 ± 17	195 ± 15
n_{tail}	4.7 ± 4.2	2.9 ± 2.8	0.0 ± 1.3	1.7 ± 1.8	0.0 ± 1.0	4.3 ± 3.3	0.0 ± 1.1

Table D.3: The parameters of the invariant mass and t_z fit, including the fitted yields and shape parameters for different p_T bins in the rapidity bin $3.00 < y < 3.50$.

parameter	p_T (GeV/c)						
	0-1	1-2	2-3	3-4	4-5	5-6	6-7
$\mu_{J/\psi}$	3096.8 ± 0.1	3096.90 ± 0.07	3096.80 ± 0.07	3096.70 ± 0.08	3096.60 ± 0.10	3096.5 ± 0.1	3096.4 ± 0.2
σ_1	11.8 ± 0.1	12.01 ± 0.07	12.29 ± 0.07	12.67 ± 0.08	13.11 ± 0.09	13.4 ± 0.1	13.8 ± 0.1
β	0.49 ± 0.08	0.33 ± 0.05	0.39 ± 0.07	0.58 ± 0.10	0.32 ± 0.09	0.19 ± 0.05	0.3 ± 0.1
F_b	0.092 ± 0.003	0.108 ± 0.002	0.122 ± 0.002	0.137 ± 0.002	0.151 ± 0.003	0.166 ± 0.003	0.191 ± 0.005
F_b'	0.094 ± 0.003	0.1082 ± 0.0016	0.1224 ± 0.0017	0.1368 ± 0.0020	0.1505 ± 0.0025	0.1663 ± 0.0033	0.1910 ± 0.0045
$\mu * 1000$	-5.4 ± 0.5	-5.5 ± 0.3	-4.0 ± 0.3	-3.9 ± 0.3	-3.3 ± 0.3	-2.7 ± 0.4	-2.9 ± 0.4
S_1	1.48 ± 0.06	1.58 ± 0.06	1.49 ± 0.06	1.36 ± 0.05	1.6 ± 0.1	1.9 ± 0.1	1.7 ± 0.2
S_2	0.89 ± 0.04	0.94 ± 0.02	0.92 ± 0.03	0.86 ± 0.06	0.96 ± 0.04	1.01 ± 0.03	0.98 ± 0.07
τ_b	1.39 ± 0.05	1.57 ± 0.03	1.42 ± 0.02	1.43 ± 0.02	1.39 ± 0.03	1.35 ± 0.03	1.27 ± 0.03
n_{bkg}	192165 ± 503	273967 ± 605	168558 ± 478	56150 ± 282	16111 ± 157	5374 ± 94	2138 ± 62
n_{sig}	37342 ± 314	72612 ± 405	63917 ± 352	43833 ± 259	27769 ± 191	16695 ± 142	9974 ± 108
n_p	33843 ± 301	64752 ± 388	56097 ± 336	37835 ± 245	23588 ± 178	13919 ± 132	8069 ± 99
n_b	3497 ± 100	7860 ± 122	7822 ± 115	5998 ± 93	4181 ± 75	2776 ± 60	1905 ± 49
n_{tail}	684 ± 72	233 ± 52	159 ± 39	50 ± 22	5 ± 11	19.6 ± 9.3	11.7 ± 7.3
parameter	7-8	8-9	9-10	10-11	11-12	12-13	13-14
$\mu_{J/\psi}$	3096.3 ± 0.2	3096.2 ± 0.3	3097.0 ± 0.4	3096.5 ± 0.4	3096.9 ± 0.6	3095.4 ± 0.8	3096.6 ± 0.9
σ_1	14.3 ± 0.2	14.2 ± 0.2	15.0 ± 0.3	14.2 ± 0.4	16.4 ± 0.6	16.1 ± 0.7	15.3 ± 0.7
β	0.05 ± 0.02	0.3 ± 0.1	0.4 ± 0.3	0.7 ± 0.3	0.4 ± 0.2	0.7 ± 0.7	0.6 ± 0.6
F_b	0.215 ± 0.006	0.231 ± 0.008	0.26 ± 0.01	0.28 ± 0.01	0.27 ± 0.02	0.33 ± 0.02	0.34 ± 0.03
F_b'	0.2150 ± 0.0061	0.231 ± 0.008	0.261 ± 0.010	0.285 ± 0.014	0.268 ± 0.017	0.335 ± 0.022	0.348 ± 0.029
$\mu * 1000$	-3.0 ± 0.5	-3.7 ± 0.6	-1.0 ± 0.8	-2.6 ± 1.0	-1.5 ± 1.2	-0.2 ± 1.6	-2.1 ± 2.2
S_1	3.1 ± 0.6	1.7 ± 0.2	1.5 ± 0.3	1.3 ± 0.1	1.8 ± 0.3	1.3 ± 0.6	1.2 ± 2.3
S_2	1.10 ± 0.02	0.94 ± 0.06	1.0 ± 0.2	0.8 ± 0.2	0.9 ± 0.1	1.0 ± 1.0	1.1 ± 2.6
τ_b	1.35 ± 0.04	1.23 ± 0.05	1.38 ± 0.06	1.29 ± 0.08	1.22 ± 0.09	1.20 ± 0.09	1.2 ± 0.1
n_{bkg}	964 ± 43	520 ± 31	284 ± 24	200 ± 19	90 ± 14	56 ± 11	40.9 ± 9.1
n_{sig}	5780 ± 82	3445 ± 63	2112 ± 49	1344 ± 39	876 ± 31	567 ± 25	362 ± 20
n_p	4537 ± 73	2650 ± 55	1561 ± 42	962 ± 33	641 ± 27	377 ± 21	236 ± 17
n_b	1243 ± 39	795 ± 31	551 ± 26	382 ± 21	235 ± 17	190 ± 15	126 ± 12
n_{tail}	2.6 ± 2.6	4.2 ± 3.8	0.0 ± 2.8	4.9 ± 4.3	7.6 ± 4.3	0.0 ± 1.1	3.9 ± 2.7

Table D.4: The parameters of the invariant mass and t_z fit, including the fitted yields and shape parameters for different p_T bins in the rapidity bin $3.50 < y < 4.00$.

parameter	p_T (GeV/c)						
	0-1	1-2	2-3	3-4	4-5	5-6	6-7
$\mu_{J/\psi}$	3096.1 ± 0.1	3096.40 ± 0.09	3096.40 ± 0.09	3096.3 ± 0.1	3096.4 ± 0.1	3096.5 ± 0.2	3096.5 ± 0.2
σ_1	13.4 ± 0.1	13.73 ± 0.08	14.35 ± 0.09	14.8 ± 0.1	15.4 ± 0.1	16.1 ± 0.2	16.9 ± 0.2
β	0.3 ± 0.1	0.23 ± 0.07	0.25 ± 0.04	0.22 ± 0.06	0.15 ± 0.06	0.13 ± 0.05	0.11 ± 0.04
F_b	0.087 ± 0.003	0.101 ± 0.002	0.117 ± 0.002	0.128 ± 0.002	0.149 ± 0.003	0.153 ± 0.004	0.179 ± 0.005
F'_b	0.091 ± 0.003	0.1015 ± 0.0019	0.1170 ± 0.0019	0.1281 ± 0.0023	0.1493 ± 0.0030	0.1528 ± 0.0038	0.1789 ± 0.0053
$\mu * 1000$	-2.8 ± 0.5	-2.5 ± 0.4	-1.5 ± 0.3	-0.5 ± 0.3	-0.5 ± 0.4	-0.1 ± 0.4	0.3 ± 0.6
S_1	1.6 ± 0.2	1.7 ± 0.1	1.69 ± 0.08	1.7 ± 0.1	1.8 ± 0.2	2.0 ± 0.3	2.1 ± 0.3
S_2	0.93 ± 0.05	0.98 ± 0.03	0.96 ± 0.02	0.98 ± 0.03	1.03 ± 0.03	1.03 ± 0.03	1.06 ± 0.03
τ_b	1.34 ± 0.06	1.42 ± 0.03	1.47 ± 0.03	1.41 ± 0.03	1.38 ± 0.03	1.37 ± 0.04	1.33 ± 0.04
n_{bkg}	86248 ± 347	121364 ± 417	72942 ± 327	26209 ± 201	8585 ± 120	2967 ± 74	1264 ± 50
n_{sig}	30746 ± 255	56482 ± 330	47209 ± 285	31416 ± 213	20177 ± 161	12281 ± 122	6943 ± 90
n_p	27962 ± 248	50748 ± 319	41686 ± 272	27392 ± 203	17164 ± 151	10404 ± 113	5700 ± 83
n_b	2785 ± 91	5730 ± 108	5523 ± 95	4025 ± 77	3013 ± 64	1877 ± 50	1242 ± 40
n_{tail}	1060 ± 79	326 ± 54	55 ± 33	70 ± 26	15 ± 15	13.0 ± 8.4	6.0 ± 4.2
parameter	7-8	8-9	9-10	10-11	11-12	12-13	13-14
$\mu_{J/\psi}$	3096.3 ± 0.3	3096.9 ± 0.4	3096.3 ± 0.5	3096.7 ± 0.7	3097.1 ± 1.0	3096.4 ± 1.4	3097.6 ± 1.7
σ_1	17.3 ± 0.3	18.2 ± 0.4	18.1 ± 0.5	18.7 ± 0.6	19.3 ± 0.9	23.4 ± 1.3	23.3 ± 1.4
β	0.15 ± 0.04	0.4 ± 0.1	0.4 ± 0.3	0.8 ± 0.1	0.2 ± 0.3	0.1 ± 0.2	0.2 ± 0.1
F_b	0.204 ± 0.007	0.202 ± 0.009	0.26 ± 0.01	0.27 ± 0.02	0.27 ± 0.02	0.29 ± 0.03	0.37 ± 0.04
F'_b	0.204 ± 0.007	0.202 ± 0.009	0.263 ± 0.013	0.271 ± 0.017	0.269 ± 0.021	0.292 ± 0.027	0.367 ± 0.037
$\mu * 1000$	-0.0 ± 0.7	1.8 ± 0.8	0.2 ± 1.0	-0.3 ± 1.5	0.9 ± 1.7	-0.0 ± 2.1	1.5 ± 2.3
S_1	2.2 ± 0.2	1.6 ± 0.2	1.4 ± 0.3	1.32 ± 0.10	1.7 ± 0.6	2.4 ± 1.0	2.3 ± 0.9
S_2	1.01 ± 0.03	0.88 ± 0.09	0.9 ± 0.2	0.6 ± 0.2	1.1 ± 0.1	1.1 ± 0.2	0.9 ± 0.1
τ_b	1.27 ± 0.05	1.30 ± 0.07	1.24 ± 0.07	1.17 ± 0.09	1.3 ± 0.1	1.5 ± 0.2	1.3 ± 0.2
n_{bkg}	561 ± 35	321 ± 27	183 ± 20	101 ± 15	47 ± 11	20.9 ± 7.7	14.3 ± 6.1
n_{sig}	4091 ± 69	2433 ± 53	1487 ± 41	869 ± 31	528 ± 24	362 ± 20	225 ± 16
n_p	3254 ± 63	1940 ± 48	1095 ± 36	634 ± 27	387 ± 21	256 ± 18	142 ± 13
n_b	836 ± 33	492 ± 25	392 ± 22	235 ± 17	142 ± 13	106 ± 11	82.4 ± 9.8
n_{tail}	3.4 ± 4.1	3.2 ± 3.4	6.6 ± 4.6	5.1 ± 3.6	0.0 ± 1.4	0.0 ± 1.4	0.0 ± 1.1

Table D.5: The parameters of the invariant mass and t_z fit, including the fitted yields and shape parameters for different p_T bins in the rapidity bin $4.00 < y < 4.50$.

parameter	p_T (GeV/c)						
	0-1	1-2	2-3	3-4	4-5	5-6	6-7
$\mu_{J/\psi}$	3093.7 ± 0.2	3093.8 ± 0.1	3094.0 ± 0.2	3094.3 ± 0.2	3095.8 ± 0.3	3095.2 ± 0.4	3095.7 ± 0.5
σ_1	15.7 ± 0.2	16.0 ± 0.1	16.8 ± 0.2	17.4 ± 0.2	18.3 ± 0.2	19.9 ± 0.3	21.2 ± 0.4
β	0.056 ± 0.006	0.058 ± 0.005	0.19 ± 0.05	0.14 ± 0.06	0.19 ± 0.09	0.11 ± 0.04	0.8 ± 0.1
F_b	0.076 ± 0.004	0.086 ± 0.003	0.102 ± 0.003	0.117 ± 0.004	0.131 ± 0.005	0.136 ± 0.006	0.167 ± 0.009
F'_b	0.079 ± 0.005	0.086 ± 0.003	0.103 ± 0.003	0.117 ± 0.004	0.131 ± 0.005	0.1357 ± 0.0061	0.169 ± 0.009
$\mu * 1000$	-12.6 ± 0.9	-10.1 ± 0.6	-8.8 ± 0.6	-4.1 ± 0.7	1.1 ± 0.8	3.0 ± 0.9	3.1 ± 1.1
S_1	8.6 ± 1.1	4.8 ± 0.4	1.9 ± 0.2	2.1 ± 0.3	1.9 ± 0.2	2.4 ± 0.3	1.36 ± 0.07
S_2	1.12 ± 0.01	1.123 ± 0.009	1.02 ± 0.03	1.05 ± 0.04	1.03 ± 0.05	1.10 ± 0.03	0.7 ± 0.2
τ_b	1.6 ± 0.1	1.45 ± 0.05	1.39 ± 0.04	1.27 ± 0.05	1.32 ± 0.05	1.30 ± 0.06	1.16 ± 0.06
n_{bkg}	13172 ± 143	24665 ± 197	15070 ± 157	7727 ± 115	3357 ± 78	1391 ± 52	678 ± 38
n_{sig}	13744 ± 145	25550 ± 200	18570 ± 167	11631 ± 131	7359 ± 100	4536 ± 77	2760 ± 59
n_p	12656 ± 146	23343 ± 196	16664 ± 161	10273 ± 126	6395 ± 95	3920 ± 72	2295 ± 55
n_b	1088 ± 64	2208 ± 73	1906 ± 58	1357 ± 47	964 ± 38	615 ± 30	466 ± 26
n_{tail}	540 ± 61	198 ± 41	96 ± 25	16 ± 15	17 ± 12	0.0 ± 2.3	21.9 ± 9.3
parameter	7-8	8-9	9-10	10-11	11-12	12-13	13-14
$\mu_{J/\psi}$	3095.5 ± 0.7	3096.9 ± 0.9	3097.6 ± 1.2	3097.7 ± 1.5	3098.4 ± 2.0	3095.7 ± 2.6	3098.5 ± 3.2
σ_1	22.1 ± 0.6	23.1 ± 0.8	25.2 ± 1.2	25.1 ± 1.4	28.0 ± 1.7	28.0 ± 2.1	28.6 ± 2.8
β	0.6 ± 0.2	0.4 ± 0.2	0.1 ± 0.1	0.7 ± 0.2	0.4 ± 0.3	0.5 ± 0.7	0.5 ± 0.3
F_b	0.18 ± 0.01	0.20 ± 0.02	0.23 ± 0.02	0.29 ± 0.03	0.35 ± 0.03	0.23 ± 0.04	0.23 ± 0.04
F'_b	0.179 ± 0.011	0.199 ± 0.016	0.233 ± 0.022	0.290 ± 0.028	0.350 ± 0.033	0.24 ± 0.04	0.23 ± 0.04
$\mu * 1000$	4.5 ± 1.5	4.2 ± 1.8	8.0 ± 2.3	4.3 ± 3.3	6.4 ± 3.4	12.0 ± 4.5	3.9 ± 4.7
S_1	1.5 ± 0.2	1.6 ± 0.3	2.4 ± 0.6	1.5 ± 0.2	1.8 ± 0.5	1.3 ± 1.7	1.8 ± 0.5
S_2	0.8 ± 0.2	0.9 ± 0.1	1.12 ± 0.09	0.6 ± 0.2	0.9 ± 0.2	1.3 ± 1.3	0.8 ± 0.3
τ_b	1.36 ± 0.09	1.4 ± 0.1	0.92 ± 0.09	1.0 ± 0.1	1.1 ± 0.1	1.1 ± 0.2	1.1 ± 0.2
n_{bkg}	322 ± 27	169 ± 21	96 ± 17	52 ± 11	31.1 ± 9.7	18.5 ± 7.6	1.6 ± 1.6
n_{sig}	1592 ± 45	964 ± 35	602 ± 28	381 ± 21	254 ± 16	142 ± 12	109 ± 10
n_p	1307 ± 41	772 ± 32	462 ± 25	271 ± 19	165 ± 14	108.1 ± 9.7	84.0 ± 9.4
n_b	285 ± 20	192 ± 17	140 ± 15	111 ± 12	89 ± 10	33.6 ± 5.7	25.4 ± 5.5
n_{tail}	4.7 ± 4.5	12.3 ± 5.6	5.8 ± 4.1	0.0 ± 1.4	0.0 ± 1.3	3.2 ± 2.7	0.0 ± 1.5

Table E.1: The efficiency ϵ_{acc} in different bins of p_{T} and y for prompt J/ψ mesons.

p_{T} (GeV/ c)	$2 < y < 2.5$	$2.5 < y < 3$	$3 < y < 3.5$	$3.5 < y < 4$	$4 < y < 4.5$
0- 1	0.58 ± 0.01	0.82 ± 0.00	0.91 ± 0.00	0.91 ± 0.00	0.80 ± 0.01
1- 2	0.60 ± 0.00	0.83 ± 0.00	0.92 ± 0.00	0.91 ± 0.00	0.81 ± 0.00
2- 3	0.66 ± 0.00	0.87 ± 0.00	0.94 ± 0.00	0.93 ± 0.00	0.85 ± 0.00
3- 4	0.71 ± 0.00	0.90 ± 0.00	0.95 ± 0.00	0.95 ± 0.00	0.87 ± 0.00
4- 5	0.76 ± 0.00	0.93 ± 0.00	0.97 ± 0.00	0.97 ± 0.00	0.91 ± 0.00
5- 6	0.81 ± 0.00	0.94 ± 0.00	0.98 ± 0.00	0.97 ± 0.00	0.93 ± 0.00
6- 7	0.84 ± 0.01	0.96 ± 0.00	0.99 ± 0.00	0.98 ± 0.00	0.95 ± 0.00
7- 8	0.87 ± 0.01	0.97 ± 0.00	0.99 ± 0.00	0.98 ± 0.00	0.96 ± 0.01
8- 9	0.89 ± 0.01	0.97 ± 0.00	0.99 ± 0.00	0.99 ± 0.00	0.96 ± 0.01
9-10	0.91 ± 0.01	0.97 ± 0.01	0.99 ± 0.00	0.99 ± 0.00	0.97 ± 0.01
10-11	0.91 ± 0.01	0.98 ± 0.01	0.99 ± 0.00	0.99 ± 0.01	0.97 ± 0.01
11-12	0.92 ± 0.01	0.97 ± 0.01	1.00 ± 0.00	0.99 ± 0.01	0.95 ± 0.02
12-13	0.92 ± 0.02	0.99 ± 0.01	0.99 ± 0.01	1.00 ± 0.00	0.98 ± 0.01
13-14	0.93 ± 0.02	0.99 ± 0.01	0.99 ± 0.01	1.00 ± 0.00	0.98 ± 0.02

Table E.2: The efficiency ϵ_{acc} in different bins of p_{T} and y for from- b -decay J/ψ mesons.

p_{T} (GeV/ c)	$2 < y < 2.5$	$2.5 < y < 3$	$3 < y < 3.5$	$3.5 < y < 4$	$4 < y < 4.5$
0- 1	0.58 ± 0.01	0.84 ± 0.01	0.91 ± 0.01	0.91 ± 0.01	0.80 ± 0.01
1- 2	0.60 ± 0.01	0.85 ± 0.01	0.91 ± 0.01	0.91 ± 0.01	0.80 ± 0.01
2- 3	0.64 ± 0.01	0.86 ± 0.01	0.94 ± 0.00	0.92 ± 0.01	0.85 ± 0.01
3- 4	0.72 ± 0.01	0.90 ± 0.01	0.95 ± 0.01	0.95 ± 0.01	0.89 ± 0.01
4- 5	0.73 ± 0.01	0.92 ± 0.01	0.97 ± 0.00	0.97 ± 0.01	0.92 ± 0.01
5- 6	0.80 ± 0.01	0.94 ± 0.01	0.97 ± 0.01	0.98 ± 0.01	0.91 ± 0.01
6- 7	0.83 ± 0.01	0.95 ± 0.01	0.99 ± 0.00	0.96 ± 0.01	0.94 ± 0.01
7- 8	0.87 ± 0.01	0.96 ± 0.01	0.99 ± 0.00	0.98 ± 0.01	0.96 ± 0.01
8- 9	0.89 ± 0.02	0.97 ± 0.01	1.00 ± 0.00	1.00 ± 0.00	0.98 ± 0.02
9-10	0.89 ± 0.02	0.98 ± 0.01	1.00 ± 0.00	1.00 ± 0.00	0.98 ± 0.02
10-11	0.92 ± 0.02	0.99 ± 0.01	0.99 ± 0.01	0.95 ± 0.03	1.00 ± 0.00
11-12	0.93 ± 0.02	0.98 ± 0.01	1.00 ± 0.00	0.98 ± 0.02	1.00 ± 0.00
12-13	0.94 ± 0.03	0.98 ± 0.02	1.00 ± 0.00	1.00 ± 0.00	1.00 ± 0.00
13-14	0.94 ± 0.04	1.00 ± 0.00	1.00 ± 0.00	1.00 ± 0.00	1.00 ± 0.00

892 E Efficiency tables

Table E.3: The efficiency ϵ_{acc} in different bins of p_{T} and y averaged over prompt J/ψ and J/ψ from b mesons.

p_{T} (GeV/c)	$2 < y < 2.5$	$2.5 < y < 3$	$3 < y < 3.5$	$3.5 < y < 4$	$4 < y < 4.5$
0- 1	0.58 ± 0.00	0.82 ± 0.00	0.91 ± 0.00	0.91 ± 0.00	0.80 ± 0.00
1- 2	0.60 ± 0.00	0.84 ± 0.00	0.92 ± 0.00	0.91 ± 0.00	0.81 ± 0.00
2- 3	0.65 ± 0.00	0.87 ± 0.00	0.94 ± 0.00	0.93 ± 0.00	0.85 ± 0.00
3- 4	0.71 ± 0.00	0.90 ± 0.00	0.95 ± 0.00	0.95 ± 0.00	0.88 ± 0.00
4- 5	0.76 ± 0.00	0.93 ± 0.00	0.97 ± 0.00	0.97 ± 0.00	0.91 ± 0.00
5- 6	0.80 ± 0.00	0.94 ± 0.00	0.98 ± 0.00	0.97 ± 0.00	0.93 ± 0.00
6- 7	0.84 ± 0.00	0.96 ± 0.00	0.99 ± 0.00	0.98 ± 0.00	0.95 ± 0.00
7- 8	0.87 ± 0.01	0.97 ± 0.00	0.99 ± 0.00	0.98 ± 0.00	0.96 ± 0.01
8- 9	0.89 ± 0.01	0.97 ± 0.00	0.99 ± 0.00	0.99 ± 0.00	0.96 ± 0.01
9-10	0.91 ± 0.01	0.98 ± 0.00	0.99 ± 0.00	0.99 ± 0.00	0.98 ± 0.01
10-11	0.91 ± 0.01	0.98 ± 0.00	0.99 ± 0.00	0.98 ± 0.01	0.97 ± 0.01
11-12	0.93 ± 0.01	0.97 ± 0.01	1.00 ± 0.00	0.99 ± 0.01	0.96 ± 0.01
12-13	0.92 ± 0.01	0.99 ± 0.01	0.99 ± 0.01	1.00 ± 0.00	0.98 ± 0.01
13-14	0.93 ± 0.02	1.00 ± 0.00	0.99 ± 0.01	1.00 ± 0.00	0.98 ± 0.02

Table E.4: The efficiency $\epsilon_{\text{Reco\&Sel}}$ in different bins of p_{T} and y for prompt J/ψ mesons.

p_{T} (GeV/c)	$2 < y < 2.5$	$2.5 < y < 3$	$3 < y < 3.5$	$3.5 < y < 4$	$4 < y < 4.5$
0- 1	0.36 ± 0.00	0.61 ± 0.00	0.70 ± 0.00	0.69 ± 0.00	0.55 ± 0.00
1- 2	0.36 ± 0.00	0.57 ± 0.00	0.66 ± 0.00	0.65 ± 0.00	0.53 ± 0.00
2- 3	0.32 ± 0.00	0.53 ± 0.00	0.62 ± 0.00	0.62 ± 0.00	0.48 ± 0.00
3- 4	0.30 ± 0.00	0.53 ± 0.00	0.61 ± 0.00	0.60 ± 0.00	0.48 ± 0.00
4- 5	0.33 ± 0.00	0.56 ± 0.00	0.63 ± 0.00	0.63 ± 0.00	0.52 ± 0.00
5- 6	0.36 ± 0.00	0.59 ± 0.00	0.66 ± 0.00	0.66 ± 0.00	0.56 ± 0.00
6- 7	0.39 ± 0.00	0.62 ± 0.00	0.68 ± 0.00	0.68 ± 0.00	0.59 ± 0.00
7- 8	0.42 ± 0.00	0.64 ± 0.00	0.70 ± 0.00	0.70 ± 0.00	0.63 ± 0.00
8- 9	0.44 ± 0.00	0.66 ± 0.00	0.72 ± 0.00	0.72 ± 0.00	0.64 ± 0.01
9-10	0.45 ± 0.01	0.66 ± 0.01	0.73 ± 0.01	0.73 ± 0.01	0.67 ± 0.01
10-11	0.48 ± 0.01	0.67 ± 0.01	0.72 ± 0.01	0.75 ± 0.01	0.68 ± 0.01
11-12	0.47 ± 0.01	0.68 ± 0.01	0.73 ± 0.01	0.76 ± 0.01	0.69 ± 0.01
12-13	0.50 ± 0.01	0.70 ± 0.01	0.73 ± 0.01	0.75 ± 0.01	0.71 ± 0.02
13-14	0.50 ± 0.01	0.69 ± 0.01	0.77 ± 0.01	0.76 ± 0.01	0.67 ± 0.02

Table E.5: The efficiency $\epsilon_{\text{Reco\&Sel}}$ in different bins of p_T and y for from- b -decay J/ψ mesons.

p_T (GeV/c)	$2 < y < 2.5$	$2.5 < y < 3$	$3 < y < 3.5$	$3.5 < y < 4$	$4 < y < 4.5$
0- 1	0.34 ± 0.01	0.58 ± 0.00	0.67 ± 0.00	0.67 ± 0.00	0.53 ± 0.01
1- 2	0.34 ± 0.00	0.56 ± 0.00	0.64 ± 0.00	0.64 ± 0.00	0.52 ± 0.00
2- 3	0.31 ± 0.00	0.51 ± 0.00	0.61 ± 0.00	0.60 ± 0.00	0.46 ± 0.01
3- 4	0.28 ± 0.00	0.51 ± 0.00	0.59 ± 0.00	0.59 ± 0.00	0.47 ± 0.01
4- 5	0.31 ± 0.00	0.54 ± 0.00	0.61 ± 0.00	0.62 ± 0.01	0.50 ± 0.01
5- 6	0.34 ± 0.01	0.58 ± 0.01	0.64 ± 0.01	0.64 ± 0.01	0.54 ± 0.01
6- 7	0.36 ± 0.01	0.60 ± 0.01	0.67 ± 0.01	0.66 ± 0.01	0.61 ± 0.01
7- 8	0.40 ± 0.01	0.62 ± 0.01	0.67 ± 0.01	0.67 ± 0.01	0.60 ± 0.01
8- 9	0.42 ± 0.01	0.62 ± 0.01	0.68 ± 0.01	0.72 ± 0.01	0.64 ± 0.02
9-10	0.42 ± 0.01	0.65 ± 0.01	0.68 ± 0.01	0.67 ± 0.02	0.64 ± 0.02
10-11	0.41 ± 0.01	0.65 ± 0.01	0.72 ± 0.02	0.69 ± 0.02	0.66 ± 0.03
11-12	0.45 ± 0.02	0.66 ± 0.02	0.69 ± 0.02	0.70 ± 0.02	0.66 ± 0.03
12-13	0.45 ± 0.02	0.66 ± 0.02	0.74 ± 0.02	0.75 ± 0.03	0.67 ± 0.04
13-14	0.50 ± 0.02	0.67 ± 0.02	0.66 ± 0.03	0.75 ± 0.03	0.74 ± 0.05

Table E.6: The efficiency ϵ_{MuonID} in different bins of p_T and y for prompt J/ψ mesons.

p_T (GeV/c)	$2 < y < 2.5$	$2.5 < y < 3$	$3 < y < 3.5$	$3.5 < y < 4$	$4 < y < 4.5$
0- 1	0.81 ± 0.00	0.84 ± 0.00	0.82 ± 0.00	0.75 ± 0.00	0.65 ± 0.00
1- 2	0.79 ± 0.00	0.84 ± 0.00	0.84 ± 0.00	0.77 ± 0.00	0.62 ± 0.00
2- 3	0.80 ± 0.00	0.86 ± 0.00	0.85 ± 0.00	0.78 ± 0.00	0.59 ± 0.00
3- 4	0.82 ± 0.00	0.88 ± 0.00	0.87 ± 0.00	0.80 ± 0.00	0.55 ± 0.00
4- 5	0.84 ± 0.00	0.90 ± 0.00	0.89 ± 0.00	0.83 ± 0.00	0.57 ± 0.00
5- 6	0.86 ± 0.00	0.91 ± 0.00	0.91 ± 0.00	0.85 ± 0.00	0.59 ± 0.00
6- 7	0.87 ± 0.00	0.93 ± 0.00	0.93 ± 0.00	0.88 ± 0.00	0.61 ± 0.00
7- 8	0.89 ± 0.00	0.93 ± 0.00	0.94 ± 0.00	0.89 ± 0.00	0.63 ± 0.01
8- 9	0.91 ± 0.00	0.94 ± 0.00	0.93 ± 0.00	0.91 ± 0.00	0.65 ± 0.01
9-10	0.91 ± 0.00	0.95 ± 0.00	0.95 ± 0.00	0.91 ± 0.00	0.67 ± 0.01
10-11	0.92 ± 0.01	0.95 ± 0.00	0.95 ± 0.00	0.92 ± 0.01	0.70 ± 0.01
11-12	0.93 ± 0.01	0.96 ± 0.00	0.95 ± 0.00	0.93 ± 0.01	0.73 ± 0.01
12-13	0.92 ± 0.01	0.96 ± 0.01	0.96 ± 0.01	0.94 ± 0.01	0.73 ± 0.02
13-14	0.93 ± 0.01	0.95 ± 0.01	0.96 ± 0.01	0.94 ± 0.01	0.77 ± 0.02

Table E.7: The efficiency ϵ_{MuonID} in different bins of p_T and y for from- b -decay J/ψ mesons.

p_T (GeV/c)	$2 < y < 2.5$	$2.5 < y < 3$	$3 < y < 3.5$	$3.5 < y < 4$	$4 < y < 4.5$
0- 1	0.80 ± 0.01	0.84 ± 0.00	0.82 ± 0.00	0.75 ± 0.01	0.64 ± 0.01
1- 2	0.79 ± 0.01	0.84 ± 0.00	0.83 ± 0.00	0.77 ± 0.00	0.63 ± 0.01
2- 3	0.79 ± 0.01	0.86 ± 0.00	0.85 ± 0.00	0.78 ± 0.00	0.60 ± 0.01
3- 4	0.82 ± 0.01	0.87 ± 0.00	0.87 ± 0.00	0.79 ± 0.01	0.57 ± 0.01
4- 5	0.84 ± 0.01	0.90 ± 0.00	0.89 ± 0.00	0.84 ± 0.01	0.57 ± 0.01
5- 6	0.86 ± 0.01	0.91 ± 0.00	0.91 ± 0.00	0.86 ± 0.01	0.57 ± 0.01
6- 7	0.88 ± 0.01	0.93 ± 0.00	0.91 ± 0.01	0.89 ± 0.01	0.61 ± 0.01
7- 8	0.88 ± 0.01	0.93 ± 0.01	0.93 ± 0.01	0.87 ± 0.01	0.63 ± 0.02
8- 9	0.91 ± 0.01	0.94 ± 0.01	0.93 ± 0.01	0.91 ± 0.01	0.70 ± 0.02
9-10	0.91 ± 0.01	0.96 ± 0.01	0.94 ± 0.01	0.92 ± 0.01	0.69 ± 0.03
10-11	0.93 ± 0.01	0.94 ± 0.01	0.96 ± 0.01	0.90 ± 0.02	0.66 ± 0.03
11-12	0.92 ± 0.01	0.93 ± 0.01	0.94 ± 0.01	0.90 ± 0.02	0.65 ± 0.04
12-13	0.92 ± 0.02	0.96 ± 0.01	0.92 ± 0.02	0.91 ± 0.02	0.73 ± 0.04
13-14	0.92 ± 0.02	0.96 ± 0.01	0.96 ± 0.01	0.91 ± 0.03	0.64 ± 0.07

Table E.8: The efficiency ϵ_{MuonID} in different bins of p_T and y averaged over prompt J/ψ and J/ψ from b mesons.

p_T (GeV/c)	$2 < y < 2.5$	$2.5 < y < 3$	$3 < y < 3.5$	$3.5 < y < 4$	$4 < y < 4.5$
0- 1	0.81 ± 0.00	0.84 ± 0.00	0.82 ± 0.00	0.75 ± 0.00	0.65 ± 0.00
1- 2	0.79 ± 0.00	0.84 ± 0.00	0.83 ± 0.00	0.77 ± 0.00	0.62 ± 0.00
2- 3	0.80 ± 0.00	0.86 ± 0.00	0.85 ± 0.00	0.78 ± 0.00	0.59 ± 0.00
3- 4	0.82 ± 0.00	0.88 ± 0.00	0.87 ± 0.00	0.80 ± 0.00	0.56 ± 0.00
4- 5	0.84 ± 0.00	0.90 ± 0.00	0.89 ± 0.00	0.83 ± 0.00	0.57 ± 0.00
5- 6	0.86 ± 0.00	0.91 ± 0.00	0.91 ± 0.00	0.85 ± 0.00	0.59 ± 0.00
6- 7	0.88 ± 0.00	0.93 ± 0.00	0.92 ± 0.00	0.88 ± 0.00	0.61 ± 0.00
7- 8	0.89 ± 0.00	0.93 ± 0.00	0.93 ± 0.00	0.89 ± 0.00	0.63 ± 0.01
8- 9	0.91 ± 0.00	0.94 ± 0.00	0.93 ± 0.00	0.91 ± 0.00	0.66 ± 0.01
9-10	0.91 ± 0.00	0.95 ± 0.00	0.94 ± 0.00	0.91 ± 0.00	0.68 ± 0.01
10-11	0.92 ± 0.01	0.95 ± 0.00	0.96 ± 0.00	0.92 ± 0.01	0.69 ± 0.01
11-12	0.93 ± 0.01	0.95 ± 0.00	0.95 ± 0.00	0.92 ± 0.01	0.72 ± 0.01
12-13	0.92 ± 0.01	0.96 ± 0.00	0.95 ± 0.01	0.93 ± 0.01	0.73 ± 0.02
13-14	0.93 ± 0.01	0.96 ± 0.01	0.96 ± 0.01	0.93 ± 0.01	0.75 ± 0.02

Table E.9: The efficiency $\epsilon_{\text{Trigger}}$ in different bins of p_T and y for prompt J/ψ mesons.

p_T (GeV/c)	$2 < y < 2.5$	$2.5 < y < 3$	$3 < y < 3.5$	$3.5 < y < 4$	$4 < y < 4.5$
0- 1	0.58 ± 0.00	0.74 ± 0.00	0.80 ± 0.00	0.80 ± 0.00	0.68 ± 0.00
1- 2	0.67 ± 0.00	0.79 ± 0.00	0.82 ± 0.00	0.81 ± 0.00	0.73 ± 0.00
2- 3	0.74 ± 0.00	0.82 ± 0.00	0.85 ± 0.00	0.82 ± 0.00	0.75 ± 0.00
3- 4	0.77 ± 0.00	0.86 ± 0.00	0.87 ± 0.00	0.85 ± 0.00	0.77 ± 0.00
4- 5	0.80 ± 0.00	0.88 ± 0.00	0.89 ± 0.00	0.86 ± 0.00	0.80 ± 0.00
5- 6	0.83 ± 0.00	0.89 ± 0.00	0.90 ± 0.00	0.88 ± 0.00	0.82 ± 0.00
6- 7	0.84 ± 0.00	0.90 ± 0.00	0.90 ± 0.00	0.89 ± 0.00	0.83 ± 0.00
7- 8	0.86 ± 0.00	0.90 ± 0.00	0.90 ± 0.00	0.89 ± 0.00	0.84 ± 0.01
8- 9	0.86 ± 0.00	0.90 ± 0.00	0.90 ± 0.00	0.90 ± 0.00	0.84 ± 0.01
9-10	0.88 ± 0.01	0.92 ± 0.00	0.91 ± 0.00	0.90 ± 0.01	0.86 ± 0.01
10-11	0.86 ± 0.01	0.93 ± 0.00	0.91 ± 0.01	0.88 ± 0.01	0.87 ± 0.01
11-12	0.89 ± 0.01	0.92 ± 0.01	0.90 ± 0.01	0.90 ± 0.01	0.86 ± 0.01
12-13	0.89 ± 0.01	0.91 ± 0.01	0.89 ± 0.01	0.89 ± 0.01	0.87 ± 0.02
13-14	0.89 ± 0.01	0.92 ± 0.01	0.90 ± 0.01	0.88 ± 0.01	0.88 ± 0.02

Table E.10: The efficiency $\epsilon_{\text{Trigger}}$ in different bins of p_T and y for from- b -decay J/ψ mesons.

p_T (GeV/c)	$2 < y < 2.5$	$2.5 < y < 3$	$3 < y < 3.5$	$3.5 < y < 4$	$4 < y < 4.5$
0- 1	0.60 ± 0.01	0.75 ± 0.01	0.80 ± 0.01	0.80 ± 0.01	0.68 ± 0.01
1- 2	0.67 ± 0.01	0.80 ± 0.00	0.82 ± 0.00	0.80 ± 0.00	0.71 ± 0.01
2- 3	0.74 ± 0.01	0.82 ± 0.00	0.84 ± 0.00	0.82 ± 0.00	0.74 ± 0.01
3- 4	0.78 ± 0.01	0.85 ± 0.00	0.86 ± 0.00	0.85 ± 0.01	0.76 ± 0.01
4- 5	0.80 ± 0.01	0.88 ± 0.00	0.89 ± 0.00	0.87 ± 0.01	0.80 ± 0.01
5- 6	0.82 ± 0.01	0.89 ± 0.00	0.89 ± 0.01	0.88 ± 0.01	0.82 ± 0.01
6- 7	0.85 ± 0.01	0.89 ± 0.01	0.90 ± 0.01	0.88 ± 0.01	0.81 ± 0.01
7- 8	0.85 ± 0.01	0.90 ± 0.01	0.89 ± 0.01	0.90 ± 0.01	0.82 ± 0.02
8- 9	0.85 ± 0.01	0.91 ± 0.01	0.91 ± 0.01	0.89 ± 0.01	0.87 ± 0.02
9-10	0.87 ± 0.01	0.92 ± 0.01	0.90 ± 0.01	0.90 ± 0.01	0.88 ± 0.02
10-11	0.90 ± 0.01	0.91 ± 0.01	0.89 ± 0.01	0.89 ± 0.02	0.83 ± 0.03
11-12	0.88 ± 0.02	0.91 ± 0.01	0.90 ± 0.02	0.87 ± 0.02	0.83 ± 0.04
12-13	0.88 ± 0.02	0.91 ± 0.02	0.86 ± 0.02	0.90 ± 0.02	0.80 ± 0.05
13-14	0.87 ± 0.02	0.91 ± 0.02	0.89 ± 0.02	0.88 ± 0.03	0.85 ± 0.06

Table E.11: The efficiency $\epsilon_{\text{Trigger}}$ in different bins of p_{T} and y averaged over prompt J/ψ and J/ψ from b mesons.

p_{T} (GeV/c)	$2 < y < 2.5$	$2.5 < y < 3$	$3 < y < 3.5$	$3.5 < y < 4$	$4 < y < 4.5$
0- 1	0.58 ± 0.00	0.74 ± 0.00	0.80 ± 0.00	0.80 ± 0.00	0.68 ± 0.00
1- 2	0.67 ± 0.00	0.80 ± 0.00	0.82 ± 0.00	0.81 ± 0.00	0.73 ± 0.00
2- 3	0.74 ± 0.00	0.82 ± 0.00	0.85 ± 0.00	0.82 ± 0.00	0.75 ± 0.00
3- 4	0.77 ± 0.00	0.86 ± 0.00	0.87 ± 0.00	0.85 ± 0.00	0.77 ± 0.00
4- 5	0.80 ± 0.00	0.88 ± 0.00	0.89 ± 0.00	0.87 ± 0.00	0.80 ± 0.00
5- 6	0.83 ± 0.00	0.89 ± 0.00	0.90 ± 0.00	0.88 ± 0.00	0.82 ± 0.00
6- 7	0.84 ± 0.00	0.90 ± 0.00	0.90 ± 0.00	0.89 ± 0.00	0.83 ± 0.00
7- 8	0.86 ± 0.00	0.90 ± 0.00	0.90 ± 0.00	0.90 ± 0.00	0.84 ± 0.01
8- 9	0.86 ± 0.00	0.91 ± 0.00	0.90 ± 0.00	0.90 ± 0.00	0.85 ± 0.01
9-10	0.88 ± 0.01	0.92 ± 0.00	0.91 ± 0.00	0.90 ± 0.00	0.86 ± 0.01
10-11	0.87 ± 0.01	0.92 ± 0.00	0.91 ± 0.01	0.88 ± 0.01	0.86 ± 0.01
11-12	0.89 ± 0.01	0.92 ± 0.01	0.90 ± 0.01	0.89 ± 0.01	0.86 ± 0.01
12-13	0.89 ± 0.01	0.91 ± 0.01	0.89 ± 0.01	0.89 ± 0.01	0.86 ± 0.01
13-14	0.89 ± 0.01	0.92 ± 0.01	0.90 ± 0.01	0.88 ± 0.01	0.88 ± 0.02

Table E.12: The efficiency ϵ_{tot} in different bins of p_{T} and y for prompt J/ψ .

p_{T} (GeV/c)	$2 < y < 2.5$	$2.5 < y < 3$	$3 < y < 3.5$	$3.5 < y < 4$	$4 < y < 4.5$
0- 1	0.10 ± 0.00	0.31 ± 0.00	0.42 ± 0.00	0.38 ± 0.00	0.19 ± 0.00
1- 2	0.11 ± 0.00	0.32 ± 0.00	0.41 ± 0.00	0.37 ± 0.00	0.19 ± 0.00
2- 3	0.12 ± 0.00	0.33 ± 0.00	0.42 ± 0.00	0.37 ± 0.00	0.18 ± 0.00
3- 4	0.14 ± 0.00	0.36 ± 0.00	0.44 ± 0.00	0.39 ± 0.00	0.18 ± 0.00
4- 5	0.17 ± 0.00	0.41 ± 0.00	0.49 ± 0.00	0.44 ± 0.00	0.22 ± 0.00
5- 6	0.20 ± 0.00	0.45 ± 0.00	0.53 ± 0.00	0.48 ± 0.00	0.25 ± 0.00
6- 7	0.24 ± 0.00	0.50 ± 0.00	0.56 ± 0.00	0.52 ± 0.00	0.29 ± 0.00
7- 8	0.28 ± 0.00	0.52 ± 0.00	0.58 ± 0.00	0.55 ± 0.00	0.32 ± 0.00
8- 9	0.31 ± 0.00	0.55 ± 0.00	0.60 ± 0.00	0.58 ± 0.01	0.34 ± 0.01
9-10	0.32 ± 0.01	0.57 ± 0.01	0.62 ± 0.01	0.59 ± 0.01	0.38 ± 0.01
10-11	0.34 ± 0.01	0.58 ± 0.01	0.62 ± 0.01	0.59 ± 0.01	0.40 ± 0.01
11-12	0.36 ± 0.01	0.58 ± 0.01	0.63 ± 0.01	0.62 ± 0.01	0.41 ± 0.01
12-13	0.38 ± 0.01	0.61 ± 0.01	0.62 ± 0.01	0.63 ± 0.01	0.44 ± 0.02
13-14	0.38 ± 0.01	0.60 ± 0.01	0.66 ± 0.01	0.63 ± 0.02	0.44 ± 0.02

Table E.13: The efficiency ϵ_{tot} in different bins of p_{T} and y averaged for J/ψ from b mesons.

p_{T} (GeV/ c)	$2 < y < 2.5$	$2.5 < y < 3$	$3 < y < 3.5$	$3.5 < y < 4$	$4 < y < 4.5$
0- 1	0.09 ± 0.00	0.30 ± 0.00	0.40 ± 0.00	0.37 ± 0.00	0.19 ± 0.00
1- 2	0.11 ± 0.00	0.31 ± 0.00	0.40 ± 0.00	0.36 ± 0.00	0.19 ± 0.00
2- 3	0.12 ± 0.00	0.32 ± 0.00	0.41 ± 0.00	0.36 ± 0.00	0.17 ± 0.00
3- 4	0.13 ± 0.00	0.34 ± 0.00	0.43 ± 0.00	0.38 ± 0.00	0.17 ± 0.00
4- 5	0.16 ± 0.00	0.39 ± 0.00	0.47 ± 0.00	0.43 ± 0.00	0.21 ± 0.00
5- 6	0.19 ± 0.00	0.44 ± 0.00	0.51 ± 0.00	0.46 ± 0.01	0.24 ± 0.00
6- 7	0.22 ± 0.00	0.48 ± 0.01	0.55 ± 0.01	0.51 ± 0.01	0.29 ± 0.01
7- 8	0.26 ± 0.01	0.50 ± 0.01	0.56 ± 0.01	0.52 ± 0.01	0.30 ± 0.01
8- 9	0.29 ± 0.01	0.51 ± 0.01	0.57 ± 0.01	0.58 ± 0.01	0.34 ± 0.01
9-10	0.30 ± 0.01	0.56 ± 0.01	0.58 ± 0.01	0.54 ± 0.01	0.37 ± 0.01
10-11	0.30 ± 0.01	0.56 ± 0.01	0.62 ± 0.01	0.55 ± 0.02	0.38 ± 0.02
11-12	0.35 ± 0.01	0.56 ± 0.02	0.59 ± 0.02	0.57 ± 0.02	0.39 ± 0.02
12-13	0.34 ± 0.02	0.58 ± 0.02	0.62 ± 0.02	0.63 ± 0.03	0.41 ± 0.03
13-14	0.39 ± 0.02	0.59 ± 0.02	0.57 ± 0.03	0.61 ± 0.03	0.48 ± 0.04

F Cross section result tables

Table F.1: Double differential production cross section (in nb) for prompt J/ψ . The first uncertainty is statistical, the second correlated systematic uncertainty shared between the bins and the last uncorrelated systematic uncertainty.

p_T (GeV/ c)	$2.0 < y < 2.5$	$2.5 < y < 3.0$	$3.0 < y < 3.5$
0– 1	$1059.0 \pm 16.4 \pm 45.6 \pm 31.8$	$947.0 \pm 8.9 \pm 38.1 \pm 7.9$	$860.6 \pm 7.6 \pm 38.8 \pm 4.7$
1– 2	$2078.5 \pm 21.6 \pm 88.6 \pm 17.0$	$1878.1 \pm 12.2 \pm 75.4 \pm 11.2$	$1682.8 \pm 10.1 \pm 76.7 \pm 6.1$
2– 3	$1863.2 \pm 18.0 \pm 78.2 \pm 17.2$	$1657.9 \pm 10.5 \pm 66.4 \pm 12.6$	$1431.0 \pm 8.6 \pm 63.4 \pm 5.2$
3– 4	$1218.2 \pm 12.9 \pm 50.7 \pm 14.3$	$1061.9 \pm 7.4 \pm 42.5 \pm 5.8$	$928.1 \pm 6.0 \pm 39.1 \pm 3.3$
4– 5	$755.1 \pm 8.5 \pm 31.0 \pm 9.3$	$620.4 \pm 4.8 \pm 24.8 \pm 4.2$	$526.5 \pm 4.0 \pm 21.6 \pm 2.0$
5– 6	$418.7 \pm 5.5 \pm 17.1 \pm 4.5$	$351.0 \pm 3.3 \pm 14.0 \pm 2.3$	$288.2 \pm 2.7 \pm 11.7 \pm 1.3$
6– 7	$236.7 \pm 3.7 \pm 9.6 \pm 7.4$	$188.4 \pm 2.2 \pm 7.5 \pm 1.3$	$157.8 \pm 1.9 \pm 6.4 \pm 0.9$
7– 8	$130.2 \pm 2.5 \pm 5.3 \pm 3.8$	$104.0 \pm 1.6 \pm 4.2 \pm 0.8$	$85.6 \pm 1.4 \pm 3.4 \pm 0.6$
8– 9	$76.0 \pm 1.8 \pm 3.1 \pm 1.4$	$58.2 \pm 1.2 \pm 2.3 \pm 0.6$	$48.3 \pm 1.0 \pm 1.9 \pm 0.4$
9–10	$47.0 \pm 1.3 \pm 1.9 \pm 1.1$	$36.0 \pm 0.9 \pm 1.4 \pm 0.4$	$27.3 \pm 0.7 \pm 1.1 \pm 0.3$
10–11	$28.7 \pm 1.0 \pm 1.1 \pm 0.6$	$20.6 \pm 0.7 \pm 0.8 \pm 0.4$	$16.9 \pm 0.6 \pm 0.7 \pm 0.2$
11–12	$16.9 \pm 0.8 \pm 0.7 \pm 0.5$	$12.7 \pm 0.5 \pm 0.5 \pm 0.2$	$11.0 \pm 0.5 \pm 0.4 \pm 0.2$
12–13	$11.5 \pm 0.6 \pm 0.5 \pm 0.4$	$7.5 \pm 0.4 \pm 0.3 \pm 0.2$	$6.6 \pm 0.4 \pm 0.3 \pm 0.1$
13–14	$7.2 \pm 0.5 \pm 0.3 \pm 0.3$	$5.5 \pm 0.3 \pm 0.2 \pm 0.1$	$3.9 \pm 0.3 \pm 0.2 \pm 0.1$
	$3.5 < y < 4.0$	$4.0 < y < 4.5$	
0– 1	$806.9 \pm 7.2 \pm 45.3 \pm 4.8$	$724.0 \pm 8.4 \pm 47.8 \pm 8.6$	
1– 2	$1502.5 \pm 9.4 \pm 87.1 \pm 5.9$	$1333.0 \pm 11.2 \pm 95.1 \pm 17.4$	
2– 3	$1238.8 \pm 8.1 \pm 68.8 \pm 5.0$	$1009.7 \pm 9.8 \pm 72.8 \pm 14.4$	
3– 4	$771.6 \pm 5.7 \pm 39.8 \pm 3.1$	$623.6 \pm 7.6 \pm 41.9 \pm 10.8$	
4– 5	$429.2 \pm 3.8 \pm 20.3 \pm 2.0$	$321.5 \pm 4.8 \pm 18.8 \pm 7.3$	
5– 6	$236.6 \pm 2.6 \pm 10.7 \pm 1.2$	$169.0 \pm 3.1 \pm 9.1 \pm 3.4$	
6– 7	$119.6 \pm 1.7 \pm 5.2 \pm 0.8$	$87.3 \pm 2.1 \pm 4.5 \pm 1.0$	
7– 8	$64.6 \pm 1.2 \pm 2.8 \pm 0.5$	$44.8 \pm 1.4 \pm 2.2 \pm 1.3$	
8– 9	$36.3 \pm 0.9 \pm 1.5 \pm 0.3$	$24.4 \pm 1.0 \pm 1.2 \pm 1.0$	
9–10	$20.1 \pm 0.7 \pm 0.8 \pm 0.2$	$13.1 \pm 0.7 \pm 0.6 \pm 0.4$	
10–11	$11.6 \pm 0.5 \pm 0.5 \pm 0.2$	$7.4 \pm 0.5 \pm 0.3 \pm 0.4$	
11–12	$6.8 \pm 0.4 \pm 0.3 \pm 0.1$	$4.4 \pm 0.4 \pm 0.2 \pm 0.2$	
12–13	$4.4 \pm 0.3 \pm 0.2 \pm 0.1$	$2.7 \pm 0.2 \pm 0.1 \pm 0.1$	
13–14	$2.5 \pm 0.2 \pm 0.1 \pm 0.1$	$2.1 \pm 0.2 \pm 0.1 \pm 0.1$	

Table F.2: Double differential production cross section (in nb) for J/ψ -from- b . The first uncertainty is statistical, the second correlated systematic uncertainty shared between the bins and the last uncorrelated systematic uncertainty.

p_T (GeV/ c)	$2.0 < y < 2.5$	$2.5 < y < 3.0$	$3.0 < y < 3.5$
0– 1	$113.2 \pm 5.4 \pm 6.7 \pm 3.7$	$102.3 \pm 2.9 \pm 5.3 \pm 1.1$	$92.7 \pm 2.6 \pm 5.0 \pm 0.8$
1– 2	$276.3 \pm 6.9 \pm 15.5 \pm 3.4$	$243.6 \pm 3.9 \pm 12.4 \pm 2.0$	$209.3 \pm 3.3 \pm 11.4 \pm 1.3$
2– 3	$300.6 \pm 6.4 \pm 16.2 \pm 4.1$	$249.4 \pm 3.6 \pm 12.6 \pm 2.5$	$204.5 \pm 3.0 \pm 10.9 \pm 1.3$
3– 4	$238.6 \pm 5.3 \pm 12.6 \pm 4.0$	$186.8 \pm 2.9 \pm 9.4 \pm 1.7$	$152.4 \pm 2.4 \pm 7.8 \pm 1.1$
4– 5	$159.9 \pm 3.8 \pm 8.3 \pm 2.9$	$126.3 \pm 2.1 \pm 6.3 \pm 1.3$	$97.2 \pm 1.7 \pm 4.9 \pm 0.8$
5– 6	$103.3 \pm 2.8 \pm 5.3 \pm 1.9$	$78.5 \pm 1.5 \pm 3.9 \pm 0.9$	$59.2 \pm 1.3 \pm 3.0 \pm 0.6$
6– 7	$67.9 \pm 2.0 \pm 3.4 \pm 2.4$	$52.1 \pm 1.2 \pm 2.6 \pm 0.7$	$38.0 \pm 1.0 \pm 1.9 \pm 0.4$
7– 8	$42.9 \pm 1.5 \pm 2.2 \pm 1.5$	$31.2 \pm 0.9 \pm 1.6 \pm 0.5$	$24.3 \pm 0.8 \pm 1.2 \pm 0.3$
8– 9	$25.3 \pm 1.1 \pm 1.3 \pm 0.7$	$21.9 \pm 0.7 \pm 1.1 \pm 0.4$	$15.2 \pm 0.6 \pm 0.8 \pm 0.3$
9–10	$18.9 \pm 0.9 \pm 0.9 \pm 0.7$	$12.8 \pm 0.5 \pm 0.6 \pm 0.3$	$10.3 \pm 0.5 \pm 0.5 \pm 0.2$
10–11	$14.2 \pm 0.8 \pm 0.7 \pm 0.5$	$9.1 \pm 0.5 \pm 0.5 \pm 0.2$	$6.7 \pm 0.4 \pm 0.3 \pm 0.2$
11–12	$9.0 \pm 0.6 \pm 0.4 \pm 0.4$	$6.8 \pm 0.4 \pm 0.3 \pm 0.2$	$4.3 \pm 0.3 \pm 0.2 \pm 0.1$
12–13	$6.5 \pm 0.5 \pm 0.3 \pm 0.3$	$4.5 \pm 0.3 \pm 0.2 \pm 0.2$	$3.3 \pm 0.3 \pm 0.2 \pm 0.1$
13–14	$4.9 \pm 0.4 \pm 0.2 \pm 0.3$	$3.6 \pm 0.3 \pm 0.2 \pm 0.1$	$2.4 \pm 0.2 \pm 0.1 \pm 0.1$
	$3.5 < y < 4.0$	$4.0 < y < 4.5$	
0– 1	$83.4 \pm 2.7 \pm 5.3 \pm 0.8$	$64.9 \pm 3.8 \pm 4.7 \pm 1.1$	
1– 2	$174.0 \pm 3.3 \pm 11.3 \pm 1.2$	$129.5 \pm 4.3 \pm 10.0 \pm 2.0$	
2– 3	$168.5 \pm 2.9 \pm 10.6 \pm 1.3$	$121.2 \pm 3.7 \pm 9.4 \pm 2.1$	
3– 4	$117.0 \pm 2.2 \pm 6.9 \pm 1.0$	$84.7 \pm 2.9 \pm 6.2 \pm 1.8$	
4– 5	$76.7 \pm 1.6 \pm 4.3 \pm 0.7$	$50.5 \pm 2.0 \pm 3.3 \pm 1.3$	
5– 6	$44.2 \pm 1.2 \pm 2.4 \pm 0.5$	$27.9 \pm 1.3 \pm 1.7 \pm 0.7$	
6– 7	$26.7 \pm 0.9 \pm 1.4 \pm 0.4$	$17.2 \pm 1.0 \pm 1.0 \pm 0.4$	
7– 8	$17.4 \pm 0.7 \pm 0.9 \pm 0.3$	$10.2 \pm 0.7 \pm 0.6 \pm 0.4$	
8– 9	$9.2 \pm 0.5 \pm 0.5 \pm 0.2$	$6.1 \pm 0.5 \pm 0.3 \pm 0.3$	
9–10	$7.8 \pm 0.4 \pm 0.4 \pm 0.2$	$4.2 \pm 0.4 \pm 0.2 \pm 0.2$	
10–11	$4.7 \pm 0.3 \pm 0.2 \pm 0.1$	$3.1 \pm 0.3 \pm 0.2 \pm 0.2$	
11–12	$2.7 \pm 0.3 \pm 0.1 \pm 0.1$	$2.5 \pm 0.3 \pm 0.1 \pm 0.1$	
12–13	$1.8 \pm 0.2 \pm 0.1 \pm 0.1$	$0.9 \pm 0.2 \pm 0.1 \pm 0.1$	
13–14	$1.5 \pm 0.2 \pm 0.1 \pm 0.1$	$0.6 \pm 0.1 \pm 0.0 \pm 0.1$	

G Modelling of t_z resolution

Reconstructed J/ψ candidate can be wrongly associated with another PV found in the event, since the true primary vertex is not found because of too few tracks originating from the vertex, as explained in section 5.1. These events corresponds to a t_z distribution with a large resolution. To account for these events, a third wide Gaussian was added to the resolution function and is compared to the nominal fit with 2 Gaussian in the resolution function in Fig. G.1 on the left. Even though from the fit comparison one would conclude that adding the third wide Gaussian helps to fit also events between 0 to -2 ps properly, the fitted results give different results. Comparing to the MC truth informations the fit including three resolution functions returns the wrong number of signal and background events, compared to the nominal one as shown in Table G.1. The fraction of this third Gaussian is really small of order of 1%, its effect can only be seen because of the logarithmic scale. From these studies it is concluded that including a third wide Gaussian for the resolution will not improve the result significantly, and two Gaussians are sufficiently good.

Table G.1: Comparison of MC truth to fitted parameters of the invariant mass and t_z fit with two Gaussian and three Gaussian for the resolution function, a high statistics bin is taken $3 < y < 3.5$, $3 < p_T < 4 \text{ GeV}/c^2$.

	MCTruth	Fit 2 Gaussian resolution	Fit 3 Gaussian resolution
# of signal events	21210	$21210 \pm (-150.85, 151.23)$	$21216 \pm (-150.86, 151.35)$
# of background events	419	$419.28 \pm (-44.434, 45.516)$	$413.48 \pm (-44.582, 45.519)$
b_{frac}	0.102782 ± 0.00208515	$0.10150 \pm (-0.0025577, 0.0025914)$	$0.099487 \pm (-0.0026358, 0.0026683)$

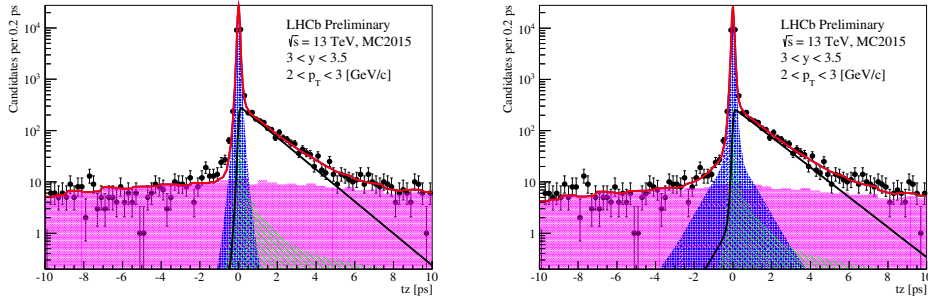


Figure G.1: The t_z distribution in the high statistics bin $3 < y < 3.5$, $3 < p_T < 4 \text{ GeV}/c^2$ fitted with 2 Gaussian(left) and an additional wide Gaussian (right) for the resolution function.

H Introduction to trigger-based analysis

Increased computing power of the LHCb experiment together with reoptimized trigger deferral, and applied online calibration and alignment made possible to implement the Turbo stream strategy. The concept of Turbo stream consists of the offline quality trigger reconstruction to perform physics measurements. Turbo stream trigger lines are saving detailed information on triggered decays, which contains kinematic variables of reconstructed particles, such as vertice information, PID variables etc. This information from Turbo stream trigger lines can be converted to conventional LHCb decay candidates and written to usual .dst files by the Tesla application. Thus, the link of Turbo stream lines and Tesla in a way is similar to usual trigger and reconstruction sequence applied in Run I, but one should keep in mind, that the Turbo stream approach doesn't imply full event reconstruction, which means that Tesla candidates will contain only information from corresponding Turbo stream line and no other information will be available in the analysis. As a practical consequence of this feature for this particular analysis one can name absence of TISTOS technique in its usual sense. On the other hand, this approach gives significant time gain, which is crucial for any early measurement analysis.

I Comparision of Tesla and stripping candidates

A MC simulation study was performed in order to estimate the effect of the new reconstruction approach on physical results. For this study 959006 events were simulated. From this number, Tesla and offline-reconstructed candidates are created and compared. Tesla candidates are created with Hlt2DiMuonJPsiTurbo trigger line. Offline candidates are combinations of opposite charge muons from StdAllLooseMuons. Cuts identical to ones applied to trigger candidates are also applied to offline candidates in order to provide comparison (see tab.3.2).

Offline and Tesla candidates from the same event were matched (in case of reconstruction of both offline and Tesla candidates) basing on common hits in LHCb detector. The maximal fraction of common hits was used as a quantitative measure of similarity of Tesla and offline candidates (see Fig. I.1). The overlap of these events are summarized in Table I.1.

Apart from the common hit fraction, a way to compare the Tesla and offline candidates on event-by-event basis is to look at the same variables for matched candidates. For example, mass and p_T distributions are presented in Fig. I.2. Since physical results of this analysis are based on the fit of t_z , comparison of Tesla and offline distributions of this variable (and variables, which are used in the calculation of t_z) was performed, see at Fig. I.3. Event though there are discrepancies in t_z values for small number of candidate, statistically these distributions are identical, which was proven by Kolmogorov-Smirnov test. During this test we compared distributions of t_z variable for Tesla and for offline samples. Test was performed by standard ROOT libraries and gave Kolmogorov-Smirnov value equal to 1.0.

The final check of difference between Tesla and offline reconstitution procedures is to

Table I.1: Summary on Tesla/Offline MC event numebrs. The difference between these numbers is less than 0.1%, which can be neglected.

	Tesla	Stripping
Total generated	959006	
Total reconstructed	432111	431433
& Trigger cuts	347392	346962
& Offline cuts	310479	310270
&Overlap>70%	310478	310270
& MC-matched	306810	306677

Table I.2: Fit results comparing offline and Tesla candidates.

	Offline	Tesla
$\mu_{J/\psi}$	3097.5 ± 0.058325	3097.5 ± 0.058317
σ_1	11.550 ± 0.04775	11.551 ± 0.047761
β	0.044156 ± 0.0028703	0.044688 ± 0.0029121
F_b	0.098185 ± 0.0016055	0.098140 ± 0.0016048
$\mu * 1000$	-0.618633 ± 0.26937	-0.608140 ± 0.26938
S_1	4.4019 ± 0.21253	4.3688 ± 0.21149
S_2	1.0501 ± 0.0053997	1.0497 ± 0.0054302
τ_b	1.4818 ± 0.028024	1.4824 ± 0.028105
n_{bkg}	322.81 ± 44.286	321.15 ± 44.361
n_{sig}	48699 ± 224.36	48730 ± 224.44

949 compare results of the fit of the same simulated dataset reconstructed in both ways.
950 Results of the fit are listed in Table I.2 and shown in Fig. I.4 and Fig. I.5 for a high
951 statistic kinematic bin.

Overlap with matched candidate

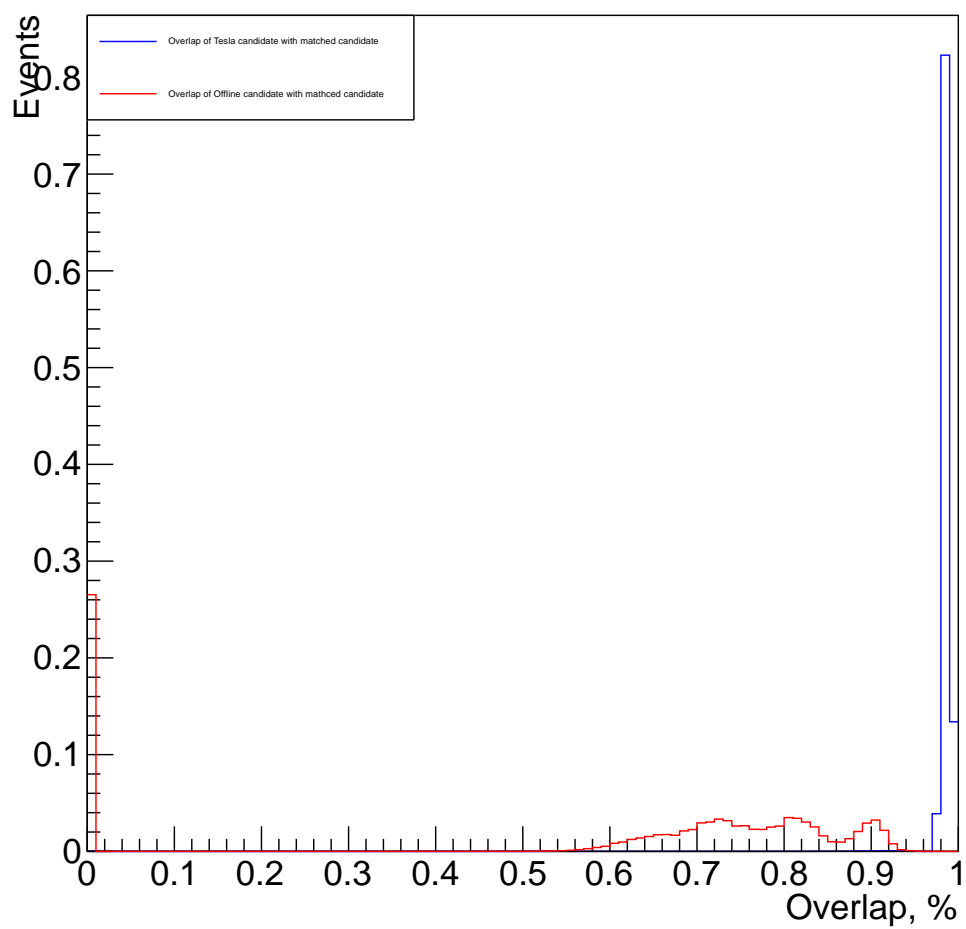


Figure I.1: LHCbID fraction overlap with matched candidate for Tesla and offline candidates.

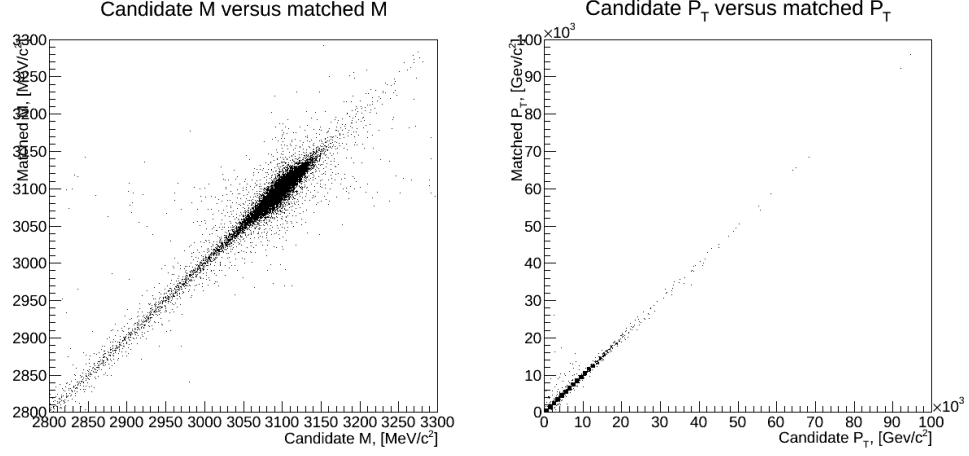


Figure I.2: Comparison of candidate mass (left) and p_T (right) of matched candidates.

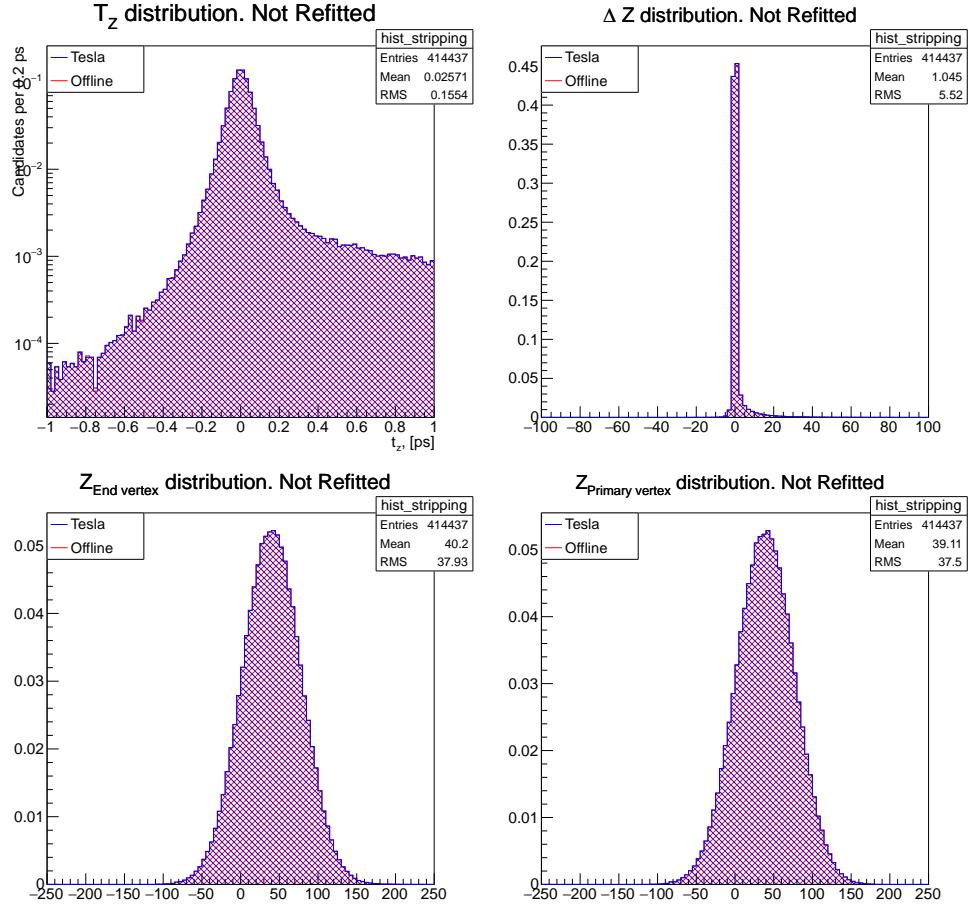


Figure I.3: Comparison of t_z , Δ_Z , primary and end vertices coordinates for Tesla and offline candidates.

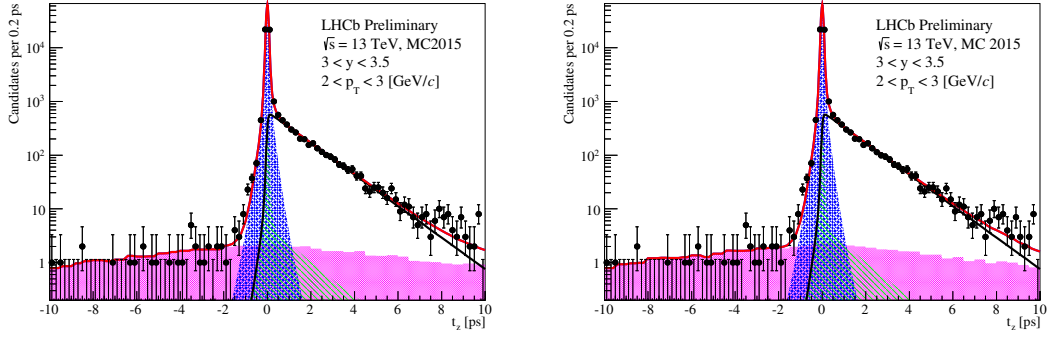


Figure I.4: t_z fit of offline (left) and Tesla (right) candidates.

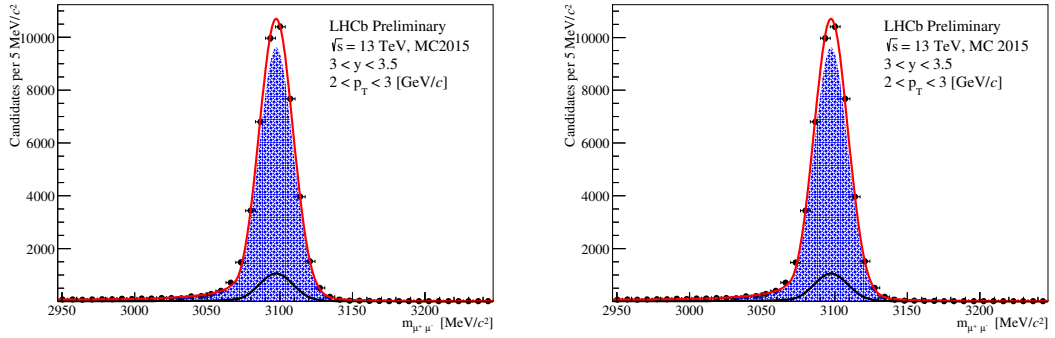


Figure I.5: Invariant mass fit of offline (left) and Tesla (right) candidates.

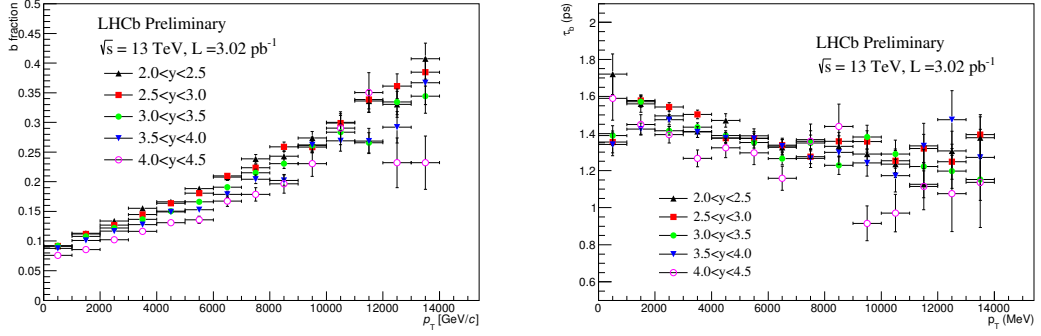


Figure J.1: Values for each (p_T, y) bin of the fitted b -fraction (Left) and pseudo b lifetime τ_b (Right). Only statistical uncertainties are shown.

J J/ψ fits

The number of inclusive J/ψ signal events and the fraction of J/ψ from b -hadron decays is determined by fitting the invariant mass $M(J/\psi)$ and t_z distribution with an unbinned simultaneous maximum likelihood fit, as described above in section 5. To gain confidence in the quality of this fit, the bin-to-bin variation of the fitted parameters is studied. The results for the fitted b -fraction and the pseudo b lifetime τ_b are shown in Fig. J.1. It can be seen that there are relatively smooth variation bin-to-bin. The behaviour for most parameters is similar to the previous studies. As is expected the b -fraction increases with increasing p_T . τ_b is falling as p_T increases, this was already observed in the previous analysis. The bin-to-bin variation of the fitted parameters for the bias on t_z (μ) is shown in Fig. J.2 together with the resolution scale factor $S = \sqrt{\beta S_1^2 + (1 - \beta) S_2^2}$. The bias of t_z is small negative, which was also seen in the previous analysis. The resolution scale is almost constant in the different bins.

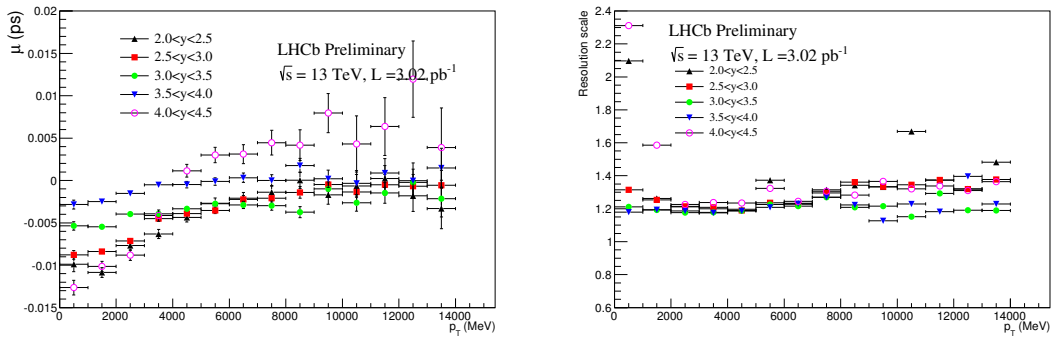


Figure J.2: Values for each (p_T, y) bin of the fitted bias on t_z (μ). Only statistical uncertainties are shown.

The bin-to-bin variation of the fitted mass parameters for the mean of the invariant

966 J/ψ mass and the signal yield are shown in Fig. J.3. The mean is constant in different
 967 bins, whereas the signal yield is highest at small p_T and mid-rapidity bins. The width of

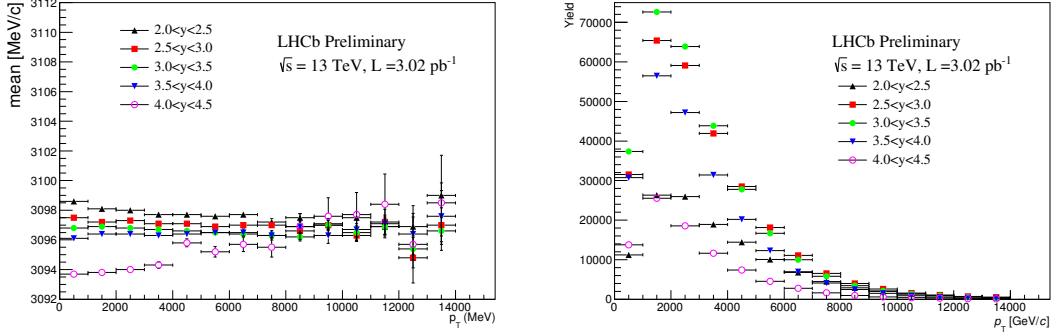


Figure J.3: Values for each (p_T, y) bin of the fitted invariant mass mean (Left) and the signal yield (Right). Only statistical uncertainties are shown.

967 the narrower CB σ_1 for the different bins is shown in Fig. J.4. The variation of the σ_1 is
 968 expected since the momentum resolution of the spectrometer is degraded at high rapidity
 969 (see Ref. [67]).

970 The fitting values for the b-fraction are further checked with the input values for the MC

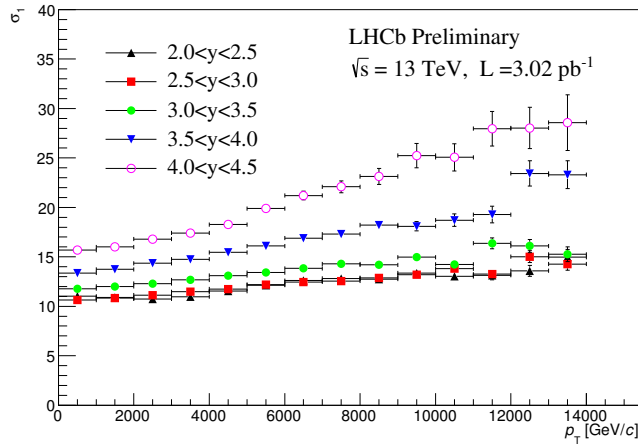


Figure J.4: Values for each (p_T, y) bin of the fitted width σ_1 of the narrower CB function. Only statistical uncertainties are shown.

971 samples and are shown in Fig. J.5. Here one can see that those values are comparable
 972 within their errors.

973 The effect of the tail due to unreconstructed primary vertices has been studied in section 5.
 974 The method consists of associating a J/ψ from a given event with the primary vertex of the
 975 next event in the J/ψ sample. The second approach is to use the expected analytic form
 976

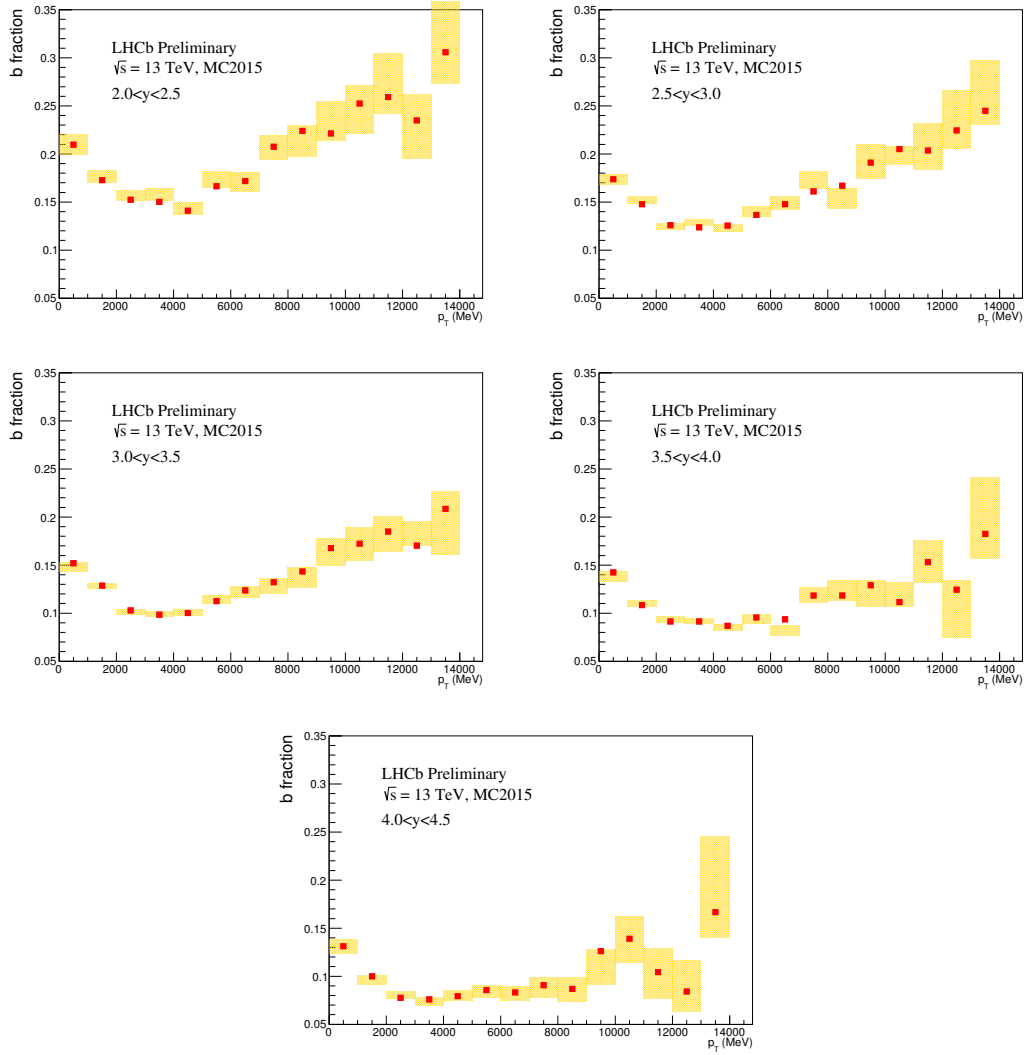


Figure J.5: Values of the fitted b -fraction (yellow filled area) compared with input MC b -fraction (points) as a function of p_T for the five rapidity bins used in the analysis. Only statistical uncertainties are shown.

of the tail function which is a bifurcated exponential with equal slopes on the positive and negative sides, which has been used for a global fit in section 7.1.2 to check for systematic uncertainty due to this tail parametrization. The results for the b -fraction in the two cases for each (p_T, y) are summarized in Fig. J.6 for MC simulation.

As a further check the fit range was changed from ± 10 ps to ± 20 ps. The results for the b -fraction in the two cases are shown in Fig. J.7 for MC. Both of the fitting results are in good agreement.

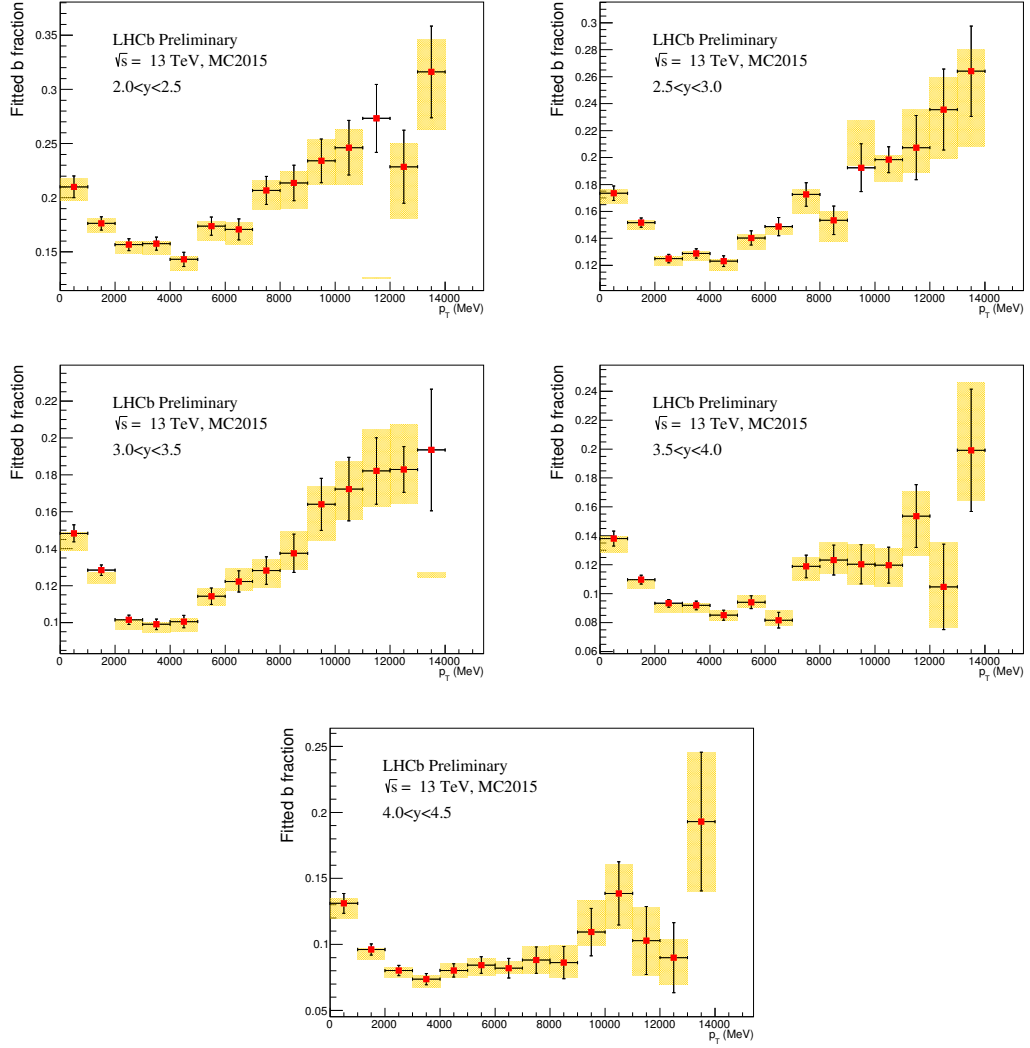


Figure J.6: Value of the fitted b -fraction using the next-event method (points) to model the tail fraction and with the analytic form (yellow). Only statistical uncertainties are shown.

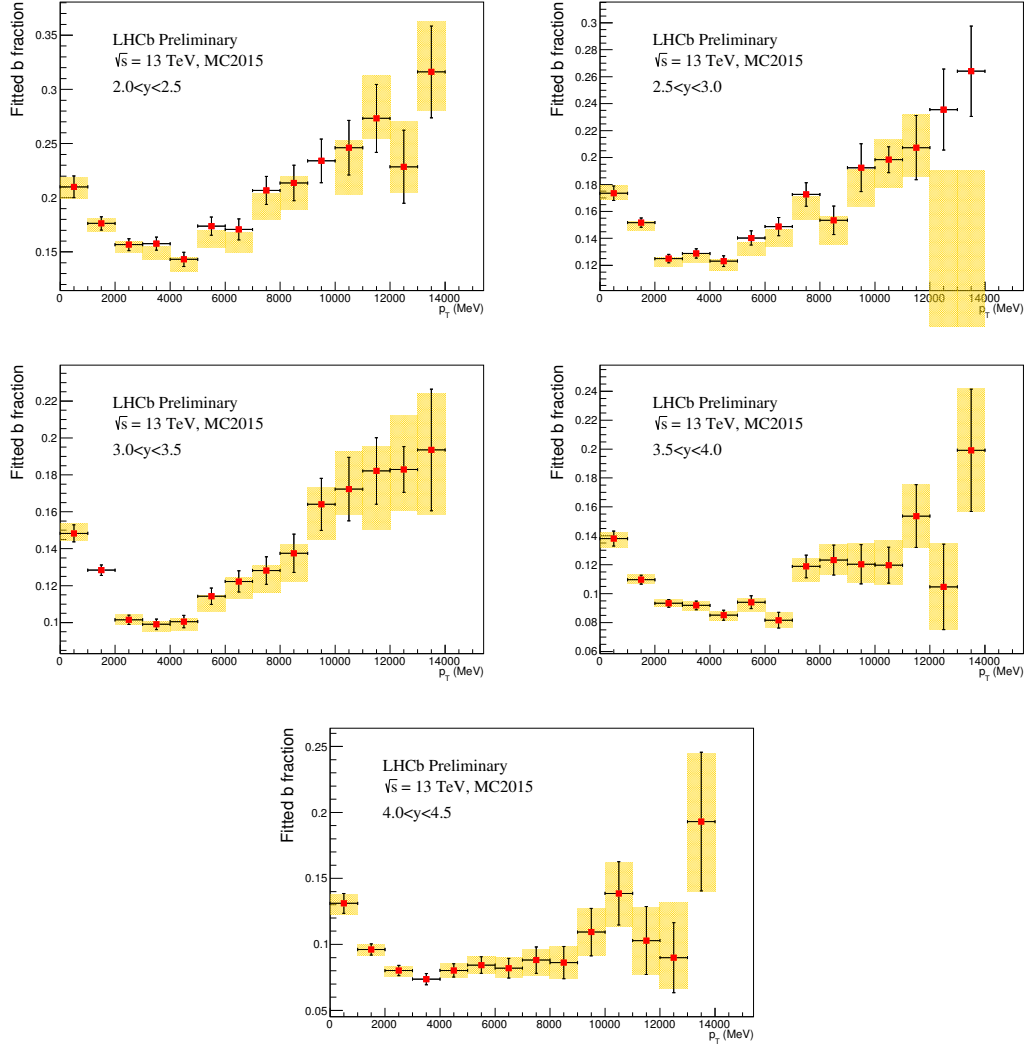


Figure J.7: Value of the fitted b -fraction using a ± 10 ps fit window (points) with a ± 20 ps window (yellow). Only statistical uncertainties are shown.

984 K Study of extrapolation factor

985 If the LHCb and CMS acceptance is totally complementary, the two J/ψ from b cross
 986 section measurements allows for an model independent way of determining extrapolation
 987 factor $\alpha_{4\pi}$. Although this is not the case, it is still possible to cross check the goodness
 988 of the extrapolation factor with a dedicated generator. The LHCb measured the J/ψ
 989 from b cross section to be $1.14 \pm 0.01(\text{stat}) \pm 0.16(\text{syst}) \mu\text{b}$ [33] or $1.07 \pm 0.064 \mu\text{b}$ [39]
 990 with updated luminosity and systematic uncertainties (updated in the corresponding
 991 internal analysis note), within $2 < y < 4.5$ and $p_T < 14 \text{ GeV}/c$. At CMS, the cross
 992 section of J/ψ from b times the $J/\psi \rightarrow \mu^+\mu^-$ branching fraction is determined to be
 993 $26.0 \pm 1.4(\text{stat}) \pm 1.6(\text{syst}) \pm 2.9(\text{lumi}) \text{ nb}$, within $-2.4 < y < 2.4$ and $6.5 < p_T < 30 \text{ GeV}/c$.
 994 With $\mathcal{B}(J/\psi \rightarrow \mu^+\mu^-) = (5.961 \pm 0.033)\%$, the CMS J/ψ from b cross section is calculated
 995 to be $0.436 \pm 0.023(\text{stat}) \pm 0.027(\text{syst}) \pm 0.049(\text{lumi}) \mu\text{b} = 0.436 \pm 0.060 \mu\text{b}$.

996 The FONLL calculation of $pp \rightarrow b\bar{b}X, b, \bar{b} \rightarrow J/\psi X$ cross section at 7 TeV gives $1.16 \mu\text{b}$
 997 at LHCb and $0.398 \mu\text{b}$ at CMS, in the kinematic ranges given above, respectively. The cross
 998 sections predicated by FONLL are consistent with both LHCb and CMS measurements
 999 (the uncertainties of FONLL are not presented here), and the ratio of CMS result over
 1000 LHCb for J/ψ from b cross section is consistent the one given by FONLL, which implies
 1001 that the extrapolation factors for LHCb and CMS given by FONLL are consistent with
 1002 data. If FONLL gives more fraction of J/ψ from b in LHCb acceptance compared to data,
 1003 then there will be less in CMS acceptance (partially complementary kinematics), and
 1004 the ratio in CMS over LHCb would be different from data. This favor the idea that the
 1005 extrapolation factor given by FONLL is reasonable. We don't perform extensive check of
 1006 the consistency of $\alpha_{4\pi}$ factor with more generators, for example in Pythia 6 and Pythia 8,
 1007 but since they give values similar to FONLL at various centre-of-mass energies, they are
 1008 also believed to be good. It should be noted that, the extrapolation factor is not a direct
 1009 measurement of this analysis, and the $pp \rightarrow b\bar{b}X$ given in this analysis is easy to extend to
 1010 other value of $\alpha_{4\pi}$ with another generator.

References

- [1] C. E. Carlson and R. Suaya, *Hadronic Production of J/ψ Mesons*, Phys. Rev. **D14** (1976) 3115.
- [2] A. Donnachie and P. V. Landshoff, *Production of Lepton Pairs, J/ψ and Charm with Hadron Beams*, Nucl. Phys. **B112** (1976) 233.
- [3] S. D. Ellis, M. B. Einhorn, and C. Quigg, *Comment on Hadronic Production of Psions*, Phys. Rev. Lett. **36** (1976) 1263.
- [4] H. Fritzsch, *Producing Heavy Quark Flavors in Hadronic Collisions: A Test of Quantum Chromodynamics*, Phys. Lett. **B67** (1977) 217.
- [5] M. Gluck, J. F. Owens, and E. Reya, *Gluon Contribution to Hadronic J/ψ Production*, Phys. Rev. **D17** (1978) 2324.
- [6] C.-H. Chang, *Hadronic Production of J/ψ Associated With a Gluon*, Nucl. Phys. **B172** (1980) 425.
- [7] R. Baier and R. Ruckl, *Hadronic Production of J/ψ and Upsilon: Transverse Momentum Distributions*, Phys. Lett. **B102** (1981) 364.
- [8] G. T. Bodwin, E. Braaten, and G. P. Lepage, *Rigorous QCD analysis of inclusive annihilation and production of heavy quarkonium*, Phys. Rev. **D51** (1995) 1125, [arXiv:hep-ph/9407339](#).
- [9] P. L. Cho and A. K. Leibovich, *Color octet quarkonia production*, Phys. Rev. **D53** (1996) 150, [arXiv:hep-ph/9505329](#).
- [10] P. L. Cho and A. K. Leibovich, *Color octet quarkonia production. 2.*, Phys. Rev. **D53** (1996) 6203, [arXiv:hep-ph/9511315](#).
- [11] CDF, F. Abe *et al.*, *J/ψ and $\psi(2S)$ production in $p\bar{p}$ collisions at $\sqrt{s} = 1.8$ TeV*, Phys. Rev. Lett. **79** (1997) 572.
- [12] J. M. Campbell, F. Maltoni, and F. Tramontano, *QCD corrections to J/ψ and Upsilon production at hadron colliders*, Phys. Rev. Lett. **98** (2007) 252002, [arXiv:hep-ph/0703113](#).
- [13] J. P. Lansberg, *J/ψ production at $\sqrt{s}=1.96$ and 7 TeV: Color-Singlet Model, NNLO* and polarisation*, J. Phys. **G38** (2011) 124110, [arXiv:1107.0292](#).
- [14] B. Gong and J.-X. Wang, *Next-to-leading-order QCD corrections to J/ψ polarization at Tevatron and Large-Hadron-Collider energies*, Phys. Rev. Lett. **100** (2008) 232001, [arXiv:0802.3727](#).

- [15] M. Cacciari, M. Greco, M. L. Mangano, and A. Petrelli, *Charmonium production at the Tevatron*, Phys. Lett. **B356** (1995) 553, [arXiv:hep-ph/9505379](#).
- [16] E. Braaten and S. Fleming, *Color octet fragmentation and the psi-prime surplus at the Tevatron*, Phys. Rev. Lett. **74** (1995) 3327, [arXiv:hep-ph/9411365](#).
- [17] Y.-Q. Ma, K. Wang, and K.-T. Chao, *A complete NLO calculation of the J/ψ and ψ' production at hadron colliders*, Phys. Rev. **D84** (2011) 114001, [arXiv:1012.1030](#).
- [18] B. Gong, X. Q. Li, and J.-X. Wang, *QCD corrections to J/ψ production via color octet states at Tevatron and LHC*, Phys. Lett. **B673** (2009) 197, [arXiv:0805.4751](#).
- [19] M. Butenschoen and B. A. Kniehl, *Reconciling J/ψ production at HERA, RHIC, Tevatron, and LHC with NRQCD factorization at next-to-leading order*, Phys. Rev. Lett. **106** (2011) 022003, [arXiv:1009.5662](#).
- [20] M. Beneke and I. Z. Rothstein, *ψ' polarization as a test of color octet quarkonium production*, Phys. Lett. **B372** (1996) 157, [arXiv:hep-ph/9509375](#).
- [21] K.-T. Chao *et al.*, *J/ψ Polarization at Hadron Colliders in Nonrelativistic QCD*, Phys. Rev. Lett. **108** (2012) 242004, [arXiv:1201.2675](#).
- [22] B. Gong, L.-P. Wan, J.-X. Wang, and H.-F. Zhang, *Polarization for Prompt J/ψ and $\psi(2S)$ Production at the Tevatron and LHC*, Phys. Rev. Lett. **110** (2013), no. 4 042002, [arXiv:1205.6682](#).
- [23] M. Butenschoen and B. A. Kniehl, *J/ψ polarization at Tevatron and LHC: Nonrelativistic-QCD factorization at the crossroads*, Phys. Rev. Lett. **108** (2012) 172002, [arXiv:1201.1872](#).
- [24] CDF, A. Abulencia *et al.*, *Polarization of J/ψ and ψ_{2S} mesons produced in $p\bar{p}$ collisions at $\sqrt{s} = 1.96$ -TeV*, Phys. Rev. Lett. **99** (2007) 132001, [arXiv:0704.0638](#).
- [25] D0, V. M. Abazov *et al.*, *Measurement of the polarization of the ψ_{1S} and ψ_{2S} states in $p\bar{p}$ collisions at $\sqrt{s} = 1.96$ -TeV*, Phys. Rev. Lett. **101** (2008) 182004, [arXiv:0804.2799](#).
- [26] ALICE, B. Abelev *et al.*, *J/ψ polarization in pp collisions at $\sqrt{s} = 7$ TeV*, Phys. Rev. Lett. **108** (2012) 082001, [arXiv:1111.1630](#).
- [27] CMS, S. Chatrchyan *et al.*, *Measurement of the prompt J/ψ and $\psi(2S)$ polarizations in pp collisions at $\sqrt{s} = 7$ TeV*, Phys. Lett. **B727** (2013) 381, [arXiv:1307.6070](#).
- [28] CMS, S. Chatrchyan *et al.*, *Measurement of the $Y(1S)$, $Y(2S)$ and $Y(3S)$ polarizations in pp collisions at $\sqrt{s} = 7$ TeV*, Phys. Rev. Lett. **110** (2013), no. 8 081802, [arXiv:1209.2922](#).
- [29] LHCb, R. Aaij *et al.*, *Measurement of J/ψ polarization in pp collisions at $\sqrt{s} = 7$ TeV*, Eur. Phys. J. **C73** (2013), no. 11 2631, [arXiv:1307.6379](#).

- [30] LHCb, R. Aaij *et al.*, *Measurement of $\psi(2S)$ polarisation in pp collisions at $\sqrt{s} = 7$ TeV*, Eur. Phys. J. **C74** (2014), no. 5 2872, [arXiv:1403.1339](#).
- [31] ALICE, B. Abelev *et al.*, *Inclusive J/ψ production in pp collisions at $\sqrt{s} = 2.76$ TeV*, Phys. Lett. **B718** (2012) 295, [arXiv:1203.3641](#).
- [32] LHCb collaboration, R. Aaij *et al.*, *Measurement of J/ψ production in pp collisions at $\sqrt{s} = 2.76$ TeV*, JHEP **02** (2013) 041, [arXiv:1212.1045](#).
- [33] LHCb collaboration, R. Aaij *et al.*, *Measurement of J/ψ production in pp collisions at $\sqrt{s} = 7$ TeV*, Eur. Phys. J. **C71** (2011) 1645, [arXiv:1103.0423](#).
- [34] CMS, V. Khachatryan *et al.*, *Prompt and non-prompt J/ψ production in pp collisions at $\sqrt{s} = 7$ TeV*, Eur. Phys. J. **C71** (2011) 1575, [arXiv:1011.4193](#).
- [35] ATLAS, G. Aad *et al.*, *Measurement of the differential cross-sections of inclusive, prompt and non-prompt J/ψ production in proton-proton collisions at $\sqrt{s} = 7$ TeV*, Nucl. Phys. **B850** (2011) 387, [arXiv:1104.3038](#).
- [36] ALICE, K. Aamodt *et al.*, *Rapidity and transverse momentum dependence of inclusive J/ψ production in pp collisions at $\sqrt{s} = 7$ TeV*, Phys. Lett. **B704** (2011) 442, [arXiv:1105.0380](#).
- [37] CMS, S. Chatrchyan *et al.*, *J/ψ and ψ_{2S} production in pp collisions at $\sqrt{s} = 7$ TeV*, JHEP **1202** (2012) 011, [arXiv:1111.1557](#).
- [38] LHCb collaboration, R. Aaij *et al.*, *Production of J/ψ and Υ mesons in pp collisions at $\sqrt{s} = 8$ TeV*, JHEP **06** (2013) 064, [arXiv:1304.6977](#).
- [39] LHCb collaboration, R. Aaij *et al.*, *Measurement of J/ψ polarization in pp collisions at $\sqrt{s} = 7$ TeV*, Eur. Phys. J. **C73** (2013) 2631, [arXiv:1307.6379](#).
- [40] M. Cacciari, M. Greco, and P. Nason, *The $P(T)$ spectrum in heavy flavor hadroproduction*, JHEP **9805** (1998) 007, [arXiv:hep-ph/9803400](#).
- [41] LHCb collaboration, A. A. Alves Jr. *et al.*, *The LHCb detector at the LHC*, JINST **3** (2008) S08005.
- [42] LHCb collaboration, R. Aaij *et al.*, *LHCb detector performance*, [arXiv:1412.6352](#).
- [43] R. Aaij *et al.*, *Performance of the LHCb Vertex Locator*, JINST **9** (2014) P09007, [arXiv:1405.7808](#).
- [44] R. Arink *et al.*, *Performance of the LHCb Outer Tracker*, JINST **9** (2014) P01002, [arXiv:1311.3893](#).
- [45] M. Adinolfi *et al.*, *Performance of the LHCb RICH detector at the LHC*, Eur. Phys. J. **C73** (2013) 2431, [arXiv:1211.6759](#).

- [46] A. A. Alves Jr. *et al.*, *Performance of the LHCb muon system*, JINST **8** (2013) P02022, [arXiv:1211.1346](#).
- [47] T. Sjöstrand, S. Mrenna, and P. Skands, *PYTHIA 6.4 physics and manual*, JHEP **05** (2006) 026, [arXiv:hep-ph/0603175](#).
- [48] I. Belyaev *et al.*, *Handling of the generation of primary events in Gauss, the LHCb simulation framework*, J. Phys. Conf. Ser. **331** (2011) 032047.
- [49] D. J. Lange, *The EvtGen particle decay simulation package*, Nucl. Instrum. Meth. **A462** (2001) 152.
- [50] P. Golonka and Z. Was, *PHOTOS Monte Carlo: A precision tool for QED corrections in Z and W decays*, Eur. Phys. J. **C45** (2006) 97, [arXiv:hep-ph/0506026](#).
- [51] Geant4 collaboration, J. Allison *et al.*, *Geant4 developments and applications*, IEEE Trans. Nucl. Sci. **53** (2006) 270; Geant4 collaboration, S. Agostinelli *et al.*, *Geant4: a simulation toolkit*, Nucl. Instrum. Meth. **A506** (2003) 250.
- [52] M. Clemencic *et al.*, *The LHCb simulation application, Gauss: Design, evolution and experience*, J. Phys. Conf. Ser. **331** (2011) 032023.
- [53] M. Bargiotti and V. Vagnoni, *Heavy quarkonia sector in PYTHIA 6.324: Tuning, validation and perspectives at LHC(b)*, CERN-LHCB-2007-042.
- [54] S. Kullback and R. A. Leibler, *On information and sufficiency*, Ann. Math. Statist. **22** (1951) 79; S. Kullback, *Letter to editor: the Kullback-Leibler distance*, The American Statistician **41** (1987) 340; the use of the Kullback-Leibler distance is described in M. Needham, *Clone track identification using the Kullback-Leibler distance*, LHCb-2008-002.
- [55] Particle Data Group, K. A. Olive *et al.*, *Review of particle physics*, Chin. Phys. **C38** (2014) 090001.
- [56] F. Archilli *et al.*, *Performance of the muon identification at LHCb*, JINST **8** (2013) P10020, [arXiv:1306.0249](#).
- [57] T. Skwarnicki, *A study of the radiative cascade transitions between the Upsilon-prime and Upsilon resonances*, PhD thesis, Institute of Nuclear Physics, Krakow, 1986, DESY-F31-86-02.
- [58] J. Lefrancous, *Crystal ball fits*, [link](#).
- [59] D. Martinez Santos and F. Dupertuis, *Mass distributions marginalized over per-event errors*, Nucl. Instrum. Meth. **A764** (2014) 150, [arXiv:1312.5000](#).
- [60] LHCb collaboration, R. Aaij *et al.*, *Measurement of the track reconstruction efficiency at LHCb*, [arXiv:1408.1251](#), to appear in JINST.

- 1144 [61] T. Sjöstrand, S. Mrenna, and P. Skands, *A brief introduction to PYTHIA 8.1*, Comput.
1145 Phys. Commun. **178** (2008) 852, [arXiv:0710.3820](#).
- 1146 [62] M. Cacciari *et al.*, *Theoretical predictions for charm and bottom production at the*
1147 *LHC*, JHEP **1210** (2012) 137, [arXiv:1205.6344](#).
- 1148 [63] H.-S. Shao *et al.*, *Yields and polarizations of prompt J/ψ and $\psi(2S)$ production in*
1149 *hadronic collisions*, JHEP **1505** (2015) 103, [arXiv:1411.3300](#).
- 1150 [64] M. Cacciari, M. L. Mangano, and P. Nason, *Gluon PDF constraints from the ratio of*
1151 *forward heavy quark production at the LHC at $\sqrt{S}=7$ and 13 TeV*, [arXiv:1507.0619](#).
- 1152 [65] LHCb collaboration, R. Aaij *et al.*, *Absolute luminosity measurements with the LHCb*
1153 *detector at the LHC*, JINST **7** (2012) P01010, [arXiv:1110.2866](#).
- 1154 [66] LHCb collaboration, R. Aaij *et al.*, *Precision luminosity measurements at LHCb*,
1155 JINST **9** (2014) P12005, [arXiv:1410.0149](#).
- 1156 [67] M. Needham, *Performance of the LHCb Track Reconstruction Software*, Tech. Rep.
1157 LHCb-2007-144. CERN-LHCb-2007-144, CERN, Geneva, Jan, 2008.